

**MICROSCALE HEMISPHERICAL SHELL RESONATING
GYROSCOPES**

A Dissertation
Presented to
The Academic Faculty

By

Peng Shao

In Partial Fulfillment
Of the Requirements for the Degree
Doctoral of Philosophy in Mechanical Engineering

Georgia Institute of Technology

DECEMBER 2014

Copyright © Peng Shao 2014

MICROSCALE HEMISPHERICAL SHELL RESONATING GYROSCOPES

Approved by:

Dr. Farrokh Ayazi, Advisor
School of Electrical and Computer
Engineering
Georgia Institute of Technology

Dr. F. Levent Degertekin
School of Mechanical Engineering
Georgia Institute of Technology

Dr. Olivier Pierron,
School of Mechanical Engineering
Georgia Institute of Technology

Dr. Oliver Brand
School of Electrical and Computer
Engineering
Georgia Institute of Technology

Dr. Peter J. Hesketh
School of Mechanical Engineering
Georgia Institute of Technology

Date Approved: Aug 20th, 2014

To my wife Mingming
and my daughter Mia

ACKNOWLEDGEMENTS

This long and winding journey would never end, if it were not for many people who have offered me generous support along the way. I am deeply indebted to all of them.

My deepest thanks go to my advisor, Prof. Farrokh Ayazi, who offered me timely assistantship and guidance. I would like to express my genuine gratitude for his outstanding mentorship, support, and encouragement throughout my years as a graduate student in IMEMS Lab. Under his supervision, I have grown both professionally and personally. I have certainly enjoyed our long discussions over the years, and these discussions have helped me understand how to approach and carry out my research.

I am very grateful to the members of my thesis committee, Prof. Olivier Pierron, Prof. Peter Hesketh, Prof. Levent Degertekin, and Prof. Oliver Brand, for their valuable feedback.

I would like to thank Dr. Logan Sorenson, Dr. Vahid Tavassoli and Benoit Hamelin for helpful discussion regarding the whole project, and their assistance on multiphysics modeling. I would also like to thank Curtis Mayberry and Chang-Shun Liu for interface circuit design and testing.

I cannot thank enough all the current and previous IMEMS Lab members for their assistance, suggestions, and friendship. Especially, I want to thank Jenna Fu, Xin Gao, Roozbeh Tabrizian, Arashk Norouz Pour Shirazi, Mojtaba Hodjat-Shamami, with whom I have had great time in discussion, cooperation, and also entertainment.

Most of all, I want to give my special thanks to my parents, my wife Mingming and my daughter Mia. Without them, I would not be able to finish my Ph.D degree.

I would like to acknowledge DARPA and Northrop Grumman Corporation for supporting this work.

TABLE OF CONTENTS

ACKNOWLEDGEMENTS	iv
LIST OF TABLES	ix
LIST OF FIGURES	x
LIST OF SYMBOLS AND ABBREVIATIONS	xvii
SUMMARY	xix
CHAPTER 1 INTRODUCTION	1
1.1 Introduction to Gyroscopes	1
1.1.1 Mechanical Gyroscopes	1
1.1.2 Optical Gyroscopes	3
1.1.3 Coriolis Vibratory Gyroscope	5
1.2 Working Principle of CVG	7
1.2.1 Coriolis Effect	7
1.2.2 Mode of Operation	9
1.2.3 Mode Matching	12
1.3 MEMS Gyroscopes	13
1.3.1 Non-degenerate Mode Gyroscope	13
1.3.2 Degenerate Mode Gyroscope	17
1.4 Why Hemisphere	19
1.5 Thesis Outline	20
CHAPTER 2 DESIGN AND SIMULATION OF MICROSCALE HEMISPHERICAL SHELL RESONATORS (μ HSR)	22
2.1 Theory of a Vibrating Hemispherical Shell	22
2.1.1 Strain of a Vibrating Shell	23
2.1.2 Strain Energy and Kinetic Energy	24
2.1.3 Mode Shape	24

2.1.4 Resonance Frequency	26
2.1.5 FEA Simulation	26
2.2 Energy Dissipation	29
2.2.1 Thermoelastic Damping (TED)	30
2.2.2 Squeezed Film Damping	33
2.2.3 Support Loss	37
2.2.4 Surface Loss	39
2.3 Structural Anisotropy	40
2.3.1 Isotropic Molding	41
2.3.2 Structural Thickness Anisotropy	47
2.3.3 Support Structure Anisotropy	52
CHAPTER 3 FABRICATION OF SILICON DIOXIDE μ HSR	57
3.1 Introduction	57
3.2 Fabrication Process	58
3.2.1 Hemispherical Molding Technique	59
3.2.2 Silicon Dioxide Hemispherical Shell Fabrication	61
3.2.3 Conformal ALD Coating	64
3.2.4 Assembly Process	65
3.3 Process Characterization	66
3.3.1 Surface Roughness of Silicon Mold	66
3.3.2 Thickness Variation	69
3.3.3 Re-entrant Extension	70
3.3.4 Capacitive Gap	71
3.3.5 Support Structure	71
CHAPTER 4 TEST AND CHARACTERIZATION OF SILICON DIOXIDE μ HSR	73
4.1 Resonance Modes	73
4.2 Ring Down Test	77

4.3 Environmental Behavior	80
4.4 Frequency Mismatch	82
4.5 Optical Measurement	84
4.6 Static Stiffness Measurement	86
CHAPTER 5 ELECTROMECHANICAL DESIGN AND SIMULATION OF MICROSCALE HEMISPHERICAL SHELL RESONATING GYROSCOPES (μ HRG)	
	88
5.1 Pull-in Voltage	89
5.2 Electrostatic Tuning	93
5.3 Drive Amplitude	94
5.4 Sensitivity	97
CHAPTER 6 MONOLITHIC FABRICATION OF POLYSILICON μ HRG	
	99
6.1 Fabrication Features	99
6.6.1 Structural Material	99
6.6.2 3D HARPSS	100
6.6.3 Self-aligned Structures	100
6.6.4 Scalable Capacitive Gap	101
6.6.5 DC Bias	102
6.2 Microfabrication Process Flow	102
6.3 Fabrication Results	108
6.4. Front Side DC Bias Contact	111
6.5 Detailed Process Modules	114
6.5.1 Silicon Dioxide Etching	114
6.5.2 Silicon DRIE	115
6.5.3 Silicon Isotropic Etching	116
6.5.4 Polysilicon Deposition	117
CHAPTER 7 TEST AND CHARACTERIZATION OF POLYSILICON μ HRG	
	119

7.1 Front-end Electronics	119
7.2 Frequency Response	121
7.3 Mode Matching Procedure	123
7.3 Rate Sensitivity	125
7.4 Discussion	127
CHAPTER 8 SUMMARY AND FUTURE WORK	133
8.1 Contributions	133
8.2 Future Work	135
8.2.1 Quality Factor Improvement	135
8.2.2 Rate Integrating Mode Operation	137
REFERENCES	139

LIST OF TABLES

Table 2.1: COMSOL eigenfrequency study of a polysilicon hemispherical shell	28
Table 2.2: Material properties.....	33
Table 2.3: Selected TED simulation run in COMSOL.....	33
Table 4.1: Geometric parameters of measured μ HSR	74
Table 4.2: Comparison of resonance frequency by equation (4.1), COMSOL FEA and measured results.....	75
Table 4.3 Summary of optical test results.....	86
Table 5.1 Reported value to angular gain for various structures	97
Table 6.1: Parameters of oxide etch recipe in Plasma-therm ICP	115
Table 6.2: Parameters of oxide etch recipe in Vision RIE.....	115
Table 6.3: Parameters of silicon DRIE in STS-Pegasus.....	116
Table 6.4: Parameters of silicon isotropic etching in STS-ICP	117
Table 6.5: Parameters of silicon isotropic etching in STS-HRM	117
Table 6.6: Parameters of LPCVD undoped polysilicon in Tystar Furnace	118
Table 6.7: Parameters of LPCVD in-situ boron doped polysilicon in Tystar Furnace...	118
Table 7.1: Support loss estimation results for various designs	130

LIST OF FIGURES

Figure 1.1: A mechanical gyroscope Structure (Source: Wikipedia)	2
Figure 1.2: Illustration of gyroscope precession [4]	2
Figure 1.3: Illustration of Sagnac effect [7].....	3
Figure 1.4: Open loop design of fiber optic gyroscope [6].....	3
Figure 1.5: A ring laser gyroscope [8].....	4
Figure 1.6: Tuning fork gyroscope	5
Figure 1.7: Hemispherical Resonator Gyroscope (HRG) Assembly	6
Figure 1.8: Fused quartz hemispherical shell resonator (HSR)	7
Figure 1.9: Inertial frame and rotating frame [15].....	8
Figure 1.10: Illustration of a single proof-mass CVG [15].....	8
Figure 1.11: Dynamics of a rate mode CVG	9
Figure 1.12: Dynamics of a rate integrating gyroscope (RIG)	10
Figure 1.13: Dynamics of a rate integrating gyroscope with finite quality factor	11
Figure 1.14: Dynamics of a rate integrating gyroscope with finite frequency mismatch. 11	
Figure 1.15: Split mode operation and matched mode operation	12
Figure 1.16: SEM of Draper’s silicon on glass tuning fork gyroscope [19].....	14
Figure 1.17: SEM of Georgia Tech mode matched tuning fork gyroscope [18]	15
Figure 1.18: UC Irvine’s decoupled gyroscope [23]	16
Figure 1.19: The Middle East Technical University’s decoupled gyroscope [27]	17
Figure 1.20: HARPSS polysilicon ring gyroscope by University of Michigan [28]	18
Figure 1.21: SOG silicon cylindrical gyroscope by University of Michigan [32].....	18
Figure 1.22: Bulk acoustic wave (BAW) silicon disk gyroscope by Georgia Institute of Technology [37].....	19
Figure 2.1: Geometric illustration of a hemispherical shell [39]	22
Figure 2.2: Axial symmetric meshing in COMSOL Multiphysics	27

Figure 2.3: Rocking mode at 14.33 kHz for a polysilicon hemispherical shell.....	27
Figure 2.4: m=2 mode at 4.85 kHz for a polysilicon hemispherical shell	27
Figure 2.5: m=3 mode at 13.35 kHz for a polysilicon hemispherical shell	28
Figure 2.6: m=4 mode at 25.64 kHz for a polysilicon hemispherical shell	28
Figure 2.7: Temperature distribution of a μ HSR at its m=2 mode	32
Figure 2.8: Illustration of COMSOL squeeze film damping simulation	35
Figure 2.9: $Q_{\text{squeeze_film}}$ as a function of vacuum pressure for a 2 μ m gap device	35
Figure 2.10: $Q_{\text{squeeze_film}}$ as a function of capacitive gap size	36
Figure 2.11: Illustration of PML region and resonating structure in support loss simulation.....	38
Figure 2.12: Q_{support} Vs. support radius.....	38
Figure 2.13: Q_{support} Vs. support stem length	39
Figure 2.14: Unit cell of single crystal silicon.....	42
Figure 2.15: Silicon structure viewed from (1,0,0) direction	42
Figure 2.16: Silicon structure viewed from (1,1,1) direction	42
Figure 2.17: Hemispherical shell with four-fold symmetry.....	43
Figure 2.18: Hemispherical shell with six-fold symmetry.....	44
Figure 2.19: Simulated frequency mismatch for m=2 mode of 100 wafer.....	44
Figure 2.20: Simulated frequency mismatch for m=3 mode of 100 wafer.....	45
Figure 2.21: Simulated frequency mismatch for m=2 mode of 111 wafer.....	46
Figure 2.22: Simulated frequency mismatch for m=3 mode of 111 wafer.....	46
Figure 2.23: Schematic diagram depicting a few of the crystal plane normals exposed during thermal oxidation of silicon hemispherical mold	48
Figure 2.24: Interpolation of silicon dioxide growth rate vs. crystal plane index	48
Figure 2.25: Thickness map for 20 hours of wet thermal oxidation at 1100°C.....	49
Figure 2.26: Simulated frequency split on (001) and (111) type substrates	51
Figure 2.27: Mesh used to simulate a square support.....	52

Figure 2.28: Mesh used to simulate a triangle support	53
Figure 2.29: Simulated relative frequency mismatch between m=2 degenerate modes with square support Vs. support size	53
Figure 2.30: Simulated relative frequency mismatch between m=3 degenerate modes with square support Vs. support size	54
Figure 2.31: Relative frequency mismatch between m=2 degenerate modes with triangle support Vs. support size.....	54
Figure 2.32: Relative frequency mismatch between m=3 degenerate modes with triangle support Vs. support size.....	55
Figure 2.33: Relative frequency mismatch between m=2 degenerate modes Vs. support misalignment.....	55
Figure 2.34: Relative frequency mismatch between rocking modes Vs. support misalignment.....	56
Figure 3.1: SF ₆ plasma isotropic etch: mold diameter Vs. etching time.....	60
Figure 3.2: SF ₆ plasma isotropic etch: mold depth Vs. etching time.....	60
Figure 3.3: Results of isotropic silicon etching	61
Figure 3.4: Fabrication and assembly process of μ HSR.....	63
Figure 3.5: Wafer level fabrication of silicon dioxide hemispherical shells	64
Figure 3.6: SEM image of silicon dioxide hemispherical shells	64
Figure 3.7: Microscope image of assembled μ HSR	65
Figure 3.8: SEM image of the surface roughness of an untreated hemispherical mold ...	67
Figure 3.9: AFM measurement of the surface roughness of an untreated hemispherical mold	67
Figure 3.10: SEM image of the surface roughness of a hydrogen annealed hemispherical mold	68
Figure 3.11: AFM measurement of the surface roughness of a hydrogen annealed hemispherical mold.....	69

Figure 3.12: Thickness variation of silicon dioxide hemispherical shell caused by XeF ₂ releasing	70
Figure 3.13: Top view SEM: showing reentrant and capacitive gap	71
Figure 3.14: Microscopic image of the support structure	72
Figure 4.1: m=2 mode resonance peak of silicon dioxide μHSR (inset: mode shape).....	76
Figure 4.2: m=3 mode resonance peak of silicon dioxide μHSR (inset: mode shape).....	76
Figure 4.3: Electrostatic tuning curve of m=2 mode resonance of silicon dioxide μHSR, fitted with quadratic equation	77
Figure 4.4: Electrostatic tuning curve of m=3 mode resonance silicon dioxide μHSR, fitted with quadratic equation	77
Figure 4.5: Illustration of electronic setup for ringdown measurement.....	78
Figure 4.6: Prototype of ringdown measurement circuit	79
Figure 4.7: m=2 resonance peak of a batch #3 device	79
Figure 4.8: Ringdown measurement of a batch #3 device.....	80
Figure 4.9: Quality factor Vs. vacuum pressure	81
Figure 4.10: TCF and quality factor Vs. temperature	81
Figure 4.11: Frequency mismatch between m=2 degenerate modes for μHSR fabricated out of (100) wafer	82
Figure 4.12: Frequency mismatch between m=3 degenerate modes for μHSR fabricated out of (100) wafer	83
Figure 4.13: Frequency mismatch between m=2 degenerate modes for μHSR fabricated out of (111) wafer	83
Figure 4.14: Frequency mismatch between m=3 degenerate modes for μHSR fabricated out of (111) wafer	84
Figure 4.15: Schematics of optical test setup (Courtesy of Northrop Grumman)	85
Figure 4.16: Optical test setup (Courtesy of Northrop Grumman).....	85
Figure 4.17: Optical ringdown test results (Courtesy of Northrop Grumman).....	85

Figure 4.18: Frequency sweep test results (Courtesy of Northrop Grumman).....	86
Figure 4.19 Static stiffness measurement system (Courtesy of Femtotools).....	87
Figure 4.20: Static deformation measurement (Courtesy of Femtotools).....	87
Figure 5.1: Schematic diagram of the μ HRG	88
Figure 5.2: Lumped parameter model of a capacitive transducer.....	89
Figure 5.3: Electrostatic deflection Vs. DC voltage	90
Figure 5.4: Electromechanical model of μ HRG in COMSOL	90
Figure 5.5: Electromechanical model of μ HRG: cross section of single electrode	91
Figure 5.6: Simulated hemispherical shell deformation in response of 40 V DC voltage	91
Figure 5.7: Simulated static displacement of hemispherical shell Vs. applied DC bias voltage.....	92
Figure 5.8: Simulated electrostatic tuning curve	94
Figure 5.9: Electrode configuration for frequency domain simulation.....	95
Figure 5.10: Simulated resonance peak by frequency sweeping	95
Figure 5.11: Simulated drive amplitude Vs quality factor.....	96
Figure 6.1: Microfabrication process flow of polysilicon μ HRG: Step a) to d).....	103
Figure 6.2: High aspect-ratio trenches in silicon	103
Figure 6.3: Silicon nitride and polysilicon refilled trench	104
Figure 6.4: Microfabrication process flow of polysilicon μ HRG: Step e) to h).....	105
Figure 6.5: Hemispherical mold with polysilicon electrodes and backside hole.....	106
Figure 6.6: Through hole viewed from front side for DC bias	106
Figure 6.7: Microfabrication process flow of polysilicon μ HRG: Step i) to l).....	107
Figure 6.8: AFM surface topography measurement of (left) in-situ boron doped polysilicon and (right) undoped polysilicon	108
Figure 6.9: Wafer level fabrication of polysilicon μ HRG	109
Figure 6.10: Bird eye view of a fabricated polysilicon μ HRG	110
Figure 6.11: Cross section view of a fabricated polysilicon μ HRG (with shell on).....	110

Figure 6.12: Cross section view of a fabricated polysilicon μ HRG (with shell off)	111
Figure 6.13: Zoomed-in view of a fabricated polysilicon μ HRG.....	111
Figure 6.14: Modified process flow for front side DC bias contact	113
Figure 6.15: Fabricated polysilicon μ HRG with front side DC bias contact.....	113
Figure 6.16: Zoomed-in view on the front side DC bias contact.....	114
Figure 7.1: Layout of interface PCB.....	119
Figure 7.2: Image of the adaptor board.....	120
Figure 7.3: A polysilicon μ HRG with all 16 electrodes bonded to the interface PCB ...	120
Figure 7.4: Assembled interface PCB (with device in on-board vacuum chamber) and adaptor board	121
Figure 7.5: Frequency response of μ HRG showing various resonance modes	121
Figure 7.6: $m=2$ Resonance mode of μ HRG	122
Figure 7.7: Frequency mismatch between two degenerate modes at 10 V DC	122
Figure 7.8: Electrostatic tuning curve of $m=2$ resonance modes.....	123
Figure 7.9: Schematic illustration of the tuning electrodes	124
Figure 7.10: The two peaks as their being matched with a 27 Hz and 5 Hz frequency mismatch.....	124
Figure 7.11: Schematic illustration of mode matching of μ HRG at 6.6 kHz	125
Figure 7.12: Testing setup for rate sensitivity	125
Figure 7.13: Rate sensitivity measurement circuit architecture.....	126
Figure 7.14: Transient response to a sinusoidal rotation input	127
Figure 7.15: Scale factor of a mode matched polysilicon μ HRG.....	127
Figure 7.16: Quality factor of different modes of polysilicon μ HRG	128
Figure 7.17: Strain energy distribution in a long stem that supporting the hemispherical shell.....	128
Figure 7.18: Illustration on support loss estimation.....	129
Figure 7.19: Support structure optimization: long stem	131

Figure 7.20: $m=2$ mode for a polysilicon μ HRG with long stem	131
Figure 8.1: Process flow for μ HRG supported by long stem.....	135
Figure 8.2: Fabricated μ HRG supported by long stem	136
Figure 8.3: Fabricated μ HRG supported by long stem (shell broken).....	137

LIST OF SYMBOLS AND ABBREVIATIONS

MEMS	Microelectromechanical systems
WAG	Whole angle mode gyroscopes
RIG	Rate integrating mode gyroscopes
3D	Three-dimensional
2D	Two-dimensional
Q	Quality factor
HRG	Hemispherical resonating gyroscope
HSR	Hemispherical shell resonator
FOG	Fibre optic gyroscope
RLG	Ring laser gyroscope
CVG	Coriolis vibratory gyroscope
DOF	Degree of freedom
SEM	Scanning electron microscope
SOI	Silicon on insulator
SOG	Silicon on glass
PRG	Polysilicon ring gyroscope
BAW	Bulk acoustic wave
BW	Bandwidth
FEA	Finite element analysis
RAM	Random-access memory
TED	Thermoelastic damping
PML	Perfectly matched layer
PMM	Perfectly matched medium
XPS	X-ray photoelectron spectroscopy
PMMA	Poly(methyl methacrylate)

EDM	Electrical discharge machining
ALD	Atomic layer deposition
HNA	HF:Nitric:Acetic etch
ICP	Inductively coupled plasma
PECVD	Plasma enhanced chemical vapor deposition
HF	Hydrofluoric acid
XeF ₂	Xenon difluoride
SF ₆	Sulfur hexafluoride
C ₄ F ₈	Octafluorocyclobutane
TiN	Titanium nitride
Pt	Platinum
BOX	Buried oxide layer
AFM	Atomic force microscopy
TIA	Trans-impedance amplifier
SiO ₂	Silicon dioxide
TCF	Temperature coefficient of frequency
PZT	Lead Zirconate titanate
DC	Direct current
AC	Alternating current
DRIE	Deep reactive ion etching
LPCVD	Low pressure chemical vapor deposition
CHF ₃	Fluoroform
IR	Infrared
O ₂	Oxygen
SiH ₄	Silane
BCl ₃	Boron trichloride
PCB	Printed circuit board

SUMMARY

MEMS gyroscopes are electromechanical devices that measure rate or angle of rotation. They are one of the fastest growing segments of the microsensor market. Advances in microfabrication technologies have enabled the implementation of chip scale monolithic gyroscopes (MEMS gyroscopes) with very small form factor that are lightweight and consume little power. Over the past decade, significant amount of research have been directed towards the development of high performance and very small size MEMS gyroscopes for applications in consumer electronics such as smart phones.

One of the most promising application of MEMS gyroscopes is personal navigation in the absence of GPS signal. The main limitation of MEMS gyroscope as a navigation device is its excessive bias drift, which will be integrated over time and cause an angular position error. This issue will require GPS to kick in every once in a while for position reset and calibration.

Whole angle gyroscopes (WAG), which are also referred to as rate integrating gyroscopes (RIG) have the ability to output the angle of rotation directly instead of angular velocity, providing a path to eliminate the integration errors and reduce the drift of the gyro. Moreover, the dynamic range of a RIG is not limited by the bandwidth of its mechanical system. In another word, it is a more stable gyroscope with a large dynamic range. However, it requires a low frequency, ultra high quality factor axial symmetric structure, which is challenging to achieve in microscale. By shrinking the size of the resonator, resonance frequencies tend to increase as they are typically inversely proportional to the critical dimension of the structure. Classic scaling laws also predict a proportional relationship between mechanical quality factor and critical dimension. Therefore, integrated ultra-high Q RIG microchips have not been demonstrated in a footprint small (a few millimeters on a side). This work demonstrates a path towards that goal.

In this dissertation, high aspect-ratio hemispherical shell structure with continuously curved surface is utilized as the high Q resonator. Being an axial symmetric structure, the 3D hemispherical shell is able to achieve low frequency (3 ~ 5 kHz) within

2 mm X 2mm die area. Detailed analysis on energy dissipation also shows its potential to achieve ultra-high quality factor with the selection of high Q material and proper design of support structure.

This dissertation presents, for the first time, the analysis, design, fabrication and characterization of a micro-hemispherical resonating gyroscope (μ HRG) that has the potential to be used as a whole angle micro-gyroscope. A three-dimensional high aspect-ratio poly- and single crystalline silicon (3D HARPSS) process is developed to fabricate free-standing, stem-supported hemispherical shell with self-aligned deep electrodes for driving, sensing and quadrature control of the gyroscope. This monolithic process consists of seven lithography steps and combines 3D micro-structure with curved surfaces with the HARPSS process to create capacitive electrodes with arbitrary gaps around the micro-hemispherical shell resonator (μ HRSR). Polysilicon is utilized as the structural material due to its isotropic mechanical properties and the potential of achieving high quality factor.

The fabrication is demonstrated successfully by prototypes of polysilicon μ HRG with diameter of 1.2 mm and thickness of 700 nm. Frequency response and gyro operation are electronically measured using the integrated electrodes. Quality factor of 8,500 is measured with frequency mismatch of 105 Hz. Electronic mode matching and alignment are successfully performed by applying tuning voltages and quadrature nulling voltages. An open loop rate sensitivity scale factor of 4.42 mV/ $^{\circ}$ /s was measured. Design and process optimization of the support structure improved the quality factor to 40,000. Further improvement of quality factor will enable the demonstration of high performance RIG using polysilicon μ HRG.

CHAPTER 1

INTRODUCTION

1.1 Introduction to Gyroscopes

A gyroscope is a sensor that can measure angular velocity or angular position of one or multiple axes. German Johann Behnenberger demonstrated the first gyroscope instrument that was made of a rotating heavy ball in 1810. In 1832, American Walter R. Johnson invented a similar device based on the principle of a rotating disc. The name “gyroscope” is given by Leon Foucault in 1852 after he demonstrated the measurement of the Earth rotation [1]. Since then, with more than a century’s development, traditional gyroscopes are now widely used in inertial navigation, platform stabilization, unmanned aerial vehicles, gyro-theodolites in tunnel mining, etc. Modern MEMS/semiconductor technology enables building a gyroscope on a silicon chip. Nowadays, we are able to find gyroscopes not only on ships, missiles, airplanes, but in smart phones, gaming consoles, cameras and other portable devices [2] as well. All gyroscopes falls in three categories: Mechanical gyroscope, optical gyroscope and Coriolis vibratory gyroscope.

1.1.1 Mechanical Gyroscopes

The conventional mechanical gyroscopes are based on the conservation of angular momentum of a spinning wheel [3]. As Figure 1.1 shows, the spinning wheel is supported by gimbal structure and gyroscope frame, allowing rotating about multiple axes. Figure 1.2 illustrates the law of gyroscope, and precession will cause the rotation of the gimbal relative to inertial space. Considering the wheel is spinning along the axis ss' , and a torque is also applied on axis tt' . Then the spin axis of the disc will be forced to turn about axis pp' . The direction of ss' , tt' , pp' follow right hand rule. By supporting the spinning wheel with different sets of gimbals, single axis or two axis gyroscope can be made.

Professor C. S. Draper at the Massachusetts Institute of Technology did excellent work on this type of mechanical gyroscopes. The resolution this type of devices range from $0.001^\circ/\text{hr}$ to $10^\circ/\text{hr}$ depending on the actual design. Also, very high dynamic range of $500^\circ/\text{s}$ is also achieved [4]. However, the disadvantage of spinning wheel mechanical gyroscopes is that they require relative motion between two mated parts. The friction between two parts will caused wear and thus affect the long-term stability. Therefore, manufacturing and maintenance of this device increases the overall cost.

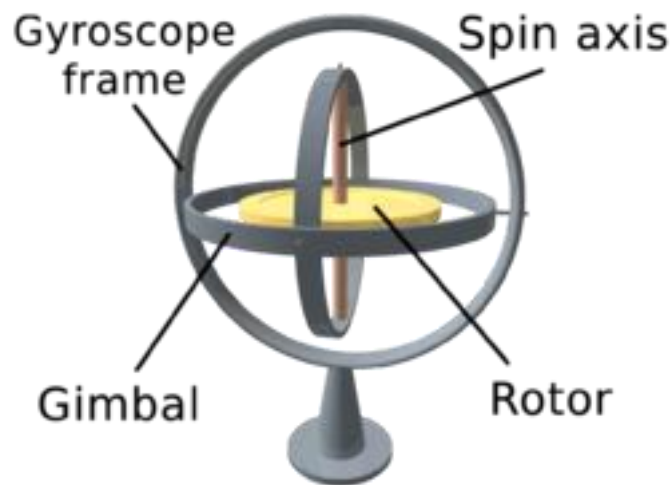


Figure 1.1: A mechanical gyroscope Structure (Source: Wikipedia)

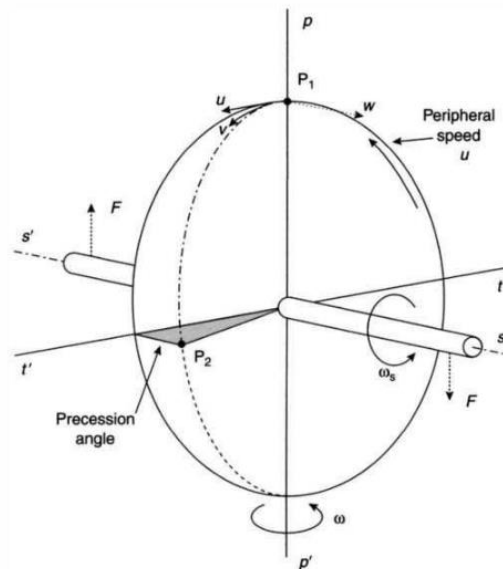


Figure 1.2: Illustration of gyroscope precession [4]

1.1.2 Optical Gyroscopes

The physical phenomenon of optical gyroscopes are the Sagnac effect [5], which is named after French physicist Georges Sagnac. It relates interferometer fringe shift to rotation rate. Fiber optic gyroscopes (FOG) and ring laser gyroscopes (RLG) are two typical optical gyroscopes. In fiber optic gyroscopes (FOG), two light waves circulate in opposite directions around a path as figure 1.3 shows. Assuming the light source is rotating clockwise, so the light traveling in the opposite direction (counter clockwise) will have shorter optical path compared to the other beam (clockwise). The phase difference between the two beams causes interference patterns to shift. The sensitivity is proportional to the total length of the circular fiber, and inverse proportional to the wavelength of the light. Figure 1.4 shows the latest open loop FOG design by KVH [6]

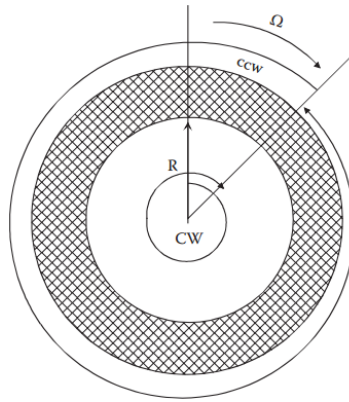
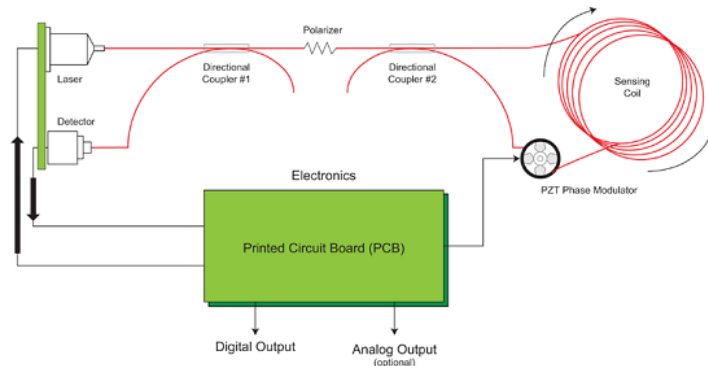


Figure 1.3: Illustration of Sagnac effect [7]



RED: KVH-manufactured polarization-maintaining, elliptical core, single mode optical fiber
GREEN: Printed circuit boards

Figure 1.4: Open loop design of fiber optic gyroscope [6]

Ring laser gyroscope (RLG) is another type of optical gyroscope, which consists of a Fabry-Perot resonator with three or more mirrors. The light is circulating through helium-neon as the gain medium, generating two laser beams, one traveling in the clockwise direction and one in the counterclockwise direction. The optical path length of the cavity is fine-tuned to be an integral multiple of the laser wavelength. When the device is at stationary, the frequencies of the two beams are equal, forming a standing wave. When the gyro is rotating about the axis perpendicular to the lasing plane, a difference of frequency between the two beams is created due to the constant light speed. The frequency difference will produce a beat frequency, taking the form of a fringe pattern which can be detected by photodiodes.

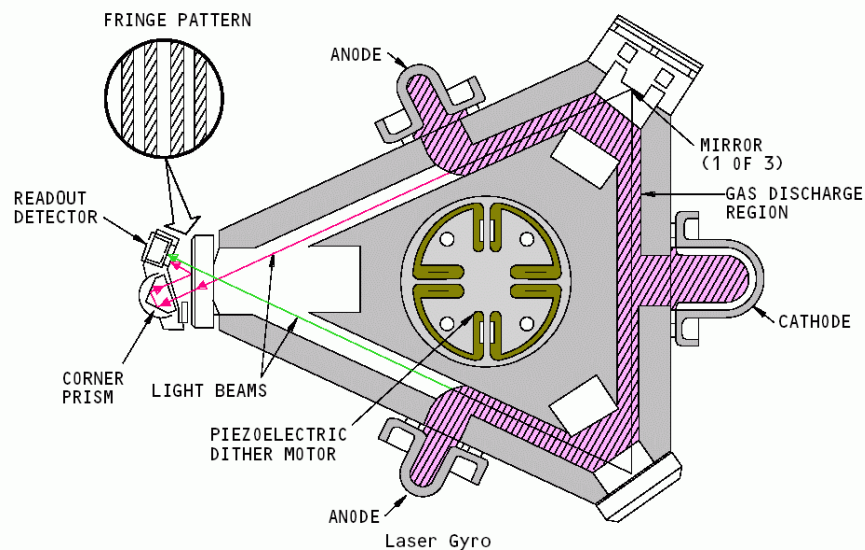


Figure 1.5: A ring laser gyroscope [8]

The biggest advantage of optical gyroscopes is free of moving parts, thus reduces the wearing of the device. And starting up the sensor only requires a few seconds [8]. However, these type of gyroscopes require highly precise assembly of lasers, optical mirrors and detectors, resulting in high assembly and maintenance cost. The requirement of long optical path for high performance also makes it bulky.

1.1.3 Coriolis Vibratory Gyroscope

Coriolis vibratory gyroscopes (CVG) are based on Coriolis effect, found by French scientist Gaspard-Gustave Coriolis in 1835. However, it was not until 1948 that people realized Coriolis effect can be used for gyroscope. Diptera, one kind of flying insect, is controlling itself with its halteres, which is actually a tuning fork gyroscope [9]. Coriolis vibratory gyroscope usually consists of a structure that has two orthogonal resonating modes, between which energy will be transferred due to Coriolis effect. This type of gyroscope will be the main focus of this dissertation, and the detailed working principle will be introduced in next section.

Systron Donner Quartz Rate Sensor (QRS) is illustrated in Figure 1.6. It is an “H” shaped tuning fork design, which is supported at the middle of the structure. Piezoelectric quartz material is used to simplify the sensing element, resulting in exceptional stability over temperature and time. The two tines on the top are driven in resonance out of phase in the plane of the structure. When there is a rotation along the input axis, the two bottom tines will resonate out of the plane of the structure. The best product has shown a bias stability of $0.035^\circ/\text{hr}$ [10].

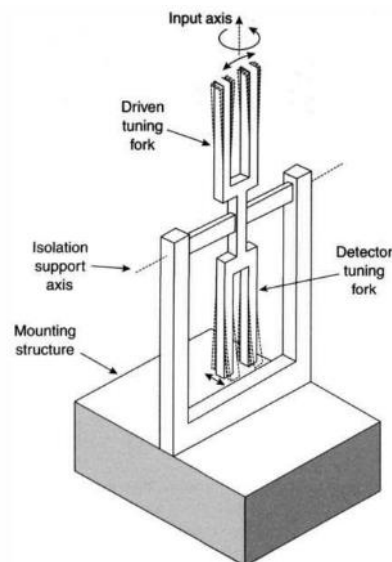


Figure 1.6: Tuning fork gyroscope

Another successful design of Coriolis vibratory gyroscope is the famous hemispherical resonator gyroscope (HRG) by Northrop Grumman Corporation (previously Litton Industries, Delco). In 1890, the physicist G. H. Bryan found when he stuck a wineglass and rotated it about its stem, the tone behaved interestingly and this could detect rotation [11]. But it wasn't until 1965 that the idea implemented at Delco. Dr. David Lynch, the god father of HRG, was leading a group developing this new type of inertial sensor for navigation. Nowadays, after the research and development of a few decades, HRG is now widely used for spacecraft stabilization, precision pointing, aircraft navigation, strategic accuracy systems, oil borehole exploration and planetary exploration [12].



**Figure 1.7: Hemispherical Resonator Gyroscope (HRG) Assembly
(Source: Northrop Grumman Corporation)**

As figure 1.7 shows, a HRG consists of a precision-machined highly symmetric hemispherical shell resonator made of an ultra-high-Q material such as fused quartz, with manually-assembled and fine-tuned electrodes. A zoomed-in view of the resonating part of hemispherical shell resonator (HSR) is illustrated in figure 1.8. The conventional 130P HRG which has the case diameter of 2.2 in and weight 0.64 lb with 64 separate parts, demonstrates bias stability smaller than $0.0005^\circ/\text{hr}$. The most latest milli HRG has case

diameter of 1.4 in and weight 0.25 lb with only 5 separate part. It shows bias stability of 0.00035°/hr [13].



Figure 1.8: Fused quartz hemispherical shell resonator (HSR)
(Source: Northrop Grumman Corporation)

1.2 Working Principle of CVG

1.2.1 Coriolis Effect

Coriolis force is a fictitious force that acts on moving objects when it is viewed in a rotating reference frame. It is named after French scientist Gaspard-Gustave Coriolis in 1835 when he wrote a paper derive the mathematical expression of Coriolis effect [14]. As figure 1.9 shows, assuming inertial frame A and rotating frame B, the absolute acceleration of a point mass in A can be written as follows

$$\vec{a} = \vec{A} + \vec{a}_B + \dot{\vec{\Omega}} \times \vec{r}_B + \vec{\Omega} \times (\vec{\Omega} \times \vec{r}_B) + 2\vec{\Omega} \times \vec{v}_B \quad (1.1)$$

The absolute acceleration of a point mass in A can be decomposed into: linear acceleration of frame B in frame A (\vec{A}), linear acceleration of the point mass in frame B (\vec{a}_B), rotation acceleration ($\dot{\vec{\Omega}} \times \vec{r}_B$), Centrifugal acceleration ($\vec{\Omega} \times (\vec{\Omega} \times \vec{r}_B)$), and Coriolis acceleration ($2\vec{\Omega} \times \vec{v}_B$). Among these component, the first two terms are linear acceleration, and can be treated as common mode. And rotation acceleration and centrifugal acceleration can also be ignored because they are higher order terms. Equation (1.1) introduces the fact

that, if the observer is standing in the rotating frame, he or she should be able to observe a force whose direction is perpendicular to the angular velocity and relative velocity of the object with respect to the rotating frame.

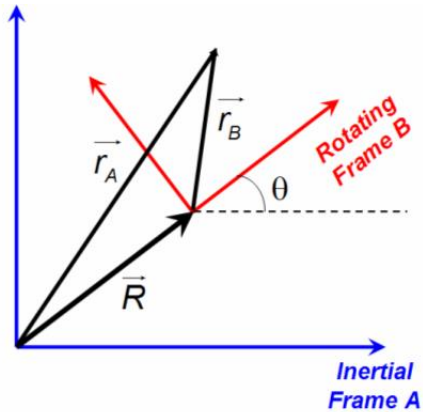


Figure 1.9: Inertial frame and rotating frame [15]

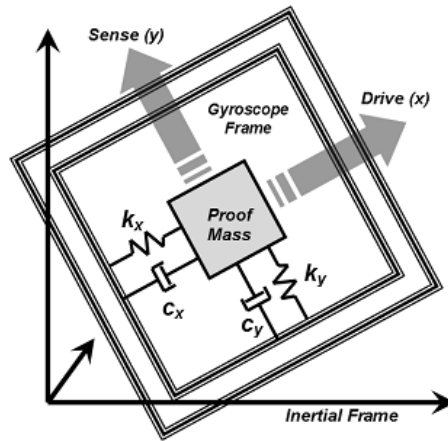


Figure 1.10: Illustration of a single proof-mass CVG [15]

Figure 1.10 illustrated a lumped parameter model of a single proof-mass Coriolis vibratory gyroscope. In theory, it is a simplified 2DOF mass-spring-damper system. The proof-mass is supported by two sets of spring and damper on two orthogonal directions, respectively. And the system is driven into resonance on x direction which is the drive axis. When there is an out-of-plane angular rotation, a displacement on y direction which is the

sense axis will be detected. Currently, the electrical transduction of driving and sensing is performed by either capacitance or piezoelectricity.

1.2.2 Mode of Operation

Coriolis vibratory gyroscopes have two operation mode: rate mode and whole angle mode (rate integrating mode) [16]. In rate mode, the readout signal is angular rate. In figure 1.10, the proof-mass is driven sinusoidally along drive axis. Coriolis effect will generate a displacement along sense axis, and the dynamics of the mass can be described by the following differential equations:

$$\begin{cases} m\ddot{x} + C_x\dot{x} + k_x x = F_0 \sin \omega_n t \\ m\ddot{y} + C_y\dot{y} - 2m\Omega\dot{x} + k_y y = 0 \\ x(0) = \dot{x}(0) = y(0) = \dot{y}(0) = 0 \end{cases} \quad (1.2)$$

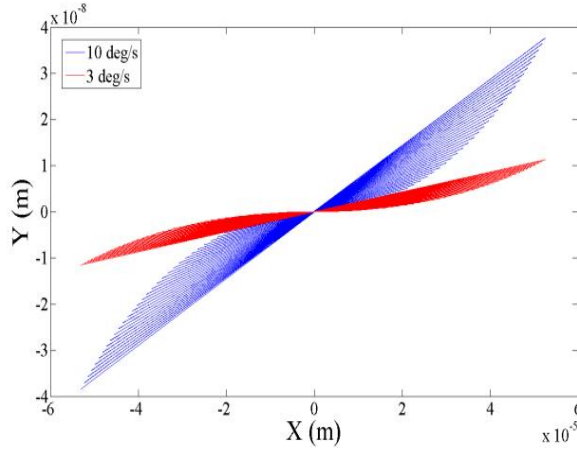


Figure 1.11: Dynamics of a rate mode CVG

Equation (1.2) assumes drive mode and sense mode have the same resonance frequency, i.e. the CVG is operated at mode-matched condition. The advantage of disadvantage of mode matching will be introduced in the next section. In equation (1.2), the term $F_0 \sin \omega t$ is the sinusoidal drive force, and $2m\Omega\dot{x}$ is the Coriolis coupling term from x axis to y axis. The Coriolis coupling term from y axis to x axis is always three orders of magnitude smaller, thus it is ignored in equation (1.2). All initial conditions are set to zero. By solving the system of differential equations, the dynamics of the proof-mass in

the response of 3°/s and 10°/s angular rate are plotted respectively in figure 1.11. As we can see, the Coriolis signal is proportional to angular rate. Thus, integration over time is needed for angular position. Moreover, it is noticeable that the system need finite time to respond and stabilize. Therefore, the dynamic range of this type of gyroscope is limited by the system bandwidth.

Another mode of operation is called whole angle mode or rate integrating mode. In this mode of operation, proof-mass is given an impulse and allowed to vibrate freely. Coriolis effect causes vibration pattern to precess. The dynamics of the mass can be described by the following differential equations:

$$\begin{cases} m\ddot{x} + C_x\dot{x} + k_x x + 2m\Omega\dot{y} = 0 \\ m\ddot{y} + C_y\dot{y} + k_y y - 2m\Omega\dot{x} = 0 \\ x(0) = A \\ \dot{x}(0) = \dot{y}(0) = \dot{y}(0) = 0 \end{cases} \quad (1.3)$$

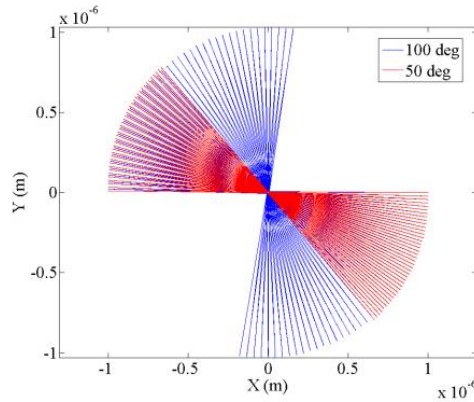


Figure 1.12: Dynamics of a rate integrating gyroscope (RIG)

As we can see in equation (1.3), the Coriolis coupling term is in both equations, which means the coupling is in both ways. And at time zero, the mass is given a finite drive amplitude and zero velocity. After that, there is no external force in the system. Usually, rate integrating gyroscopes (RIG) have a very high mechanical quality factor of resonance. Thus, the damping term is negligible. The stiffness on two axis is also assumed to be identical. Figure 1.12 demonstrates the dynamics of a rate integrating mode gyroscope in response of 50° and 100° rotation. The angle ϕ that the mass rotates is proportional to

the angle that the system rotates and can be directly determined from the instantaneous position and velocity by equation (1.4). The advantage is obvious that no integration error will be introduced over time, and dynamic range is not limited by the system bandwidth.

$$\tan 2\phi = \frac{2(\omega_n^2 xy + \dot{x}\dot{y})}{\omega_n^2(x^2 - y^2 + (\dot{x}^2 - \dot{y}^2))} \quad (1.4)$$

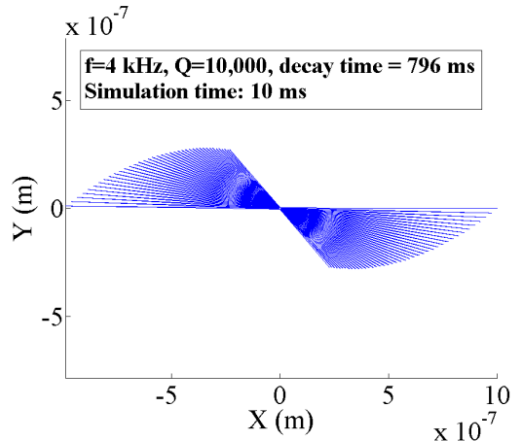


Figure 1.13: Dynamics of a rate integrating gyroscope with finite quality factor

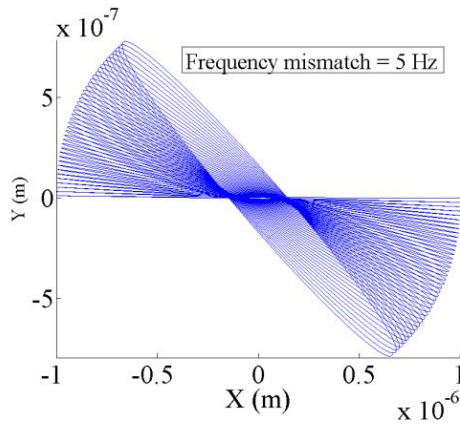


Figure 1.14: Dynamics of a rate integrating gyroscope with finite frequency mismatch

However, gyroscopes that operated in rate integrating mode have very high requirement on the performance of the resonator. First, it requires a high ringdown time, which translates into low frequency and high quality factor. Figure 1.13 shows the dynamics of a rate integrating gyroscope with finite quality factor. The vibration amplitude decays as time goes by, so another excitation will be needed more frequently. And this will

affect system nonlinearity. Second, it requires a highly isotropic oscillator with fully matched drive and sense modes. Figure 1.14 shows the dynamics of rate integrating gyroscope with finite frequency mismatch. The elliptical shape trajectory causes large quadrature error during gyroscope precession [17]. The angular position information cannot be solved by equation (1.4), thus the gyroscope is not usable.

1.2.3 Mode Matching

As discussed in previous section, rate integrating gyroscopes (RIG) need fully matched drive and sense mode, which means the peak of one of the modes needs to be within the 3dB bandwidth of the other mode. Since rate integrating gyroscopes are usually with high Q at low frequency, the bandwidth is very small. Assuming the resonator has a Q of 100,000 at 5 kHz, the bandwidth will be only 50 mHz. This requires highly stable electronics, which is a big challenge at system level.

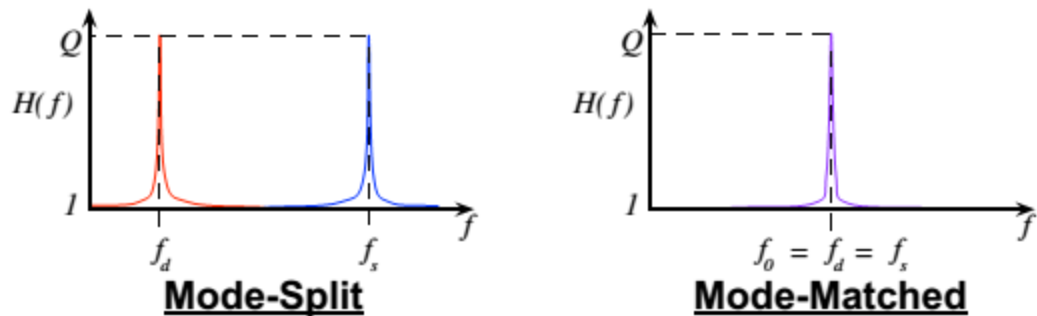


Figure 1.15: Split mode operation and matched mode operation

Rate mode gyroscopes can work at either mode matched condition [18] or split mode condition [19]. In split mode operation, the sense mode is operated at a different frequency from the drive mode, resulting in partial energy transfer between the two modes. The advantage of mode matching is that, the Coriolis signal is amplified not only by drive mode quality factor, but sense mode quality factor as well, resulting in higher sensitivity. However, due to fabrication imperfection the two modes are never matched as fabricated. Thus, a tuning or trimming mechanism needs to be implemented to match the two modes.

Some mode matched MEMS gyroscopes are intentionally designed with an initial split between the two modes, and use electrostatic spring softening effect for fine tuning and mode matching [20]. Figure 1.13 illustrates split mode operation and matched mode operation.

1.3 MEMS Gyroscopes

Nowadays, most MEMS gyroscopes are Coriolis Vibratory Gyroscope (CVG). The working principle is as described in the previous section. However, the structural design could be quite different due to different application and processing technologies. Overall, the structure of MEMS gyroscope can be divided into two categories: degenerate mode gyroscope and non-degenerate mode gyroscope. Degenerate mode gyroscope is usually an axisymmetrical structure with its fundamental modes used as drive mode and sense mode. The drive mode and corresponding sense mode are of the same order and orthogonal, which means the nodes of drive mode locate at the anti-nodes of sense mode and vice versa. Thus they are inherently matched if without fabrication imperfection. Non-degenerate mode gyroscope usually consists of one or multiple proof-masses which are supported by carefully designed tethers to allow two-degree-of-freedom motion. Since the tethers at drive and sense direction are different, they are not degenerate modes.

1.3.1 Non-degenerate Mode Gyroscope

The first batch-fabricated silicon micromachined vibratory gyroscope was demonstrated by the Charles Stark Draper Laboratory in 1991 [21]. This silicon bulk mechanical device was a double-gimbal vibratory gyroscope supported by torsional flexure structures. In this design, an outer gimbal was electrostatically excited at constant amplitude using drive electrodes. In the presence of rotation perpendicular to the plane of the device, this oscillatory motion was transferred to the inner gimbal along the still axis of the inner flexures. Two years later in 1993, the Charles Stark Draper Laboratory reported

a silicon-on-glass tuning fork gyroscope [19] fabricated through the dissolved wafer process [22]. This gyroscope was electrostatically vibrated in its plane using a comb drive actuator. The applied rotation signal normal to the drive mode would then excite the out-of-plane rocking mode of the structure which was capacitively monitored.

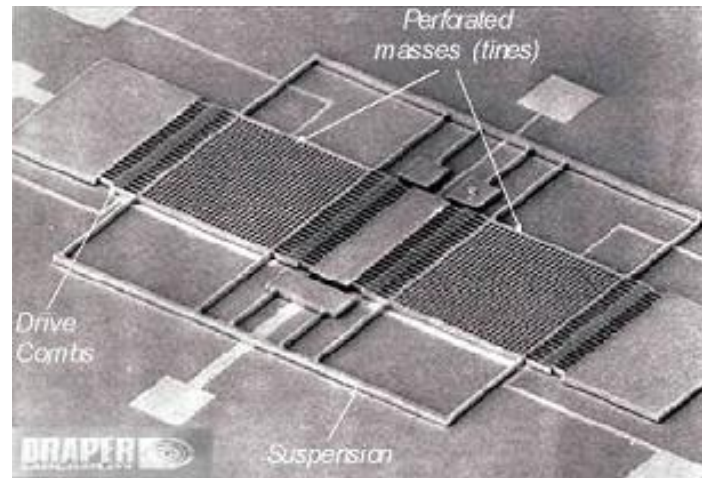


Figure 1.16: SEM of Draper's silicon on glass tuning fork gyroscope [19]

A first mode matched tuning fork gyroscope was reported by Georgia Tech [18, 20], with high quality factor for both in plane drive mode and sense mode. It is fabricated on a silicon-on-insulator (SOI) wafer by a backside release technique. As figure 1.14 shows, the two tines of the tuning fork is driven by comb drive along x axis. In order to balance the drive mode, four quadrature nulling electrodes are applying a torque to the structure by DC voltages. Parallel plate capacitor is used for sensing electrodes. The resonance frequency of sense mode is design intentionally slightly higher than drive mode. Due to electrostatic spring soften effect on parallel plate capacitors, resonance frequency of sense mode will shift towards low frequency as polarization voltage increase while resonance frequency of drive mode is not affected. At some point, the tuning fork gyroscope reaches mode matched condition. With the mode matched condition, bias drift below $1^\circ/\text{h}$, and scale factor of $88 \text{ mV}/^\circ/\text{s}$ is measured. The system bandwidth is usually below 1 Hz in the mode matched condition of high quality factor at low frequency.

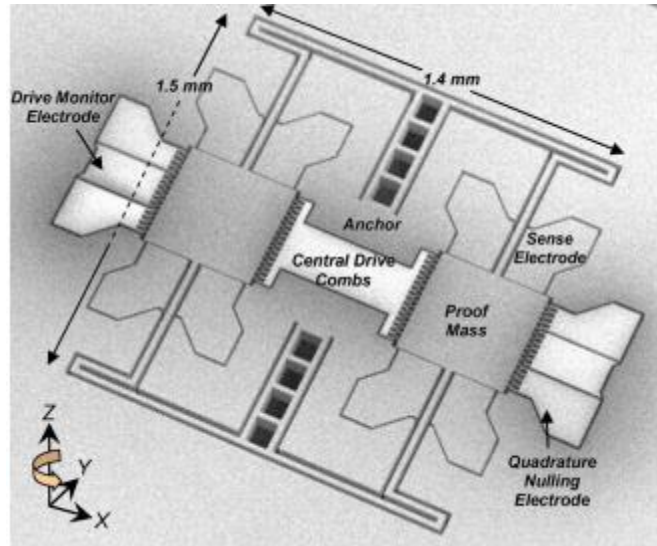


Figure 1.17: SEM of Georgia Tech mode matched tuning fork gyroscope [18]

The Coriolis signal of a MEMS gyroscope is generally much smaller than drive mode signal. Due to various cross-coupling mechanisms between drive and sense mode, the actual mode shape is not perfectly orthogonal. Even smaller amount of offset will saturate the sense signal. This is called quadrature error. Even though quadrature error is 90° phase difference with the Coriolis signal, there is no perfect electronic filter can filter out quadrature signal. In order to reduce the amount of quadrature signal, decouple mass design is proposed.

UC Irvine reported a novel micromachined gyroscope design that provides enhance decoupling of the drive and sense modes, and increased actuation and detection mechanism minimizes the effects of fabrication imperfections and the resulting anisoeastics, by utilizing independent folded flexures and constrained moving electrodes in the drive and sense modes [23]. The post-release capacitance enhancement concept aims to increase the drive and sense capacitance beyond the minimum trench width limited by photolithography. Bulk-micromachined prototype gyroscopes were fabricated, and the experimental results demonstrated a noise floor of $0.25^\circ/\text{s}/\sqrt{\text{Hz}}$ with 50 Hz bandwidth in atmospheric pressure.

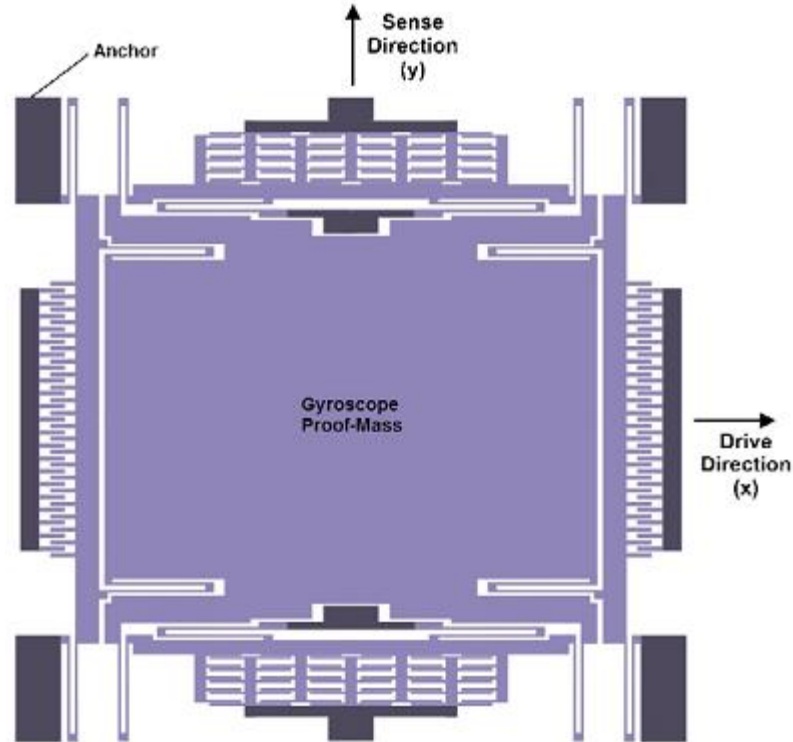


Figure 1.18: UC Irvine's decoupled gyroscope [23]

Researchers from the Middle East Technical University in Turkey presented symmetrical and decoupled silicon micro gyroscopes by surface micromachined polysilicon [24] and bulk micromachined single crystal silicon using a dissolved wafer process [25]. A 100- μm -thick single-crystal silicon MEMS gyroscope based on SOI processing with an improved decoupling arrangement between the drive and sense modes was demonstrated in 2008 [26]. The scale factor is 22.2 mV/ $^{\circ}\text{/s}$, with a composite nonlinearity as small as 0.6% within the 50 $^{\circ}\text{/s}$ measurement range. The zero-rate bias of the sensor is less than 0.1 $^{\circ}\text{/s}$ after turning on, while the bias stability is measured to be 14.3 $^{\circ}\text{/h}$. The rate equivalent white-noise density of the gyroscope is measured to be better than 6.9 $^{\circ}\text{/h}/\sqrt{\text{Hz}}$.

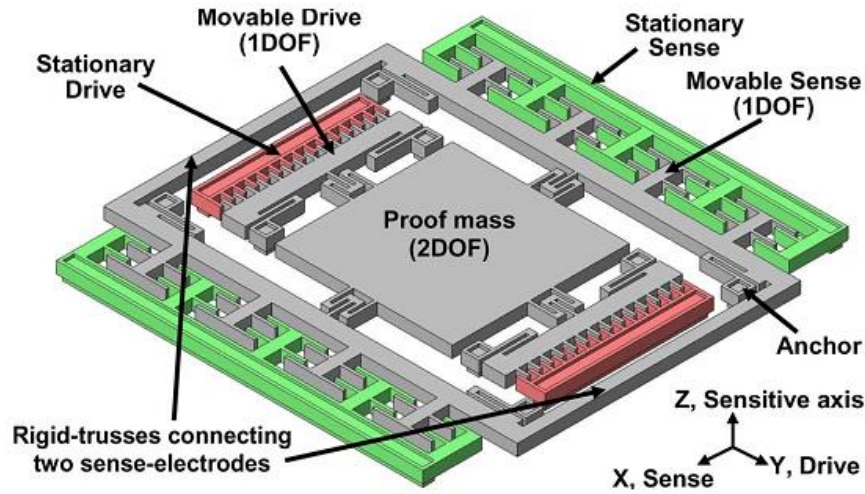


Figure 1.19: The Middle East Technical University’s decoupled gyroscope [27]

1.3.2 Degenerate Mode Gyroscope

The first MEMS gyroscope that is based on energy transfer between two degenerate modes of vibration was developed by University of Michigan [28]. A circular polysilicon vibrating ring with supporting tethers were fabricated by High Aspect-ratio Combined Poly and Single-crystal Silicon (HARPSS) process [29]. The polysilicon ring gyroscope (PRG) is 80 μm in thickness and 1.1 mm in diameter, with 20:1 aspect ratio. An open-loop sensitivity of 200 $\mu\text{V}/\text{deg/s}$ in a dynamic range of 250 deg/s was measured under low vacuum level for a prototype device tested in hybrid format. The resolution for a PRG with a quality factor (Q) of 1200, drive amplitude of 0.15 μm , and sense node parasitic capacitances of 2 pF was measured to be less than 1 deg/s in 1 Hz bandwidth. MEMS ring gyroscopes made out of other structural materials such as electroplated Nickel [30], single crystal silicon [31] are also reported.

University of Michigan reported a single crystal silicon cylindrical gyroscope, fabricated by Silicon-On-Glass (SOG) process which can provide deep (>300 μm), high aspect-ratio (>1:15), and narrow-gap (2 μm) silicon structures [32]. The gyroscope is operated at 3 kHz with quality factor of 100,000 in both rate mode and rate integrating

mode. Measurement result shows initial frequency mismatch of 7 Hz can be matched within 20 mHz by electrostatic tuning, and decay time is 8.7 seconds. The rate mode angle random walk was $0.09^\circ/\sqrt{\text{Hz}}$ with Allan Variance of $129^\circ/\text{hr}$ and an angular gain of 0.011.

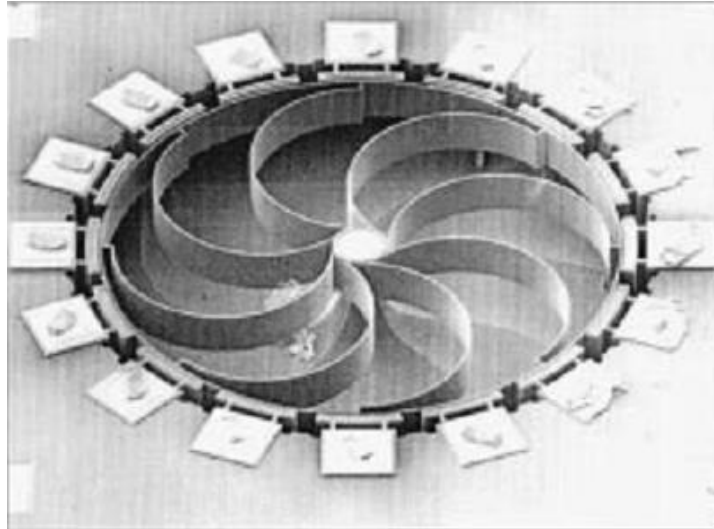


Figure 1.20: HARPSS polysilicon ring gyroscope by University of Michigan [28]

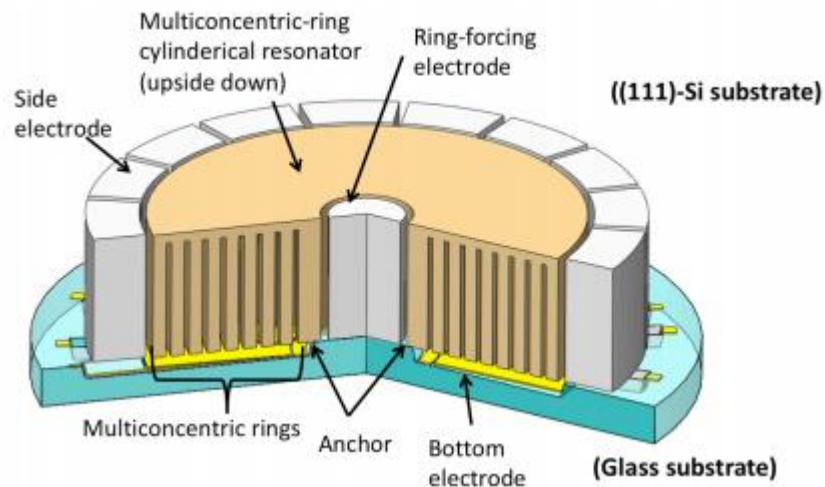


Figure 1.21: SOG silicon cylindrical gyroscope by University of Michigan [32]

Georgia Institute of Technology developed a Bulk Acoustic Wave (BAW) disk gyroscopes in single crystal silicon [33]. The capacitive BAW disk gyroscopes are stationary devices operating in their degenerative MHz-frequency bulk acoustic modes with very small vibration amplitudes (<20 nm). The ability of capacitively drive and sense these high frequency high stiffness devices is granted by HARPSS process, which can

generate sub-micron capacitive gap sizes (180 – 250 nm). The high frequency of the modes results in a large device bandwidth ($BW > 100$ Hz) under very high-Q ($Q > 100,000$) mode-matched condition. Since the BAW gyroscopes are solid state devices with very large stiffness, they exhibit superior shock resistance. Another advantage is BAW gyroscopes can operate at relatively high vacuum pressure or even in atmosphere, reducing the cost of vacuum packaging. The measurement on a 1200 μm diameter (111) silicon disk gyroscopes demonstrates a rate sensitivity of 0.32 mV/ $^\circ/\text{s}$ and bias instability of 17 $^\circ/\text{hr}$ [34]. Other BAW gyroscopes based on degenerate modes of vibration are also reported by Georgia Institute of Technology, such as annulus supported by spoke [35] and piezoelectric square [36].

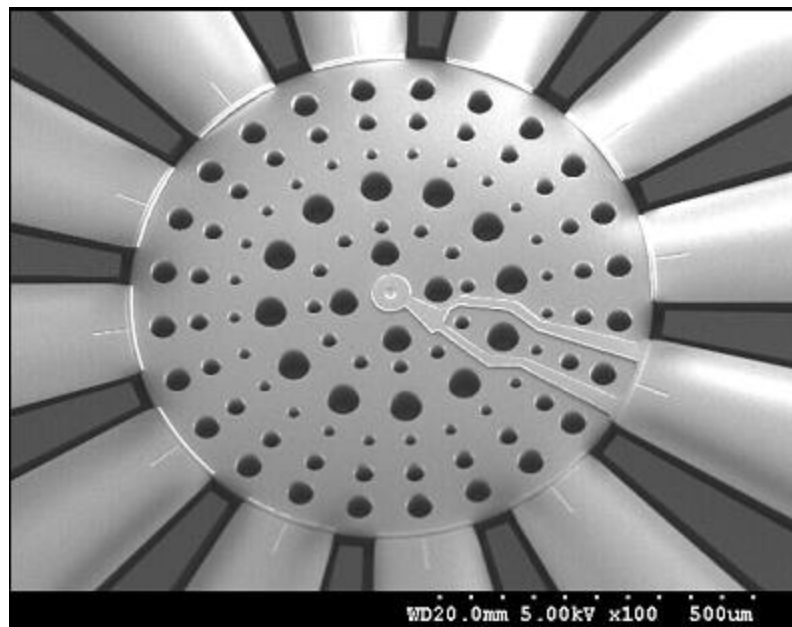


Figure 1.22: Bulk acoustic wave (BAW) silicon disk gyroscope by Georgia Institute of Technology [37]

1.4 Why Hemisphere

As introduced in section 1.1, hemispherical resonator gyroscope (HRG) is one of the most successful designs for navigation grade gyroscope, which has been widely used in high value space missions. The physical principle of the HRG is based on the inertial properties of elastic waves propagating in a solid object. The undisputable advantages of

these existing instruments are their high sensitivity, environmental stability, and robust operation over time. A disadvantage is their extremely high cost and large size. With the latest advances in micro-fabrication technology and the development of MEMS inertial sensors, there is a possibility that the conventional HRG can be miniaturized down to chip scale.

One of the advantages of HRG is that it can be operated at rate integrated mode (RIG), which is made possible by its low resonance frequency, ultra high quality factor and extreme axial symmetry. At the range of low frequency, axial symmetric structures such as circular ring [28], cylinder [32] have been fabricated. However, low frequency resonators always require much larger structure. For some planar structures, the overall footprint approaches or exceeds 1 cm X 1 cm [32, 38]. The curved three dimensional structure of μ HRG allows low resonance frequencies (< 8 kHz) at extremely small sizes with 1/100 area reduction compared to its planar counterparts.

Moreover, the 3D curved structure of hemispherical shell has less coupling between the vibration mode and the support structure compared to other planar axial symmetric structures, thus has the potential of higher mechanical quality factor. The structure is also expected to demonstrate low stiffness, which would enable large reference vibration amplitudes with large capacitive gaps, resulting in an improved mechanical noise floor and sensitivity. A large electrostatic tuning range will be another outcome of the low stiffness of the hemisphere structure.

1.5 Thesis Outline

This work explores the design, fabrication and testing of microscale hemispherical resonator gyroscopes (μ HRG). This thesis is organized as follows:

CHAPTER 1 briefly introduces the background of MEMS gyroscope, reviews the different type of gyroscopes and their operational principles.

CHAPTER 2 presents the design of microscale hemispherical shell resonator (μ HSR) for a low frequency, high quality factor axisymmetric resonator. Finite element analysis for resonance frequency, various energy dissipation mechanism and structure anisotropy is carried out

CHAPTER 3 introduces the microfabrication process for freestanding, stem-supported hemispherical shell that is electrically actuated by assembled electrodes. The fabrication results are also shown.

CHAPTER 4 shows the characterization results of microfabricated μ HSR. Quality factors are measured for different mode at various environment. Frequency mismatch is measured for different process parameters. The results demonstrate a structure promising for a high performance gyroscope.

CHAPTER 5 presents the electro-mechanical design and simulation of microscale hemispherical resonating gyroscope (μ HRG). Pull-in voltage, electrostatic tuning range, drive amplitude, Coriolis sensitivity is simulated for an efficient capacitive transducer design.

CHAPTER 6 introduces the microfabrication process for polysilicon μ HRG with self-aligned hemispherical shell and electrodes for drive, sense and control of the gyroscope. This integrated monowafers process consists of seven lithography steps and can be transferred to foundry for commercialization

CHAPTER 7 presents the testing results of fabricated μ HRG. Frequency response is measured by network analyser, demonstrating a high Q axial symmetric device. Mode matching is performed by applying tuning voltages and quadrature control voltages. Open loop rate sensitivity is then measured.

CHAPTER 8 introduces the future direction of this research for a high performance navigation grade rate integrating gyroscope.

CHAPTER 2

DESIGN AND SIMULATION OF MICROSCALE HEMISPHERICAL SHELL RESONATORS (μ HSR)

Micro-hemispherical shell resonator (μ HSR) is the beating heart of high performance μ HRG. The μ HSR is required to have high quality factor at low frequency (a few kHz) with high axisymmetry. In designing the μ HSR, various parameters will affect the performance. In this chapter, theory of a vibrating hemispherical shell is firstly introduced, followed by the simulation and analysis on energy dissipation and structural anisotropy of μ HSR.

2.1 Theory of a Vibrating Hemispherical Shell

The core part of a microscale hemispherical shell resonating gyroscope (μ HRG) is the hemispherical shell resonator (μ HSR), which works at its second axisymmetric vibrating mode. It is very important and necessary to analyze the vibration of the μ HSR in order to design the gyroscope. Figure 2.1 shows the geometric illustration of an inverted hemispherical shell, x is the central axis, $h(\varphi)$ is the shell thickness, R is the shell radius, φ_0 and φ_F are the starting and ending boundary angles, and E , μ , ρ are material Young's modulus, Poisson ratio and density, respectively. Assuming that the shell material is isotropic and homogeneous.

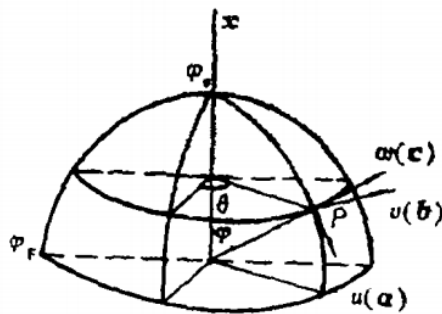


Figure 2.1: Geometric illustration of a hemispherical shell [39]

In figure 2.1, φ , θ and r are the longitudinal, circumferential and radial coordinates in spherical coordinate system. So the displacement of the arbitrary point P is

$$\vec{V} = u\hat{\varphi} + v\hat{\theta} + w\hat{r} \quad (2.1)$$

Where u , v , w are the longitudinal, circumferential, and radial displacements respectively, $\hat{\varphi}$, $\hat{\theta}$ and \hat{r} are the unit vector on each direction.

2.1.1 Strain of a Vibrating Shell

Considering a hemispherical surface z inside the shell with the distance z from the middle surface, its longitudinal normal strain ε_1^z , circumferential normal strain ε_2^z and the shear strain γ_{12}^z on z surface can be derived as [40]:

$$\begin{cases} \varepsilon_1^z = \frac{\varepsilon_1 + z\lambda_1}{1 + z/R} \\ \varepsilon_2^z = \frac{\varepsilon_2 + z\lambda_2}{1 + z/R} \\ \gamma_{12}^z = \frac{\gamma_{12} + z\tau}{1 + z/R} \end{cases} \quad (2.2)$$

The strain on the neutral surface is:

$$\begin{cases} \varepsilon_1 = \left(\frac{\partial u}{\partial \varphi} + w \right) / R \\ \varepsilon_2 = \left(\frac{\partial v}{\partial \theta} + u \cos \varphi + w \sin \varphi \right) / R \sin \varphi \\ \gamma_{12} = \left(\frac{\partial u}{\partial \theta} + \sin \varphi \frac{\partial v}{\partial \varphi} - v \cos \varphi \right) / R \sin \varphi \end{cases} \quad (2.3)$$

Other parameters can be written as:

$$\begin{cases} \lambda_1 = \left(-\frac{\partial^2 w}{\partial \varphi^2} + \frac{\partial u}{\partial \varphi} \right) / R^2 \\ \lambda_2 = \left(-\frac{1}{\sin^2} \frac{\partial^2 w}{\partial \theta^2} - \frac{\cos \varphi}{\sin \varphi} \frac{\partial w}{\partial \varphi} + \frac{\cos \varphi}{\sin \varphi} u + \frac{1}{\sin \varphi} \frac{\partial v}{\partial \theta} \right) / R^2 \\ \tau = \left[\frac{\partial v}{\partial \theta} + \sin \varphi \frac{\partial v}{\partial \varphi} - v \cos \varphi + 2 \left(\frac{\cos \varphi}{\sin \varphi} \frac{\partial w}{\partial \theta} - \frac{\partial^2 w}{\partial \varphi \partial \theta} \right) \right] / R^2 \sin \varphi \end{cases} \quad (2.4)$$

In the case of thin shell with $h(\varphi)/R \ll 1$, equation (2.2) can be simplified as,

$$\begin{cases} \varepsilon_1^z = \varepsilon_1 + z\lambda_1 \\ \varepsilon_2^z = \varepsilon_2 + z\lambda_2 \\ \gamma_{12}^z = \gamma_{12} + z\tau \end{cases} \quad (2.5)$$

2.1.2 Strain Energy and Kinetic Energy

The strain energy of the vibrating shell is:

$$U = \frac{1}{2} \int_V (\varepsilon_1^z \sigma_1 + \varepsilon_2^z \sigma_2 + \gamma_{12}^z \sigma_{12}) dV \quad (2.6)$$

Where V is the volume integration domain. According to Hook's Law in three dimension, stress of a vibrating hemispherical shell can be written as,

$$\begin{cases} \sigma_1 = \frac{E}{1-\mu^2} (\varepsilon_1^z + \mu\varepsilon_2^z) \\ \sigma_2 = \frac{E}{1-\mu^2} (\mu\varepsilon_1^z + \varepsilon_2^z) \\ \sigma_{12} = \frac{E}{2(1+\mu)} \gamma_{12}^z \end{cases} \quad (2.7)$$

The kinetic energy of the vibrating shell is:

$$T = \frac{1}{2} \int_V \left[\left(\frac{\partial u}{\partial t} \right)^2 + \left(\frac{\partial v}{\partial t} \right)^2 + \left(\frac{\partial w}{\partial t} \right)^2 \right] \rho dV \quad (2.8)$$

2.1.3 Mode Shape

Microscale hemispherical resonator gyroscope usually works at its m th axial symmetric vibrating shapes, which can be written as [39]

$$\begin{cases} u = u(\varphi) \cos m\theta \sin \omega_n t \\ v = v(\varphi) \sin m\theta \sin \omega_n t \\ w = w(\varphi) \cos m\theta \sin \omega_n t \end{cases} \quad (2.9)$$

$u(\varphi)$, $v(\varphi)$, $w(\varphi)$ are the vibrating shapes in longitudinal, circumferential and radial direction, and ω_n is the resonance frequency.

For the flexural modes with relative small vibration amplitude, Lord Rayleigh's inextensional theory is satisfied. Therefore, the strain on the neutral surface of the shell is zero:

$$\varepsilon_1 = \varepsilon_2 = \gamma_{12} = 0 \quad (2.10)$$

So, together with equation (2.3), (2.9) and (2.10), we can obtain the following equations:

$$\begin{cases} w(\varphi) = -\frac{du(\varphi)}{d\varphi} \\ mv(\varphi) + u(\varphi) \cos \varphi - \frac{du(\varphi)}{d\varphi} \sin \varphi = 0 \\ mu(\varphi) + v(\varphi) \cos \varphi - \frac{dv(\varphi)}{d\varphi} \sin \varphi = 0 \end{cases} \quad (2.11)$$

The solution of equation (2.11) is:

$$\begin{cases} u(\varphi) = \left(C_1 \tan^m \left(\frac{\varphi}{2} \right) - C_2 \cot^m \left(\frac{\varphi}{2} \right) \right) \sin \varphi \\ v(\varphi) = \left(C_1 \tan^m \left(\frac{\varphi}{2} \right) + C_2 \cot^m \left(\frac{\varphi}{2} \right) \right) \sin \varphi \\ w(\varphi) = - \left[C_1 (m + \cos \varphi) \tan^m \left(\frac{\varphi}{2} \right) + C_2 (n - \cos \varphi) \cot^m \left(\frac{\varphi}{2} \right) \right] \end{cases} \quad (2.12)$$

Assuming the hemispherical shell is anchored at position $\varphi = 0^\circ$, with the following boundary condition:

$$u(\varphi = 0^\circ) = v(\varphi = 0^\circ) = w(\varphi = 0^\circ) = 0 \quad (2.13)$$

Then the constant C_2 must be zero, equation (2.12) is:

$$\begin{cases} u(\varphi) = C_1 \sin \varphi \tan^m \left(\frac{\varphi}{2} \right) \\ v(\varphi) = C_1 \sin \varphi \tan^m \left(\frac{\varphi}{2} \right) \\ w(\varphi) = -C_1 (m + \cos \varphi) \tan^m \left(\frac{\varphi}{2} \right) \end{cases} \quad (2.14)$$

The above equation shows the mode shape of a hemispherical shell vibrating at its m th axial symmetric mode. The constant C_1 can be determined by the actual vibrating amplitude.

2.1.4 Resonance Frequency

Using the expression of mode shape, stress and strain, the strain energy and kinetic energy in equation (2.6) and (2.8) can be re-written as:

$$U = \frac{C_1^2 \sin^2 \omega_n t E \pi}{2(1 - \mu^2)} \frac{1}{12R^2} \int_{\varphi_0}^{\varphi_F} 4(1 - \mu)m^2(m^2 - 1)^2 \tan^{2m} \frac{\varphi}{2} \frac{h^3(\varphi)}{\sin^3 \varphi} d\varphi \quad (2.15)$$

$$T = \frac{C_1^2 \cos^2 \omega_n t}{2} \omega_n^2 R^2 \rho \pi \int_{\varphi_0}^{\varphi_F} (\sin^2 \varphi + 2n \cos \varphi + n^2 + 1) \sin \varphi \tan^{2m} \frac{\varphi}{2} h(\varphi) d\varphi \quad (2.16)$$

If assuming shell thickness is uniform across the whole geometry, natural frequency can then be obtained by $U_{\text{peak}} = T_{\text{peak}}$

$$\omega_m = \frac{m(m^2 - 1)}{R^2} \sqrt{\frac{E \cdot I(m, h)}{3(1 + \mu)\rho \cdot J(m, h)}} \quad (2.17)$$

Where,

$$I(m, h) = h^2 \int_{\varphi_0}^{\varphi_F} \frac{\tan^{2m}(\varphi/2)}{\sin^3 \varphi} d\varphi \quad (2.18)$$

$$J(m, h) = h \int_{\varphi_0}^{\varphi_F} (m^2 + 1 + \sin^2 \varphi + 2m \cos \varphi) \tan^{2m}(\varphi/2) d\varphi \quad (2.19)$$

Then the resonance frequency of a vibrating hemispherical shell is found to be proportional to the thickness of the shell, and inversely proportional to the square of the radius of the shell. The following relationship will be used as the scaling law for microscale hemispherical shell resonator gyroscope design.

$$f \propto \frac{h}{R^2} \quad (2.20)$$

2.1.5 FEA Simulation

Finite Element Analysis (FEA) is done by COMSOL Multiphysics software. Quadrilateral elements are used for the major body of the structure, and tetrahedral elements are used at the bottom around the support structure as figure 2.2 shows. A

polysilicon hemispherical shell with radius $600\ \mu\text{m}$ and thickness $1\ \mu\text{m}$ is modeled. In order for the accuracy of simulation, total of 31,000 elements are generated with the need of 9 GB of RAM.

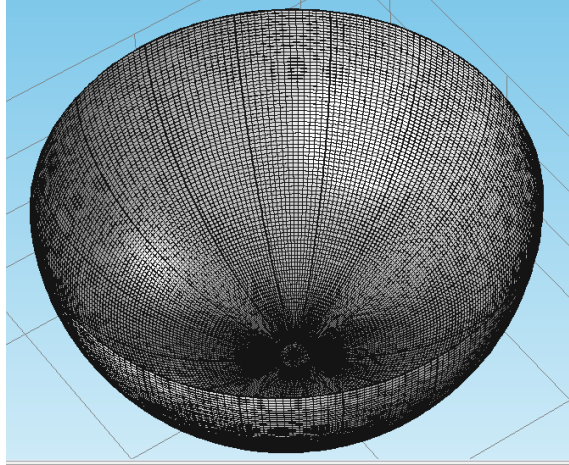


Figure 2.2: Axial symmetric meshing in COMSOL Multiphysics

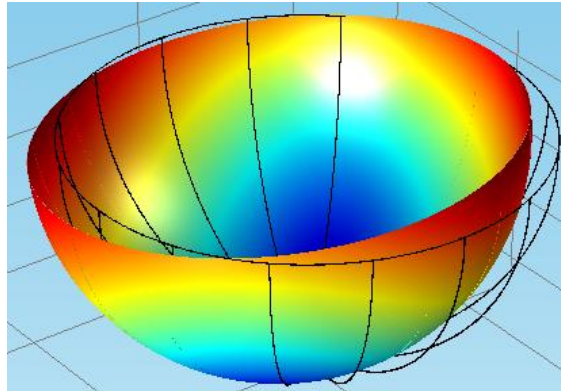


Figure 2.3: Rocking mode at 14.33 kHz for a polysilicon hemispherical shell

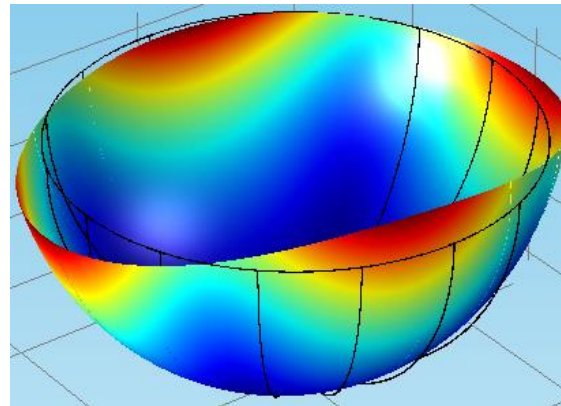


Figure 2.4: $m=2$ mode at 4.85 kHz for a polysilicon hemispherical shell

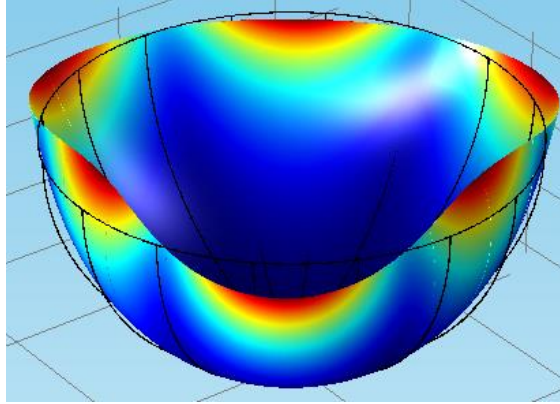


Figure 2.5: m=3 mode at 13.35 kHz for a polysilicon hemispherical shell

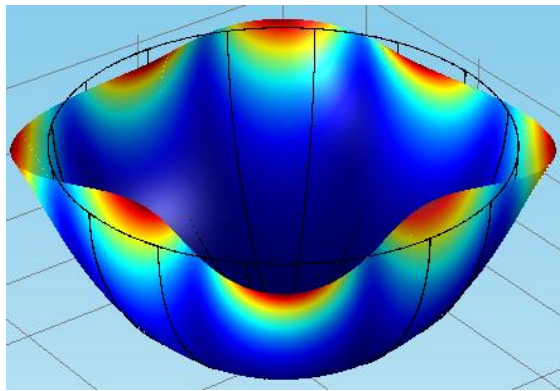


Figure 2.6: m=4 mode at 25.64 kHz for a polysilicon hemispherical shell

Table 2.1: COMSOL eigenfrequency study of a polysilicon hemispherical shell

	Mode #1 (Hz)	Mode #2 (Hz)	Mismatch (Hz)
Rocking	14324.9591	14325.2500	0.2909
m=2	4852.0189	4852.0965	0.0776
m=3	13352.2318	13352.2327	0.0009
m=4	25641.1334	25641.1338	0.0004

Figure 2.3 to Figure 2.6 illustrated the mode shape of the polysilicon hemispherical shell for rocking mode, m=2 mode, m=3 mode and m=4 mode respectively. Table 2.1 summarizes the simulated resonance frequency by COMSOL multiphysics eigenfrequency study. The numerical error by FEA analysis will caused a finite frequency mismatch

between two degenerate modes. This frequency mismatch is calculated, proving a symmetric meshing algorithm. As can be seen in Table 2.1, higher order modes are less affected by the meshing asymmetry. The μ HRG described in this dissertation works at its $m=2$ mode. However, studying and understanding its higher order mode helps improve the performance.

2.2 Energy Dissipation

Quality factor (Q) of the micro-hemispherical shell resonator (μ HSR) is an important performance for the gyroscope. Higher quality factor always means higher sensitivity and lower noise. In resonating devices, Q is defined in terms of the energy stored in the resonator to the energy supplied by a generator, per cycle, to keep signal amplitude constant at the resonance frequency as equation (2.21) shows.

$$Q = 2\pi \times \frac{\text{Energy Stored}}{\text{Energy dissipated per cycle}} \quad (2.21)$$

For high values of Q, the following definition is also mathematically accurate [41]

$$Q = \frac{f}{BW} \quad (2.22)$$

Where, f is the resonance frequency and BW is the 3dB bandwidth of the resonance peak.

In mechanical systems, the stored energy is the sum of the potential and kinetic energies at some point of time, and the dissipated energy is always related to any work done by various physical phenomenon. In this section, different energy dissipation mechanisms such as thermoelastic damping, squeezed film damping, support loss, are studied. The total Q can be calculated by equation (2.23) once all the damping mechanism is fully understood.

$$\frac{1}{Q} = \frac{1}{Q_{TED}} + \frac{1}{Q_{Air}} + \frac{1}{Q_{support}} + \dots \quad (2.23)$$

2.2.1 Thermoelastic Damping (TED)

TED results from the coupling of the vibrational domain into the thermal domain and the subsequent dissipation of the thermal energy via irreversible heat flow through thermal gradients. To quantify this dissipation, one should solve the governing equations of thermoelasticity distributed over the structure of interest. Hence, for every point in the structure, one should solve [42-44] (subject to appropriate boundary conditions)

$$\rho \frac{\partial^2 u_i}{\partial t^2} - \frac{E}{2(1+\mu)(1-2\mu)} \frac{\partial^2 u_j}{\partial x_i \partial x_j} - \frac{E}{2(1+\mu)} \frac{\partial^2 u_i}{\partial x_j^2} = - \frac{\alpha E}{(1-2\mu)} \frac{\partial T}{\partial x_i} \quad (2.24)$$

$$\rho C_P \frac{\partial T}{\partial t} - \kappa \frac{\partial^2 T}{\partial x_i^2} = - \frac{\alpha E}{3(1-2\mu)} T_0 \frac{\partial \varepsilon_{ii}}{\partial t} \quad (2.25)$$

where u_i represents the displacement in the x_i^{th} direction, t represents time, and σ_{ij} and ε_{ij} are the linearized stress and strain components. T_0 is the ambient temperature of the device and T is the localized temperature offset from ambient. The remaining material properties are the linear coefficient of thermal expansion α , the specific heat C_P , and the thermal conductivity κ .

Ultimately, the Q determined by TED of a single relaxation mechanism of the structure can be well approximated by [44, 45]

$$Q_{TED}^{-1} = \Delta_E \frac{\omega \tau_{th}}{1 + (\omega \tau_{th})^2} \quad (2.26)$$

where Δ_E is the relaxation strength of the Young's Modulus defined by

$$\Delta_E = \frac{E \alpha^2 T_0}{\rho C_P} \quad (2.27)$$

and the thermal relaxation time constant τ_{th} is given by

$$\tau_{th} = \frac{\rho C_P d^2}{\pi^2 \kappa} \quad (2.28)$$

In the above, ω is the driven angular frequency and d is the thermal path length defined by the temperature distribution over the structure, and is a function of the geometry.

Zener has demonstrated [46] that the geometry-dependent parameter of minimum Q_{TED} that separates the adiabatic and isothermal modes of operation of a device. In the adiabatic region, the frequency of operation is high enough to prevent significant thermal diffusion, thereby reducing the irreversible thermodynamic loss. In the isothermal region, large thermal gradients do not have a chance to develop. When the resonator is driven in the m^{th} inextensional mode, $\omega = \omega_m$ is assumed to be low enough that the resonator is operated in the isothermal regime where $\omega_m \tau_{th} \ll 1$, and equation (2.26) reduces to

$$Q_{TED}^{-1} = \Delta_E \omega_m \tau_{th} \quad (2.28)$$

Alternatively, traditional macroscale hemispherical shell resonators typically have a greater h/R ratio, resulting in high modal stiffness. It is usually safe to assume that they operate in the adiabatic TED regime, for which

$$Q_{TED}^{-1} = \frac{\Delta_E}{\omega_m \tau_{th}} \quad (2.29)$$

COMSOL Multiphysics was used as the finite element software to solve the fully-coupled system of equations define in equation (2.24) and (2.25). COMSOL is a powerful finite element suite and allows nearly arbitrary coupling of different built-in physics domain. Therefore, COMSOL is selected as the platform for all the simulations run in this dissertation. For TED simulation, the Solid Mechanics module of COMSOL was used with thermal expansion enabled to account for the left and right hand sides of equation (2.24). The Heat Transfer in Solids module was used to account for the second term on the left of equation (2.25), and the first term on the left and the right hand side were co-implemented as a body heat source. The simulation was run at PACE serve at Georgia Tech with 24 cores and 100 GB physical memory. Figure (2.7) shows the temperature distribution of a μHSR working at its $m=2$ resonance mode. It clearly demonstrates a rapid decay from the rim of the shell to its bottom, with an opposite polarity at its anti-nodes with opposite stress and room temperature at nodes.

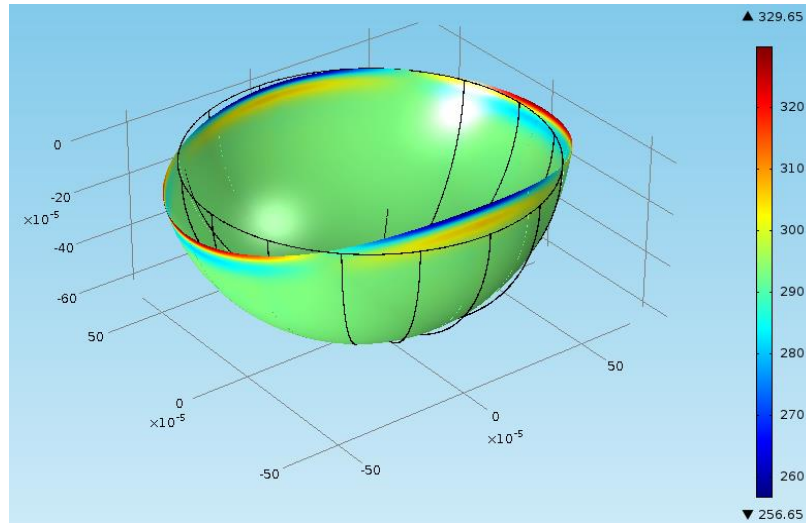


Figure 2.7: Temperature distribution of a μ HSR at its $m=2$ mode

The μ HSR is going to be operated below 20 kHz for longer decay time. At these frequencies, energy losses due to thermoelastic damping can be expected to be a significant factor in determining the overall resonator Q . Therefore, extensive thermoelastic damping simulations of hemispherical shell structures of varying dimensions and materials to identify some potentially promising structures. Table 2.2 lists the important material properties of various semiconductor and metal materials. Selected results of some of those simulations are shown in Table 2.3. The decay time values are calculated under the assumption that $Q = Q_{TED}$. Of course, it can be expected that the overall resonator Q will be less than Q_{TED} because of other energy loss mechanisms, which will be discussed in the following section. Nevertheless, the goals will be to minimize other loss mechanisms and get as close to Q_{TED} as possible. As such, the simulation results are helpful in selecting materials that are more likely than others to have a better performance.

The data in the table confirms that Q_{TED} is affected strongly by the value of the thermal expansion coefficient of the material. In particular, it can be seen that SiO_2 easily outperforms all the other materials listed in the table from the point of view of Q_{TED} . Of course, the overall Q of SiO_2 resonators could be significantly lower, because of the effect of the additional processing steps (conductive coating) needed to make it electrically

conductive. The other materials listed in the table are all conductors or semiconductors that can be doped, but their thermoelastic damping is low enough for high Q_{TED} . As it can be seen, polysilicon shells with thickness of $1\mu\text{m}$ will yield sufficiently high Q_{TED} values and as such would be one of the best candidates for the μHRG from a standpoint of ease of fabrication.

Table 2.2: Material properties

Material	Young's Modulus [GPa]	CTE [ppm/C]	Thermal Conductivity [W/(mK)]	Mass Density [kg/m ³]
PolySi	160	2.6	34	2330
SiO ₂	70	0.5	1.4	2200
SiN	250	2.3	20	3100
Al	70	23.1	237	2700
Au	70	14.2	317	19300
Cu	120	16.5	401	8960
Pt	168	8.8	71.6	21450

Table 2.3: Selected TED simulation run in COMSOL

Material	Diameter [μm]	Thickness [μm]	Frequency [Hz]	Q_{TED}	Decay Time [s]
PolySi	1240	1	4803.2	4.33E+06	286.8
SiO ₂	1240	1.5	4847.5	1.89E+08	12434.0
SiN	1240	1	5175.4	3.01E+06	184.8
Al	1240	1.5	4089.5	4.66E+05	36.3
Au	620	1	4270.8	3.98E+06	296.9
Cu	1240	2	3901.7	5.88E+05	47.9
Pt	716	1	4754.7	9.66E+05	64.7

2.2.2 Squeezed Film Damping

If a structure is oscillating near a second surface, the damping effect of the surround air will be increased due to the squeeze film action of the gas between the surfaces [47]. The squeeze film damping will be more important than the drag force damping of air if the thickness of the gas film is smaller than one-third of the width of the structure [48]. Therefore, for most MEMS resonance devices which are targeting high quality factor,

squeeze film damping is an important energy dissipation mechanism due to the narrow capacitive gap for driving and sensing the device.

In MEMS devices, the behavior of squeeze film is governed by viscous effect only, while ignoring its inertial effect. Therefore, the reduced Reynolds equation is used [49, 50]:

$$\frac{\partial}{\partial x} \left(\rho \frac{h^3}{\mu} \frac{\partial P}{\partial x} \right) + \frac{\partial}{\partial y} \left(\rho \frac{h^3}{\mu} \frac{\partial P}{\partial y} \right) = 12 \frac{\partial(h\rho)}{\partial t} \quad (2.30)$$

Where P is the pressure in the film, ρ is the density, μ is the coefficient of viscosity of the fluid, h is the thickness of the film.

Furthermore, for MEMS devices, the temperature variation is usually negligible due to small dimensions. Under the isothermal condition, gas density is directly proportional to its pressure. Thus, equation (2.30) can be reduced to:

$$\frac{\partial}{\partial x} \left(\frac{Ph^3}{\mu} \frac{\partial P}{\partial x} \right) + \frac{\partial}{\partial y} \left(\frac{Ph^3}{\mu} \frac{\partial P}{\partial y} \right) = 12 \frac{\partial(hP)}{\partial t} \quad (2.31)$$

In the case of capacitive parallel plate, h and μ is not a function of position. Equation (2.31) can be simplified as

$$\frac{\partial^2}{\partial x^2} P^2 + \frac{\partial^2}{\partial y^2} P^2 = \frac{24\mu}{h^3} \frac{\partial(hP)}{\partial t} \quad (2.32)$$

The squeeze film pressure consists of two main components: the viscous damping force and the elastic damping force. The viscous damping force causes the viscous flow of air when the air is squeezed out or sucked into the plate region; the elastic damping force causes the compression of the air film.

In the case of a low frequency resonator, the gas film is not compressed appreciably, then the viscous damping force dominates. The viscous force is directly proportional to the speed of the plate. In the case of high frequency resonator, the gas film is compressed but fails to escape, then the elastic force dominates. The elastic force is directly proportional to the displacement of the plate.

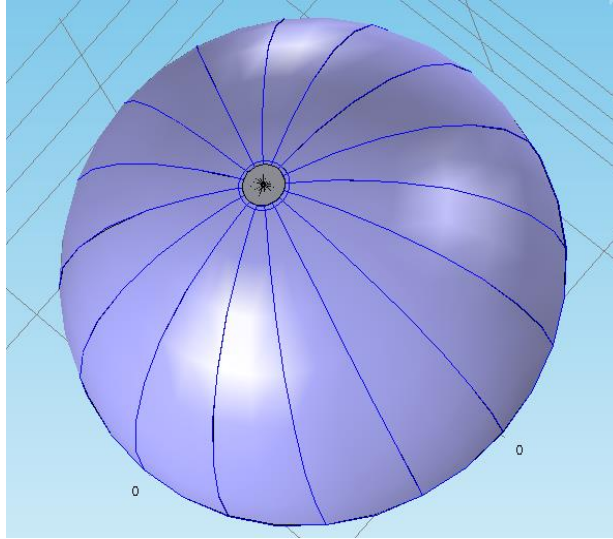


Figure 2.8: Illustration of COMSOL squeeze film damping simulation

The microscale hemispherical resonating gyroscope presented in this dissertation is a low frequency device (< 20 kHz). Thus, squeeze film damping will play an important role on the mechanical quality factor. Although it can be eliminated by testing the device in a vacuum chamber with around $10 \mu\text{Torr}$ vacuum level, the study will be instructive eventually when performing vacuum packaging of these devices. Current vacuum packaging technologies are able to seal MEMS device in $100 \mu\text{Torr}$ to 1 mTorr with the application of gettering material [51]. In proper designing the capacitive gap size, squeeze film damping should be minimized at 1 mTorr vacuum level.

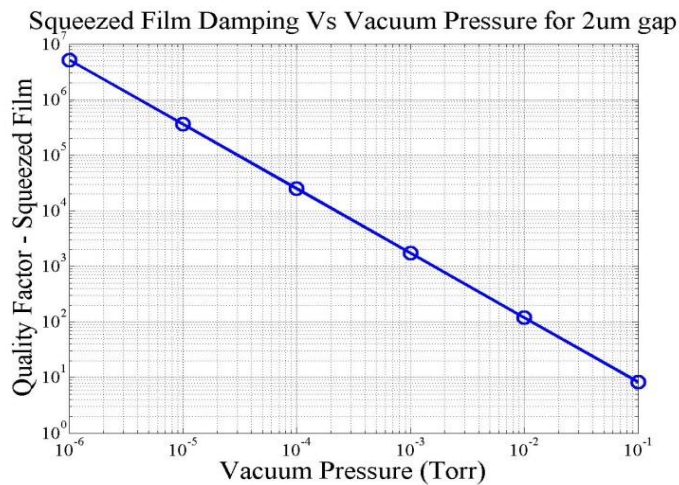


Figure 2.9: $Q_{\text{squeez_film}}$ as a function of vacuum pressure for a $2\mu\text{m}$ gap device

Finite element model is built in COMSOL Multiphysics, using the module of solid mechanics with thin film damping option on. Figure 2.8 illustrates the model in COMSOL. Surfaces in purple color have thin film damping set up for simulation. The simulation is run at a 24 core computer node at Georgia Tech PACE server with the usage of 64 GB physical memory.

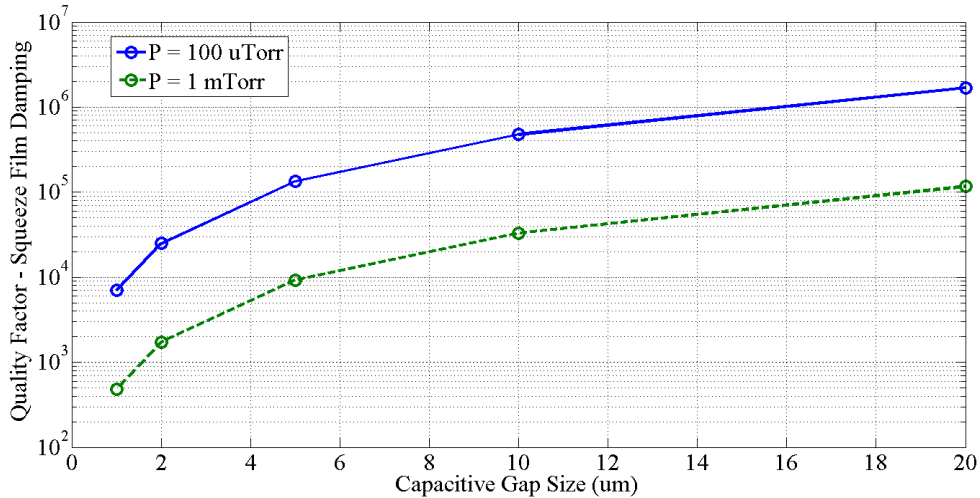


Figure 2.10: $Q_{\text{squeez_film}}$ as a function of capacitive gap size

Figure 2.9 shows the simulation results for a device with 2 μm capacitive gap at different vacuum pressure from 1 μTorr to 100 mTorr. It clearly shows a linear relationship between quality factor and vacuum pressure, with Q of 5,200,000 at 1 μTorr and Q of 8.3 at 100 mTorr. Another study on how gap size will affect the quality factor is also performed at 100 μTorr and 1 mTorr, around which is the vacuum pressure of a packaged device. With a gap size of a few microns, it is impossible to reach very high Q. In order to reach Q of 1 million, at least 20 μm gap size is needed at 100 μTorr vacuum pressure. This simulation result is challenging the fabrication process flow significantly. Traditional microfabrication technique create the capacitive gap by a sacrificial layer, whose thickness defines the gap size. In the meantime, 20 μm film could be too thick for any types of sacrificial layer, if the deposition requires high uniformity and smoothness. Therefore, a

new process flow which can create scalable capacitive gaps is developed, and will be introduced in Chapter 6.

2.2.3 Support Loss

Support loss, also known as clamping loss or anchor loss, is the vibration energy of a resonator dissipated by transmission through its support. During its flexural vibration, the hemispherical shell resonator will have both vibrating shear force and moment on its support structure. These shear force and moment will be acting as excitation sources, thus will excite elastic waves propagating into the support. This mechanism causes some energy dissipated through the support structure into substrate.

Close form solution of support loss of some particular structures such as beam [52], circular disk [53] has been reported. A Perfectly Matched Layers (PML) method was also developed based on finite element method [54]. The PML absorbs incoming waves over a wide frequency range for any non-zero angle of incidence. A PML model consists of a sub-domain where the actual equation of interest is dealt with explicitly, and a sub-domain that produces the desired effect of a far-field radiation boundary condition.

Because of the way the perfectly match medium (PMM) is defined, the size of the PMM needs to be on same order of the wavelength. This actually creates a difficulty in simulating low frequency resonant devices by PML method. After calculating the speed of sound in silicon, one can easily find the wavelength of a 5 kHz resonator is about 2 meters. It is impossible to model a structure with 2 meter in size, while having another high aspect ratio hemispherical shell structure. Therefore, the simulation is done at above 350 kHz with increased shell thickness in order to show the trend of quality factor as a function of support design.

A hemispherical shell with diameter 1000 μm and thickness 50 μm with PML region 2 cm is built in COMSOL as figure 2.11 shows. Since frequency mismatch is not a concern of this simulation, only one eighth of the shell with symmetric boundary condition

is modeled in order to reduce the number of elements. The inset is the zoomed-in view of the resonating shell structure. It can be clearly seen that the PML region is much larger than the size of the resonating structure¹.

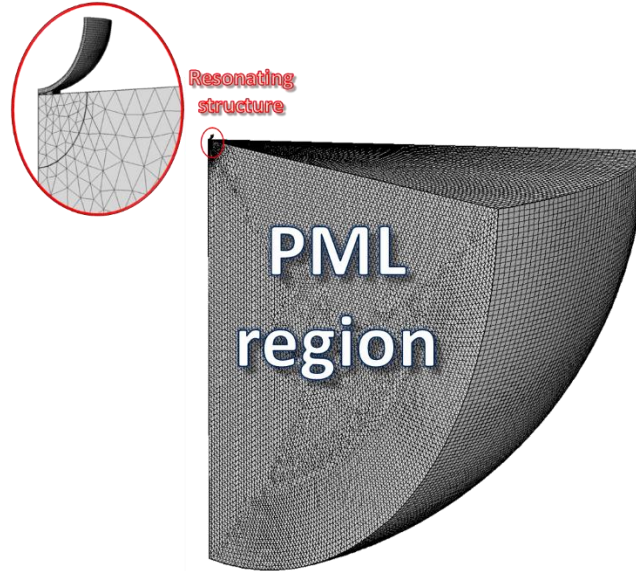


Figure 2.11: Illustration of PML region and resonating structure in support loss simulation

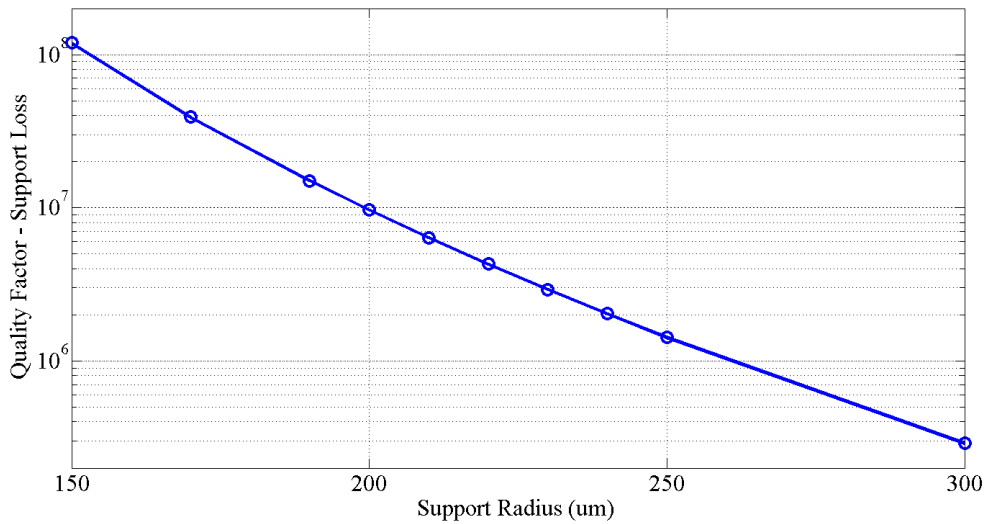


Figure 2.12: Q_{support} Vs. support radius

¹ Courtesy of Dr. Vahid Tavassoli on PML simulation

Figure 2.12 shows the trend of quality factor as a function of support radius. Quality factor reduces from 100,000,000 to 200,000 as the support radius increases from 150 μm to 300 μm . There is a clear trend that smaller support will give higher quality factor. In order to further isolate acoustic energy and the substrate which is an energy sink, the structure can be levitated by a long supporting stem. Figure 2.13 shows the trend of quality factor as a function of support stem length. By increasing the stem length from 20 μm to 200 μm , the quality factor increases almost an order of magnitude.

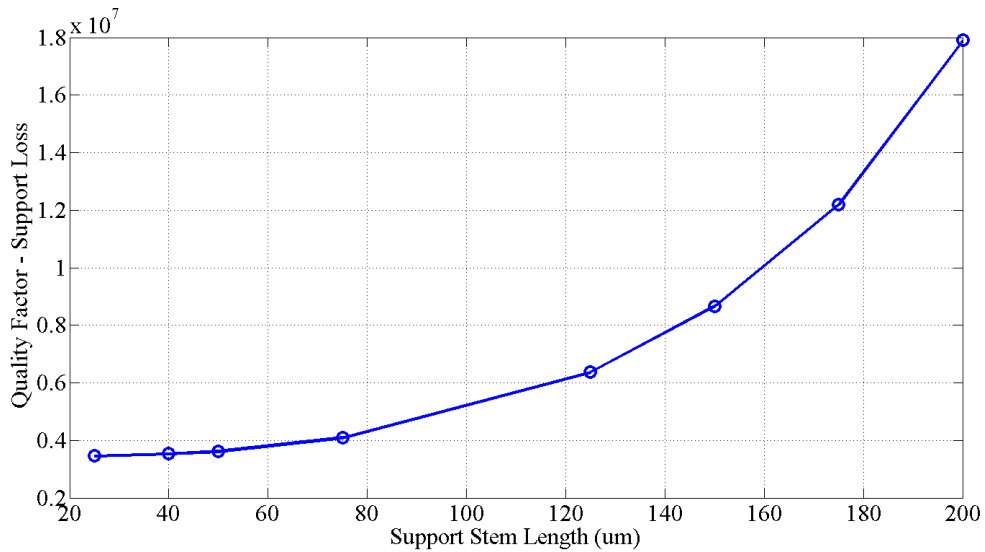


Figure 2.13: Q_{support} Vs. support stem length

2.2.4 Surface Loss

For MEMS shell structures with ultra-high aspect ratio, the surface-to-volume ratio increases dramatically when shell thickness scales down. Then surface loss starts to play an important role. The surface loss is mostly caused by surface stress, which could significantly be modified by adsorbates on the surface or surface defects. When adsorbates exist on the surface, the charge transfers between the surface and the adsorbates, therefore the Coulomb repulsion of the dipole moments associated with the adsorbate atom orbits at a close distance would modify the surface stress, and lead to surface loss [55]. It has been

derived theoretically for a sub-micron thick cantilever, the Q_{surface} is directly proportional to the film thickness [55, 56] .

However, due to the lack of fully understanding of this type of energy loss mechanism, there is no report on modeling surface loss for estimation of Q_{surface} . Researchers studied experimentally the effect of thermal treatment on surface loss of silicon cantilever [57, 58], and demonstrated that annealing the devices at high temperature (600 – 1000 °C) will increase the quality factor by a factor of 2 to 4. By x-ray photoelectron spectroscopy (XPS) study, significant amount of oxygen and carbon were detected, showing the necessary to investigate the effects of both oxygen and carbon adsorptions on the structure. By flash heating the devices, native O_2 as well as native oxide were removed and a monotonic dependence of Q factor on O/Si ratio for submicron thick cantilevers can be shown. This technique requires elimination of ambient air exposure after thermal treatment, otherwise oxygen and carbon will re-adsorb on the structure surface. In order for this, devices need to be vacuum packaged right after thermal treatment without breaking the vacuum. Proper equipment needs to be developed accordingly.

2.3 Structural Anisotropy

The micro-hemispherical shell resonating gyroscope (μ HRG) presented in this dissertation is the second type MEMS gyroscope that relies on the energy transfer between two degenerate mode of vibration. This type of MEMS gyroscope consists an axial symmetric structure with drive and sense electrodes around. The way to quantify structural anisotropy is to measure the frequency mismatch of two degenerate modes. For example, without electrostatic tuning the polysilicon ring gyroscope has a mismatch of 63 Hz out of 28 kHz [28]; the bulk acoustic wave disc gyroscope has a mismatch of 300 Hz out of 5.9 MHz [34]. This frequency mismatch directly reflect the degree of symmetry of the structure, which is required by both rate mode [18] and rate integrating mode [59] gyroscope.

In general, the frequency mismatch of micro-hemispherical shell resonating gyroscope could be created from the isotropic etching of bulk silicon, structural material growth/deposition anisotropy, support structure misalignment and/or anisotropy. This section analyze these possible causes of frequency mismatch and instruct on designing the structure and process flow of the gyroscope.

2.3.1 Isotropic Molding

The hemispherical shape of μ HRG is defined by isotropic etching of bulk single crystal silicon as describe in [60], which will be discussed in detail in following chapters. In this section, the analysis of the effect of etching anisotropy on the frequency mismatch between degenerate modes is performed. Single crystal silicon has a diamond structure with face centered cubic (fcc) lattice as figure 2.14 shows. Each silicon atom has four nearest neighbors and the lattice constant is 5.431 angstroms. Typical commercial available single crystal silicon wafers have their cutting plane normal to direction (1,0,0) / (0,0,1) and direction (1,1,1), which are named 100 and 111 silicon wafer, respectively. If viewed perpendicular to (100) plane, the silicon structure is showing a four-fold symmetry (figure 2.15), and a six-fold symmetry (figure 2.16) while viewed perpendicular to (111) plane. Thus, 100 silicon wafer has four-fold symmetry and 111 silicon wafer has six-fold symmetry, with the most close-packed direction of (1,1,0).

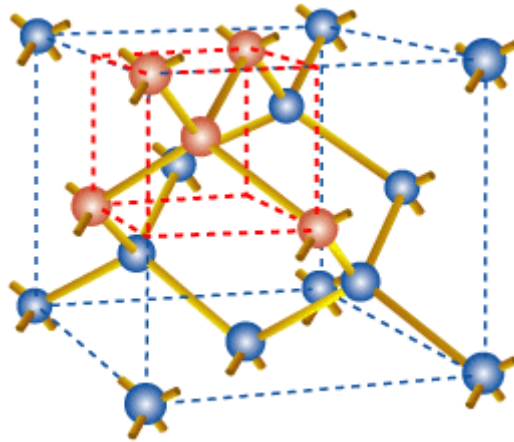


Figure 2.14: Unit cell of single crystal silicon

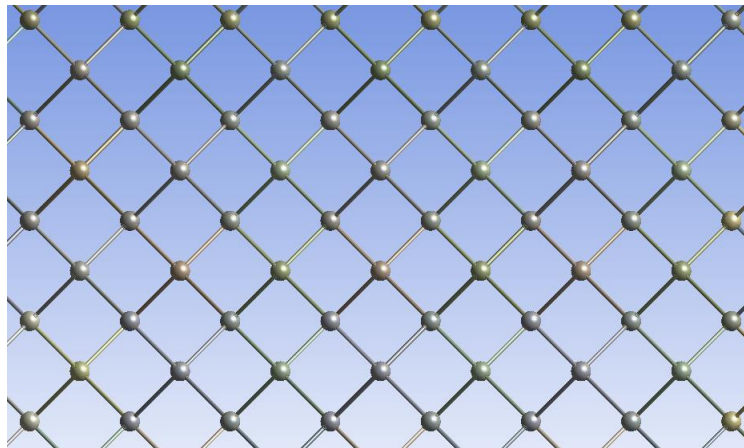


Figure 2.15: Silicon structure viewed from (1,0,0) direction

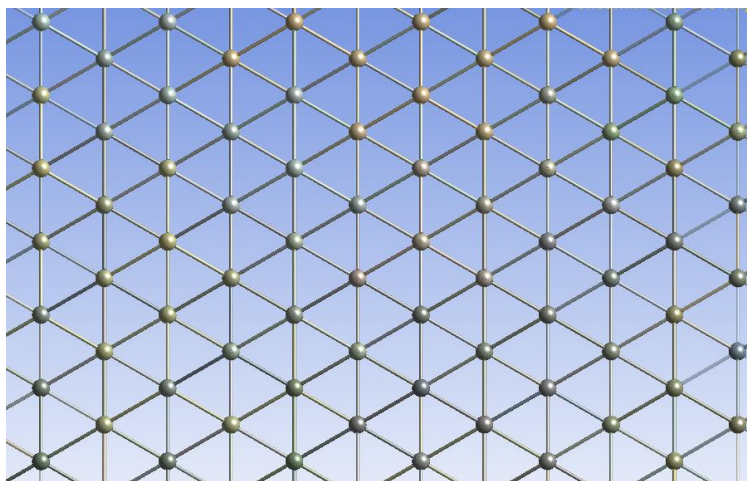


Figure 2.16: Silicon structure viewed from (1,1,1) direction

Due to this in-plane anisotropy of silicon wafer, isotropic etching of single crystal silicon has crystalline dependency. The most close-packed direction is showing the slowest etch rate because there is more atoms to be etched in this direction. To simulate this type of crystal dependent anisotropy, geometry model is built in COMSOL Multiphysics to imitate the shape shown in [61, 62]. For 100 silicon wafer, 1/8 of a hemi-ellipsoid shell is used to model the continuously varying shell radius. By other body operations such as mirroring and rotation, a full hemispherical shell with four-fold symmetry can be modeled. The degree of anisotropy can be tuned by changing the ratio between the maximum semi-principle axes and minimum semi-principle axes of the hemi-ellipsoid shell. The degree of anisotropy can then be defined as:

$$\text{anisotropy} = \frac{R_{max} - R_{min}}{R_{ave}} = \frac{dR}{R} \quad (2.33)$$

where R_{max} is the maximum radius at 45° , R_{min} is the minimum radius at 0° , and R_{ave} is the average radius.

Figure 2.17 demonstrates the geometry model of a hemispherical shell of four fold symmetry with anisotropy 2.38% (left) and 4.54% (right). Similarly, 1/12 of a hemi-ellipsoid shell can be used to model a hemispherical shell created out of 111 silicon wafer. Figure 2.18 demonstrates the geometry model of a hemispherical shell of six fold symmetry with anisotropy 1.18% (left) and 2.22% (right).

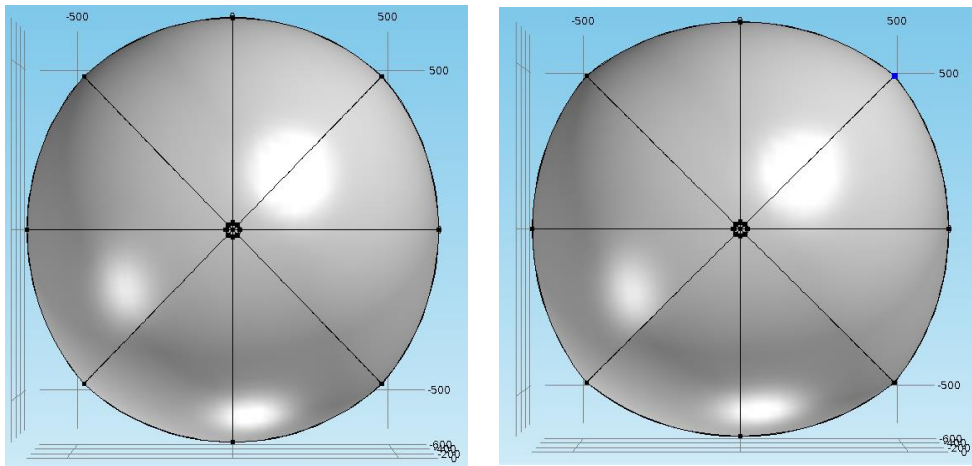


Figure 2.17: Hemispherical shell with four-fold symmetry

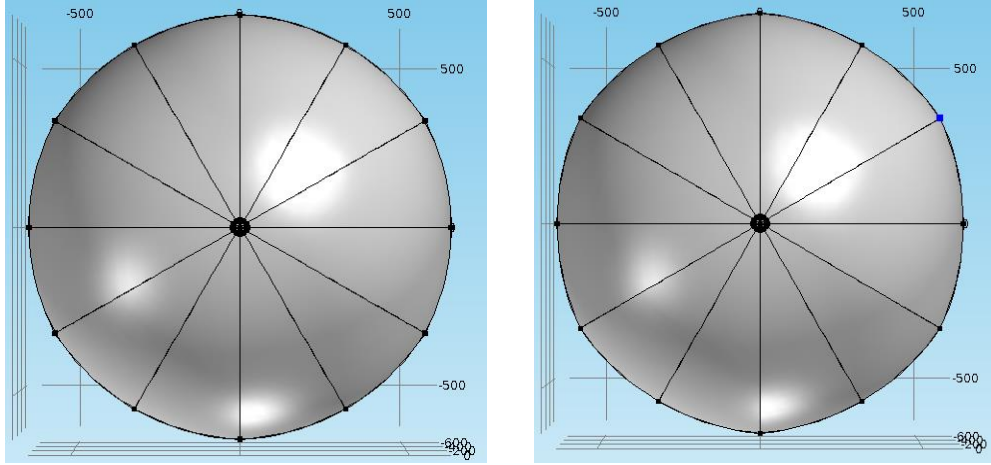


Figure 2.18: Hemispherical shell with six-fold symmetry

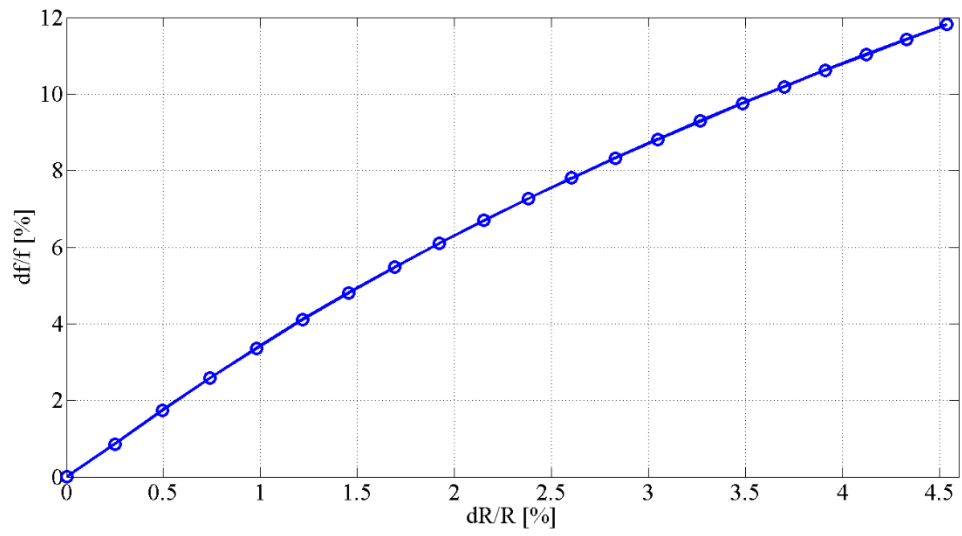


Figure 2.19: Simulated frequency mismatch for m=2 mode of 100 wafer

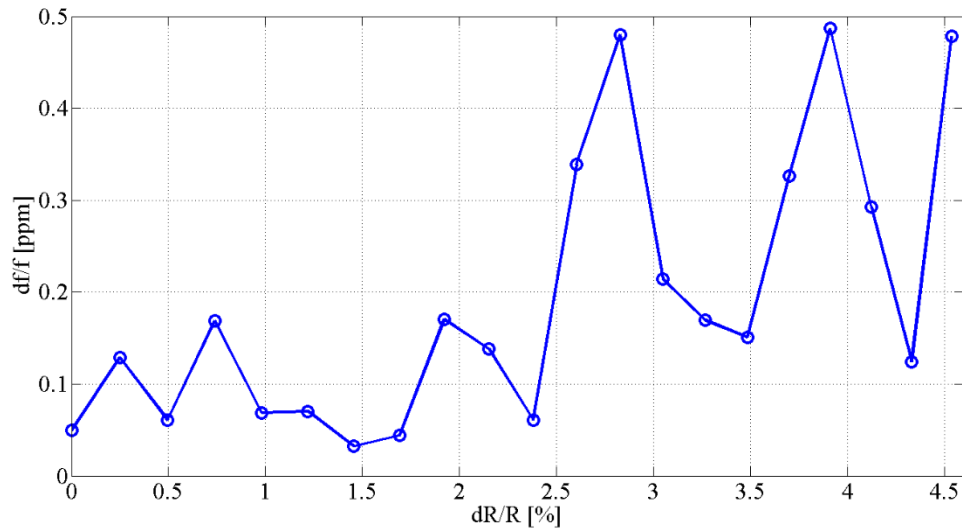


Figure 2.20: Simulated frequency mismatch for m=3 mode of 100 wafer

Eigen-frequency analysis was run for a polysilicon hemispherical shell with radius of 620 μm and thickness of 1 μm . Calculated frequency mismatch was scaled with the actual frequency to obtain the relative value. Figure 2.19 and figure 2.20 demonstrate the frequency mismatch of m=2 and m=3 mode for a hemispherical shell created out of 100 wafer, respectively. The frequency mismatch of m=2 is showing a nearly proportional trend with the anisotropy, while m=3 is showing no dependency on the anisotropy (<0.5 ppm can be considered as calculation error). Figure 2.21 and figure 2.22 demonstrate the frequency mismatch of m=2 and m=3 mode for a hemispherical shell created out of 111 wafer, respectively. The frequency mismatch of m=3 is showing a nearly proportional trend with the anisotropy, while m=2 is showing no dependency on the anisotropy (<50 ppm can be considered as calculation error).

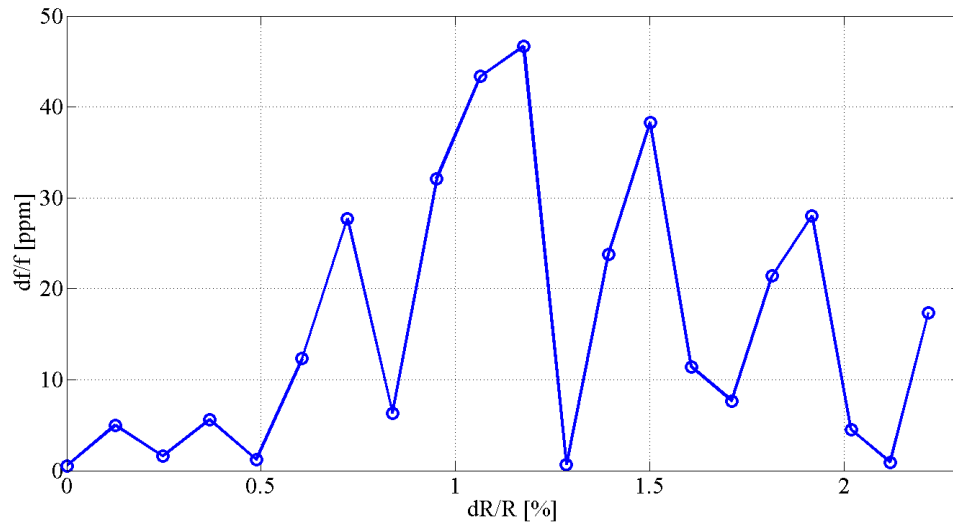


Figure 2.21: Simulated frequency mismatch for m=2 mode of 111 wafer

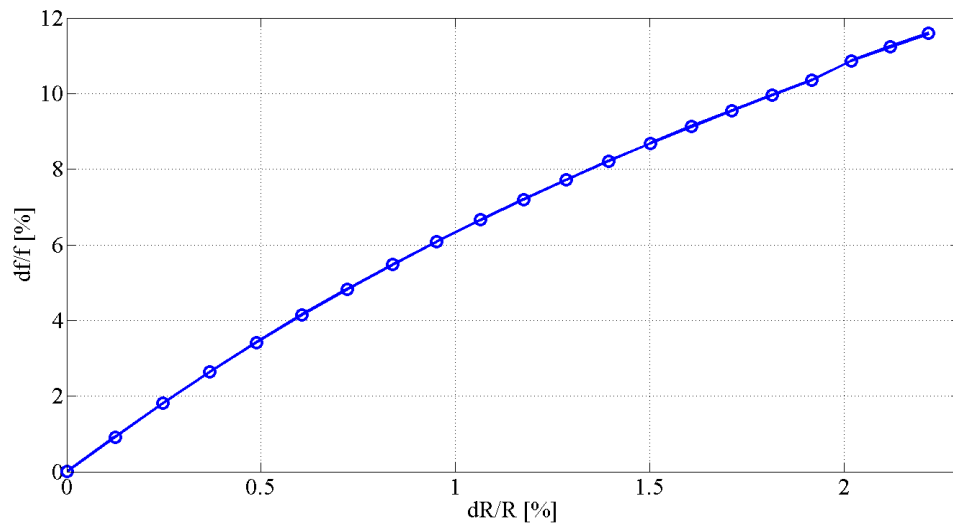


Figure 2.22: Simulated frequency mismatch for m=3 mode of 111 wafer

This set of simulation demonstrates the effect of the orientation of silicon wafer on the frequency mismatch between degenerate modes of m=2 and m=3 modes. The four-fold symmetry structure produced by 100 wafer will have a large frequency mismatch for m=2 mode but negligible frequency mismatch for m=3 mode. In the meantime, the six-fold symmetry structure produced by 111 wafer will have a large frequency mismatch for m=3 mode but negligible frequency mismatch for m=2 mode. These conclusion will be proved experimentally in the next chapter. Therefore, for a μ HRG that operated at m=2 mode, 111

silicon wafer is preferred; and for a μ HRG that operated at $m=3$ mode, 100 silicon wafer is preferred.

2.3.2 Structural Thickness Anisotropy

The growth rate of silicon dioxide on single crystal silicon has crystalline dependency. In this section, the effect of thickness anisotropy arising due to crystalline axis dependency in the wet thermal oxide growth on hemispherical single-crystal silicon molds is considered².

After defining the hemispherical silicon mold with an isotropic SF_6 etch as in [60], the entire set of silicon crystal planes will be exposed as figure 2.23 shows. Following the Deal-Grove model [63], the growth of thermal oxide in this mold can be accurately predicted for specific planes under varied processing conditions using empirically-derived parameters from growth on (001), (110), and (111) silicon wafers. Rate constants for these planes generally follow an Arrhenius temperature dependency allowing for prediction over a wide range of growth temperatures. However, little literature exists on oxide growth between these crystal planes, and that which does exist presents difficulties in application such as being limited to thin or native oxide layers [64, 65]. The growth conditions ultimately determine the structure of the μ HSR. To create large and balanced μ HSRs, oxide layers with a few μm of thickness must be employed to survive the XeF_2 release process [60].

² Courtesy of Dr. Logan Sorenson on structural anisotropy simulation

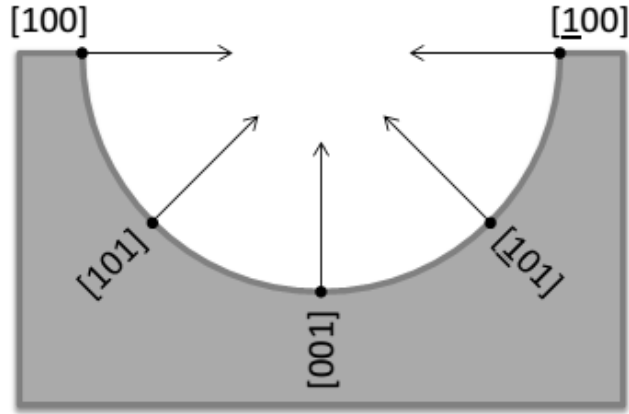


Figure 2.23: Schematic diagram depicting a few of the crystal plane normals exposed during thermal oxidation of silicon hemispherical mold

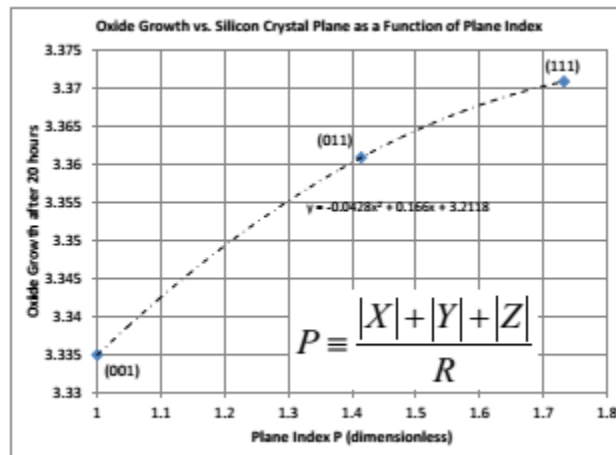


Figure 2.24: Interpolation of silicon dioxide growth rate vs. crystal plane index

Therefore, a new method of interpolation of the available growth data through a dimensionless crystal plane index P is proposed as shown in figure 2.24. Wet thermal silicon dioxide growth after 20 hours vs. crystal orientation is determined by Deal-Grove model and interpolated using a plane index P . A maximum of 36 nm (1.08%) difference was obtained between the 3 crystal planes. This approach can be generalized as knowledge of oxide growth kinetics is improved for uncommon orientations. Figure 2.25 was generated using the thickness interpolation of Figure 2.24. Figure 2.25 is the top view of the relative thickness map for 20 hours of wet thermal oxide growth at 1100°C in ideal hemispherical micromold on (001) and (111) single-crystal silicon wafers, respectively.

implement the mesh modification algorithm. Shell elements with a variable thickness parameter could be employed, but this complicates modeling of the shell-support stem interface. A more convenient option is mapping the oxide thickness variations according to figure 2.25 onto the Young's modulus by deriving the resulting effect on the modal frequencies while maintaining a constant geometric thickness of the shell.

Starting from equation (2.17), it can be shown that at an arbitrary point on the midsurface of the shell, the contribution to change in the overall frequency of the shell from a small thickness perturbation ($\Delta h \ll h$) at that point is:

$$\frac{\Delta\omega_m}{\omega_m} = \frac{\Delta h(\varphi, \theta)}{h} \quad (2.34)$$

It can also be shown that there is a similar contribution due to a Young's modulus perturbation with an additional factor of 1/2:

$$\frac{\Delta\omega_m}{\omega_m} = \frac{1}{2} \frac{\Delta E(\varphi, \theta)}{E} \quad (2.35)$$

Thus, there is an equivalency between small perturbations in thickness and Young's modulus over the area of the shell, which can be exploited to study the impact of thickness modulations on the frequency splits without impacting the geometry or mesh of the resonator. This is achieved by entering the following expression in place of the normal Young's modulus of the material in the finite element software:

$$E' = E + \Delta E(\varphi, \theta) = E \left(1 + 2 \frac{\Delta h(\varphi, \theta)}{h} \right) \quad (2.36)$$

It is interesting to note that small radial deviations from the ideal geometry can also be accounted for in a manner similar to (2.36), but with a factor of -4 instead of 2. Further, any perturbations to the other variables in (2.17) can be accounted for, or they may be used as an alternative to modulate the Young's modulus, providing a flexible and convenient method to take into account small perturbations to the parameters of the structure over the area of the shell.

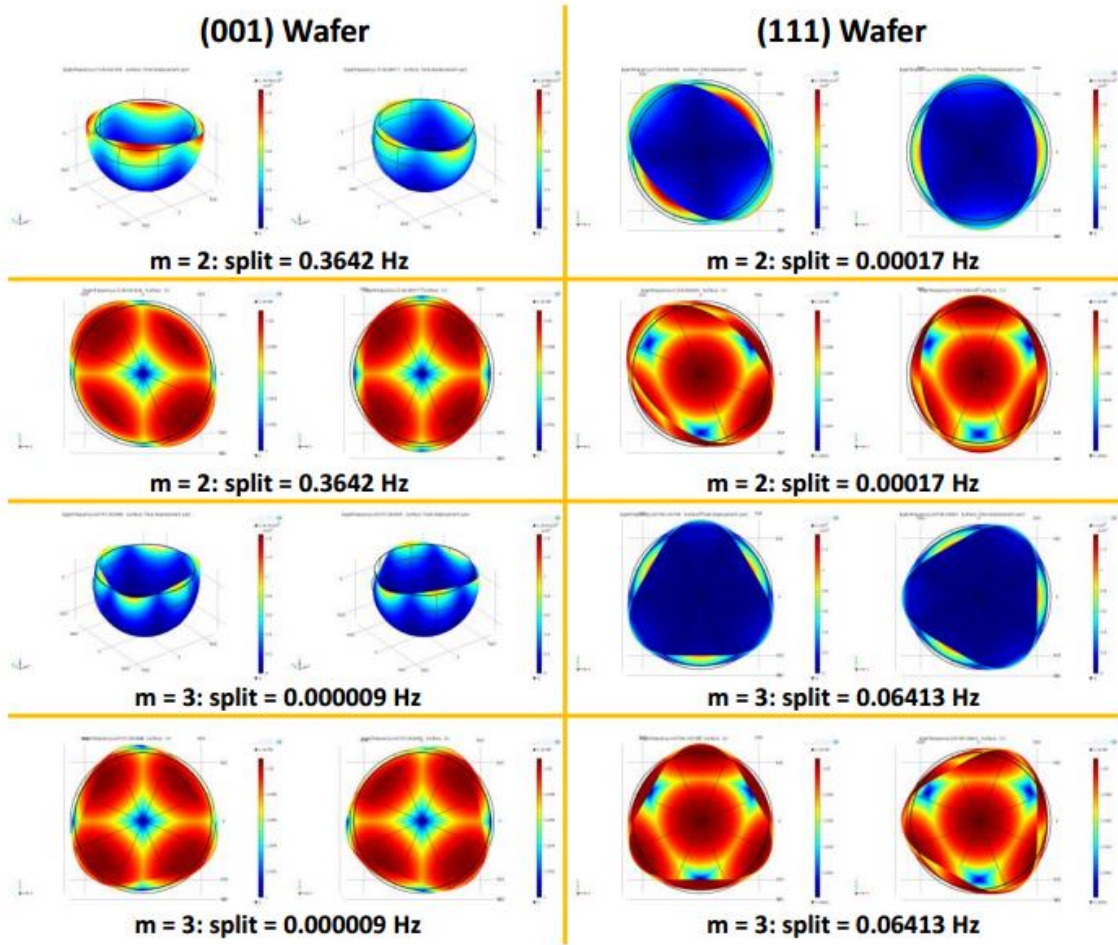


Figure 2.26: Simulated frequency split on (001) and (111) type substrates

COMSOL Multiphysics finite element software was chosen as the simulation platform due to its ease in implementing spatially-dependent material parameters by user-defined functions. Figure 2.26 shows the result of performing modal analysis on the structure for different assumptions of the initial substrate orientation. These simulations were controlled against a perfectly isotropic structure. A mesh convergence study was performed until the degenerate modes converged within 1 mHz. The thickness was then modulated according to Figure 2.24. For (001) wafers, the $m=3$ mode shows intrinsically 0 Hz frequency split (within numerical precision) and the $m=2$ mode shows 0.36 Hz split, while this situation reverses for (111) wafers, impacting the choice of starting substrate to achieve frequency-matched oxide shell resonators. Closer inspection reveals that the nearly-zero $m=2$ split in the latter case is not intrinsically 0 Hz but instead results as a

consequence of the nearly circular thickness pattern at the bottom of the hemisphere where stiffness contributions are most critical. These frequency splits are a direct consequence of the symmetry of the thickness anisotropy imparted by the underlying wafers, and shows that mitigation is possible by appropriate choice of the operating mode to eliminate frequency split along the two principle axes of elasticity.

2.3.3 Support Structure Anisotropy

The free-standing hemispherical shell structure of a μ HRG is usually released by isotropic XeF_2 vapor etching of bulk silicon [60] and followed by HF etching of sacrificial silicon dioxide layer [66] for some cases. The size and shape of the support structure is fully dependent on the timing and the nature of the etchant. Thus, there could be anisotropy on the shape of the support structure mainly due to 1) anisotropy transferred from the hemispherical mold; 2) etching anisotropy from the crystalline dependency. In the following chapter, it will be demonstrated that for a 100 substrate, a square-shaped support will be formed [60]. While for a 111 substrate, a triangle-shaped support will be formed [67]. In this section, the effect of the anisotropy of support structure on frequency mismatch between degenerate modes will be discussed.

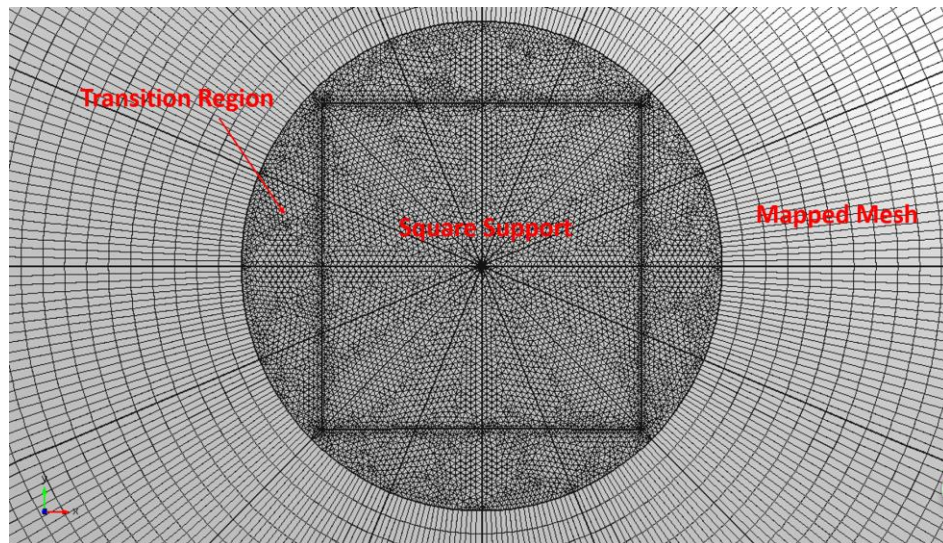


Figure 2.27: Mesh used to simulate a square support

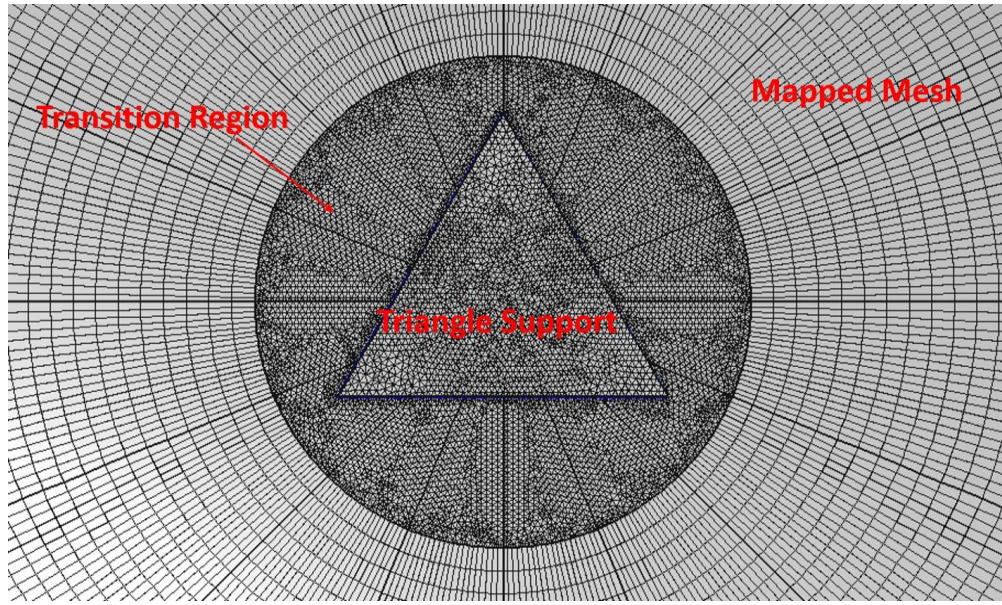


Figure 2.28: Mesh used to simulate a triangle support

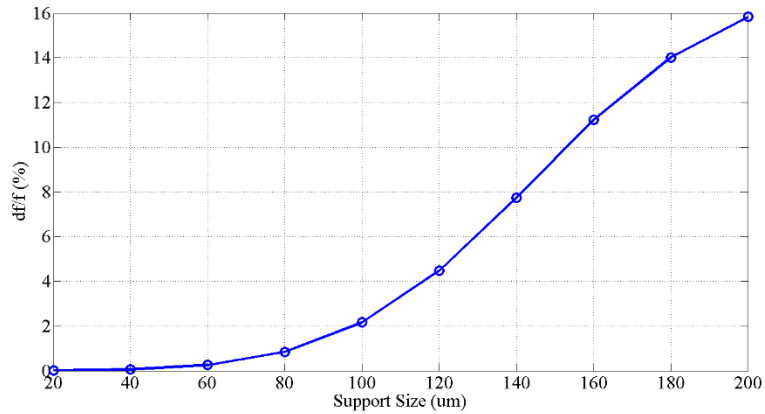


Figure 2.29: Simulated relative frequency mismatch between m=2 degenerate modes with square support Vs. support size

Figure 2.27 and figure 2.28 show the geometric model and mesh created in COMSOL in order to simulate the effect of square support and triangle support on frequency mismatch respectively. Fully symmetric mapped mesh is used for the hemispherical shell, and free tetrahedral mesh is used for the support structure with a transition region between them. Figure 2.29 – figure 2.32 show the simulation results on frequency mismatch of m=2 and m=3 mode of square support and triangle support respectively. As we can see, square support has a large impact on m=2 mode, while has nearly no impact on m=3 mode. At the same time, triangle support has no impact on m=2

mode, while has very small impact on m=3 mode. Thus, 111 silicon substrate will give the best symmetry for m=2 mode while 100 silicon substrate will give the best symmetry for m=2 mode.

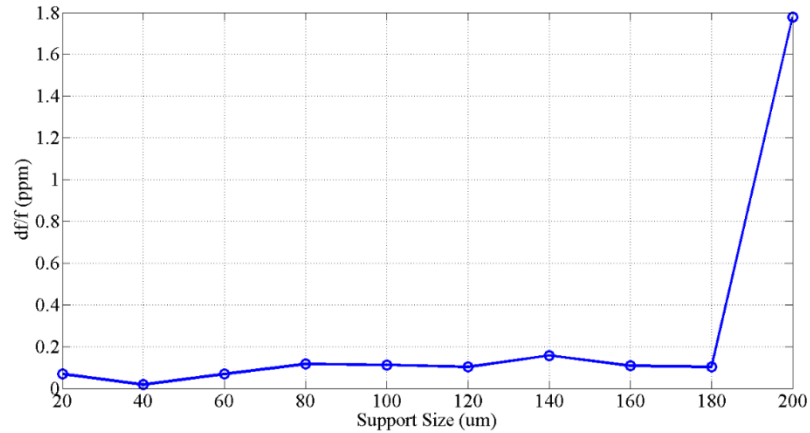


Figure 2.30: Simulated relative frequency mismatch between m=3 degenerate modes with square support Vs. support size

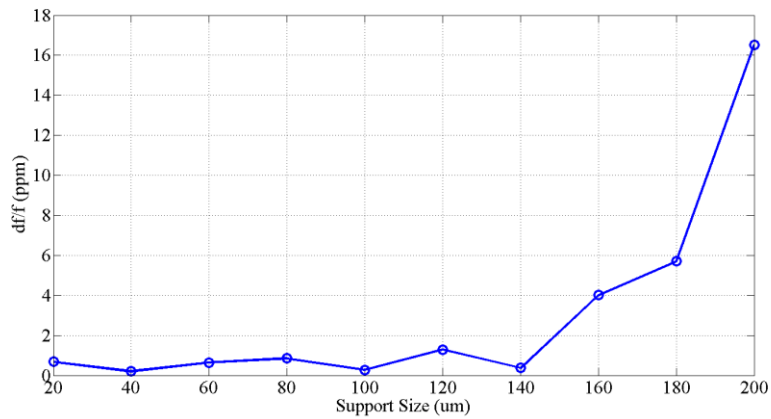


Figure 2.31: Relative frequency mismatch between m=2 degenerate modes with triangle support Vs. support size

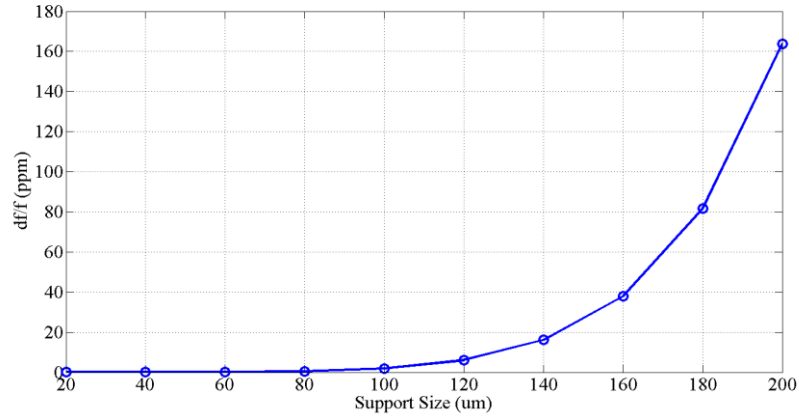


Figure 2.32: Relative frequency mismatch between $m=3$ degenerate modes with triangle support Vs. support size

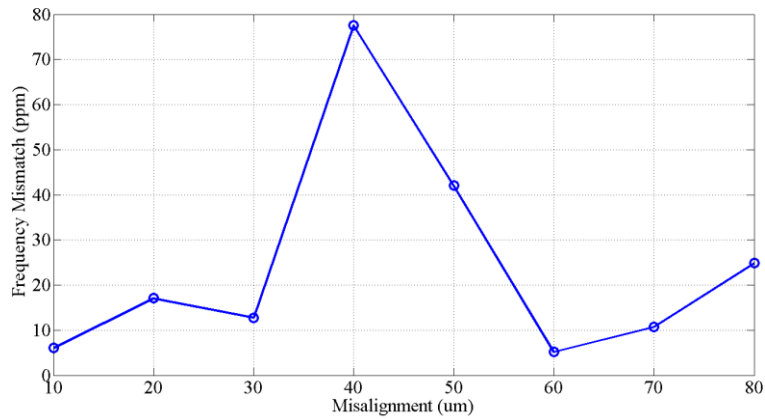


Figure 2.33: Relative frequency mismatch between $m=2$ degenerate modes Vs. support misalignment

Another type of anisotropy of the support of hemispherical shell is the misalignment between the shell structure and the support structure, because they are defined in separate lithography step. Usually, a front side alignment step could result in misalignment up to $5\ \mu\text{m}$, while a backside alignment step could result in misalignment up to $20\ \mu\text{m}$. Simulation is run for a circular support with radius of $200\ \mu\text{m}$ and misalignment from $10\ \mu\text{m}$ to $80\ \mu\text{m}$. Figure 2.33 shows the maximum frequency mismatch between two $m=2$ degenerate modes are smaller than $80\ \text{ppm}$, which can be considered as numerical error. Therefore, $m=2$ mode is almost immune to the misalignment of the support structure. Simulation also shows that support misalignment is having even lesser impact on the

frequency mismatch between $m=3$ degenerate modes. However, it has high impact on the rocking mode of the hemispherical shell as figure 2.34 shows.

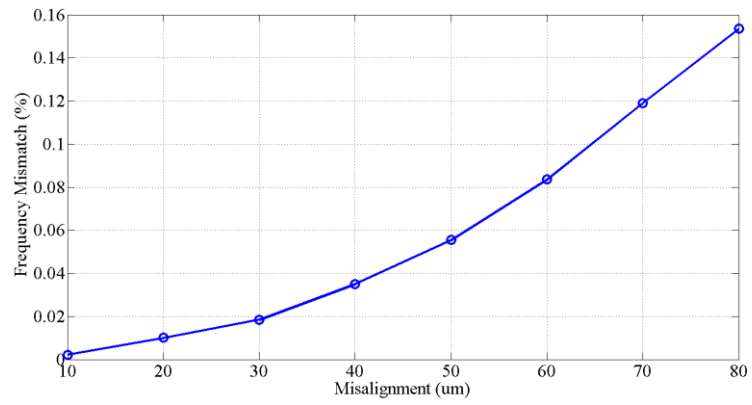


Figure 2.34: Relative frequency mismatch between rocking modes Vs. support misalignment

CHAPTER 3

FABRICATION OF SILICON DIOXIDE μ HSR

Micro-hemispherical shell resonators (μ HSR) with high quality factor (Q) and low frequency mismatch (Δf) is the first step of micro-hemispherical shell resonating gyrosopes (μ HRG). However, conventional micro-fabrication techniques are based on photolithography which is a 2D process. In this chapter, the fabrication process to create 3D micro-hemispherical shell resonators is introduced. Fabrication results and geometric characterization is also demonstrated.

3.1 Introduction

Fabrication approaches for micro-hemispherical shells have been reported by several literatures. PMMA and boron-doped silicon shells were first fabricated in 1979 for thermonuclear fusion research [68]. Shells made from gold or oxide were fabricated by a similar technique [69]. However, the target application of these shells was for packaging purposes, and they were fully detached from the substrate rather than supported by stems. Hence, their resonance characteristics were not measured. A blow-molding method based on thermoplastic forming of bulk metallic glass has been used to fabricate 3D micro shells [70]. UC Irvine has demonstrated stem-supported hemispherical shells through glass blowing and laser-cutting of individual glass spheres [71]. However, this method produced shells with inherently large stem diameters, which resulted in low quality factor resonances. In addition, laser-cutting is a serial process that is time consuming and difficult to implement during wafer-level batch fabrication [72]. Due to the finite depth of field of the laser focusing system, precise alignment is needed between the central axis of the shell and that of the rotary stage to create balanced shells. The cutting mechanism is laser ablation, which will produce residual roughness on the edge of the cut and may sputter debris back onto the shell. These are factors that can lead to asymmetry and cause frequency split

between the ideally-degenerate flexural shell modes. UC Davis reported polycrystalline diamond hemispherical shell resonators fabricated by μ EDM and micromachining showing quality factor below 3,000 and frequency split of 870 Hz [73].

Our group at Georgia Tech have recently reported polysilicon hemispherical shell resonators with integrated capacitive transducers for electrical operation [66]. The electrodes are created by boron-doping of n-type silicon wafers, forming PN junctions for isolation. The capacitive gap is defined by the sacrificial oxide layer grown from the silicon hemispherical mold, and the maximum thickness is a few microns, limiting the achievable vibration amplitudes. Difficulties in fabricating free-standing, stem-supported micro-hemispherical shells with fully isolated integrated capacitive transducers have prevented thorough mechanical characterization of such structures. In this chapter, a novel assembly method forms electrodes with large capacitive gaps surrounding the shell for rapid characterization of the thermally-grown oxide shell resonances, enabling full electrical characterization of microscale stem-supported hemispherical shells with intrinsically-unlimited support size.

We have developed thermally-grown silicon dioxide hemispherical shells released from microfabricated single-crystal silicon molds. These hemispherical shells are subsequently coated with a thin, conformal conductive film by atomic layer deposition (ALD) for electrical actuation and sensing. Integrated capacitive transducers are formed by surrounding the coated shell with silicon electrode pillars, which are fabricated from SOI wafers. These pillars are brought into place by assembly of the electrode and shell dies. With this approach, the first fully-electromechanical characterization of silicon dioxide μ HSR is performed.

3.2 Fabrication Process

This section introduces the fabrication process flow to produce silicon dioxide μ HSR that are free-standing and stem-supported. To electrically connect the hemispherical

shell and the substrate for DC polarization, the atomic layer deposition (ALD) conformal coating technique is used to create conductive coating with thickness on the order of several tens of nanometers. A subsequent die-level assembly process creates excitation and sensing electrodes around the fabricated μ HSR.

3.2.1 Hemispherical Molding Technique

One of the core technique in developing a high performance μ HSR is the mold creating method. The hemispherical mold is required to be highly symmetric with mirror-finishing smooth surface. For process compatibility, commercial available silicon wafer is selected as our starting substrate. A few literatures studied the isotropic etching technique of different types of silicon substrates. Three types of isotropic silicon etchant, HNA [62, 74], XeF_2 [62], and SF_6 plasma [75] was discuss by various literatures. XeF_2 etching is showing very rough etched surface that is not qualified for our purpose. HNA isotropic etching is highly dependent on the bath temperature, agitation rate and is difficult to control precisely with high uniformity over a silicon wafer. SF_6 plasma isotropic etch is a repeatable process with good mold symmetry and surface finishing. Therefore, SF_6 plasma is selected as our approach to create hemispherical mold.

Isotropic etching of silicon by SF_6 plasma is done by Inductively Coupled Plasma (ICP) tool by turning off the passivation step of BOSCH process. This type of blank silicon etch recipe will result in an isotropic etching of silicon. Silicon dioxide mask is firstly etched by C_4F_8 plasma to define the initial starting circular opening. Then, SF_6 plasma will perform an isotropic etching of silicon while undercutting silicon dioxide mask. Figure 3.1 shows the mold diameter as a function of etching time in STS HRM for initial circular opening of 300 μm and 400 μm , respectively. Figure 3.2 shows the mold depth as a function of etching time in the same etching tool. For a both initial opening tested, isotropic etching of 90 minutes will give a three dimensional shape close to a hemisphere. Figure 3.3 shows

(a) the hemispherical mold cavity etched in a silicon wafer and (b) an inverted silicon dioxide shell by etching away surrounding silicon.

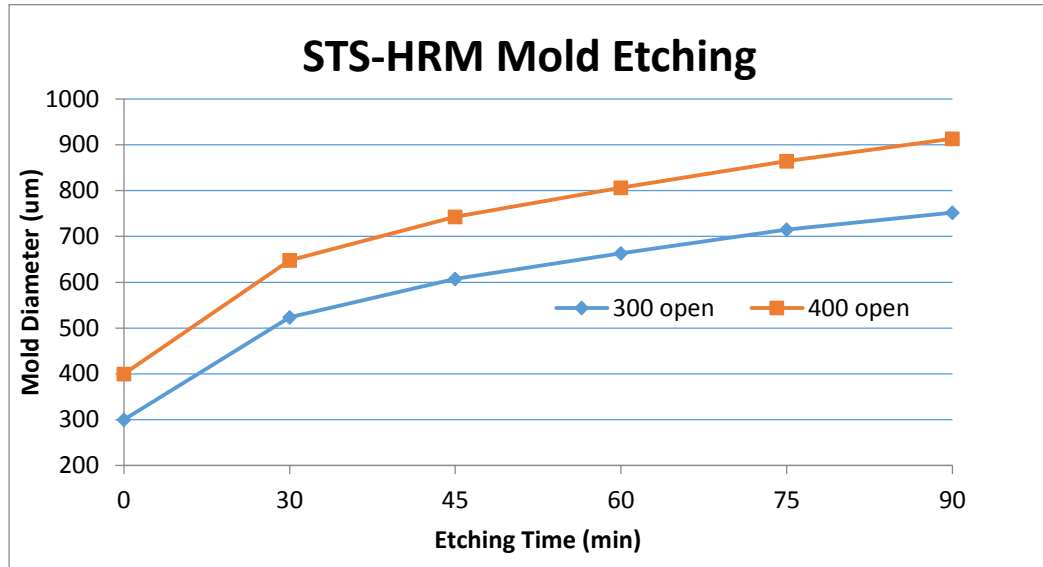


Figure 3.1: SF₆ plasma isotropic etch: mold diameter Vs. etching time

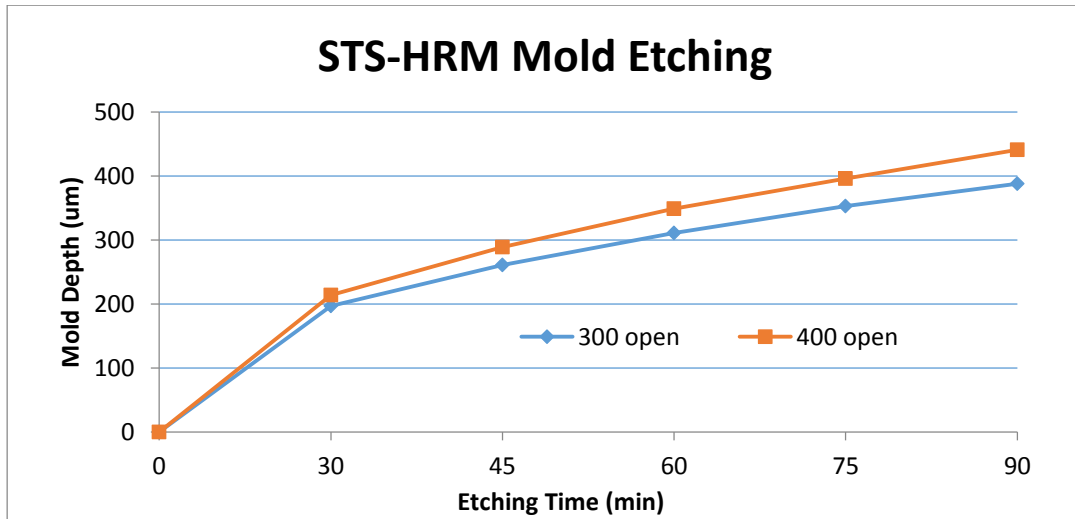
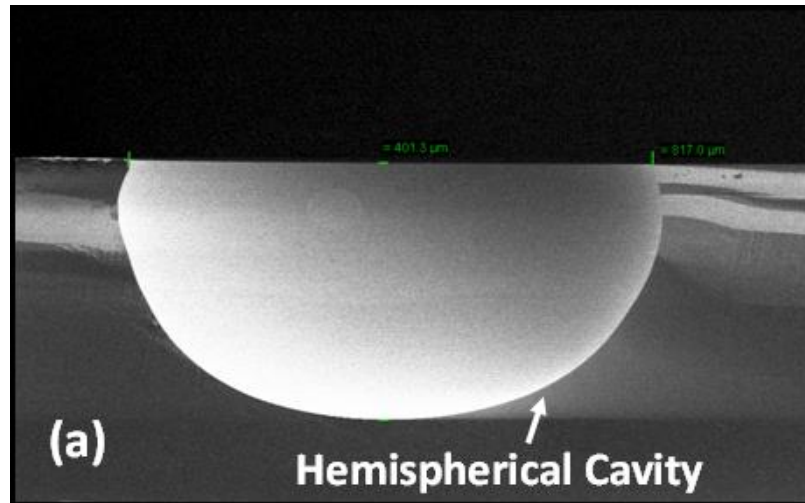
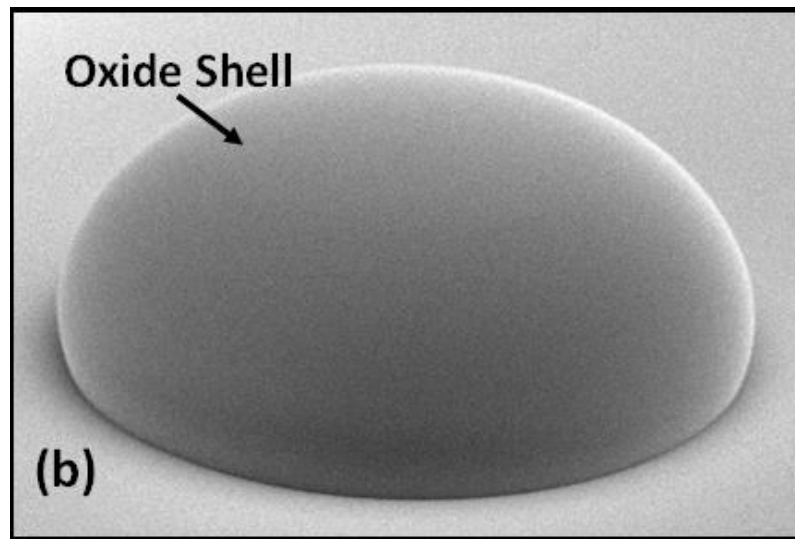


Figure 3.2: SF₆ plasma isotropic etch: mold depth Vs. etching time



(a) Hemispherical mold cavity etched in a silicon wafer



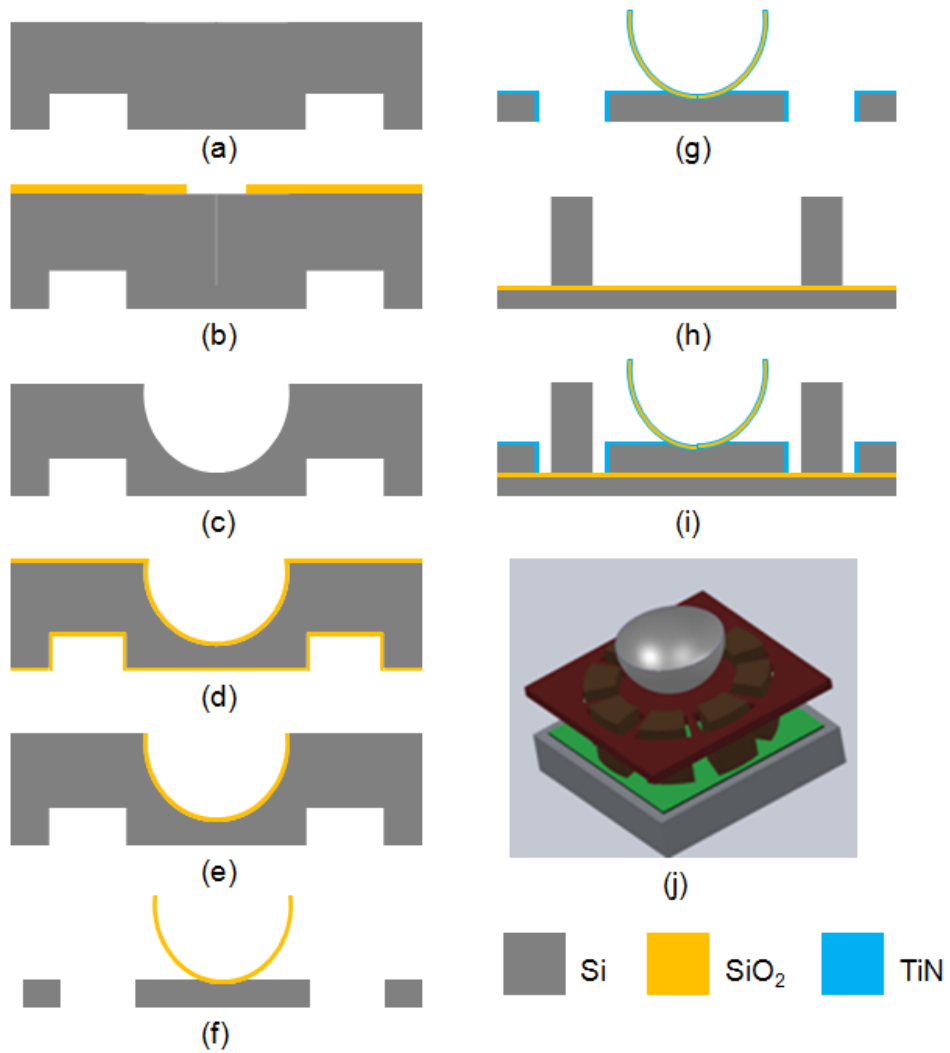
(b) An inverted silicon dioxide shell by etching away surrounding silicon

Figure 3.3: Results of isotropic silicon etching

3.2.2 Silicon Dioxide Hemispherical Shell Fabrication

In this section, the fabrication process flow of a stem-supported freestanding silicon dioxide hemispherical shell is introduced. Figure 3.4 shows an overview of the wafer-level batch-fabrication process for silicon dioxide μ HSR and the assembly with the electrode die. The process starts with a boron-doped ($100 \Omega\cdot\text{cm}$) single-crystal silicon wafer. To permit the die-level assembly, blind holes around the shell are first etched from back side

of the wafer using the Bosch process. Later in the process, these blind holes will become through holes for electrode assembly after shell release. A 7 μm thick PECVD oxide layer is deposited on the front side at 300°C, providing enough masking during the hemispherical mold creation process. A circular opening is then etched into the PECVD oxide mask by a front side to back side alignment. Silicon is then isotropically etched by SF_6 plasma to create a symmetric hemispherical mold. After the PECVD oxide mask is removed in hydrofluoric acid (HF), oxide is thermally grown at 1100°C using a wet oxidation method. Enough thickness is needed to safely go through the release step. The thermally-grown oxide on the wafer surface is removed in C_4F_8 plasma while the hemispherical mold is protected by photoresist. The remaining photoresist is removed in Piranha, leaving only oxide in the hemispherical mold. The oxide shell is released by etching the surrounding silicon in XeF_2 . Figure 3.5 shows an optical image of an array of released oxide shells. Figure 3.6 shows the SEM image of a fully-released stem-supported hemispherical shell.



Fabrication and assembly process flow of μ -wineglass: (a) etch back side blind holes for electrode assembly; (b) pattern frontside PECVD oxide mask; (c) isotropically etch silicon mold in SF_6 plasma and remove oxide mask; (d) grow thermal oxide; (e) remove oxide on top side and backside while photoresist is protecting oxide in mold; (f) release μ -wineglass by XeF_2 ; (g) atomic layer deposition (ALD) conformal coating of titanium nitride (TiN) layer; (h) etch electrode pillars on silicon-on-insulator (SOI) wafer; (i) assembly of two dies with adhesive in between (not shown); (j) three-dimensional view of assembled μ -wineglass.

Figure 3.4: Fabrication and assembly process of μ HSR

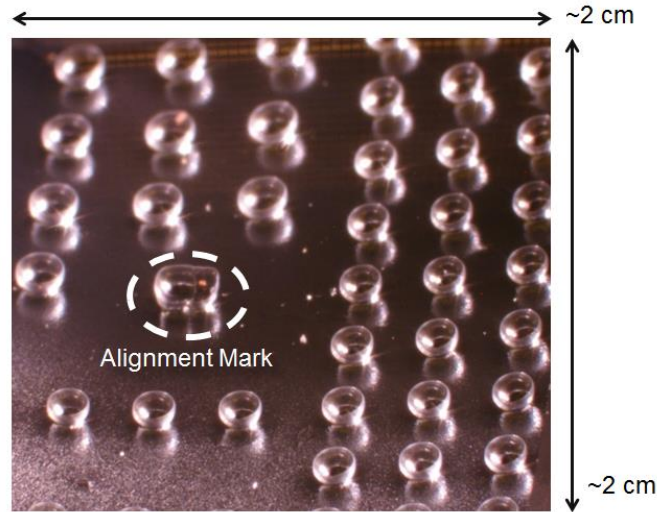


Figure 3.5: Wafer level fabrication of silicon dioxide hemispherical shells

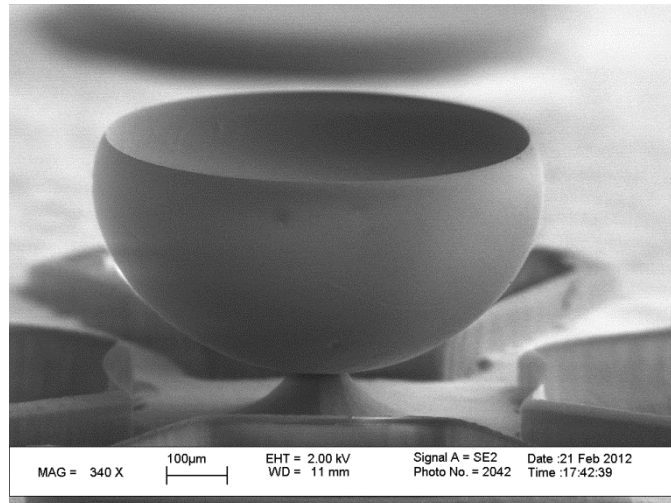


Figure 3.6: SEM image of silicon dioxide hemispherical shells

3.2.3 Conformal ALD Coating

To enable electrical testing, the silicon dioxide hemispherical shells must be coated with a conformal conductive layer that electrically connects the shell structure and the supporting substrate, providing a path for DC bias. Compared to evaporation and sputtering, atomic layer deposition (ALD) provides film with higher quality and better uniformity. Two types of ALD coating are used in this device. Sample #1 and #2 are coated with 30 nm of titanium nitride (TiN) ceramic material at 250°C, while sample #3 is coated with 35

nm of platinum (Pt) metal at 250°C, bridging the sharp transition between the oxide shell and the silicon stem (Fig. 3.6). A resistance of 800 Ω was measured between the TiN-coated shell and substrate, and 50 Ω was measured between the Pt-coated shell and substrate by probing the shell and substrate, confirming that this layer provides sufficient electrical connection for DC bias.

3.2.4 Assembly Process



Figure 3.7: Microscope image of assembled μ HSR

Due to the difficulty of integrating μ HSR and electrodes on the same process, a novel assembly process was developed for electrically exciting and sensing the resonances of our μ HSR. Electrode pillars (500 μm wide and 900 μm tall) are etched by a high aspect ratio silicon etcher STS-ICP on silicon-on-insulator (SOI) wafers to ensure electrical isolation between electrodes. The custom-made SOI wafer has a 900 μm thick device layer with a resistivity of 0.001 $\Omega\cdot\text{cm}$, buried oxide layer (BOX) of 1 μm , and handle layer of 400 μm . The μ HSR die and electrode die are carefully assembled under microscope. Adhesive is dispensed and hard-baked between the two dies to secure them together. Figure 3.7 shows a bird's eye view of an assembled device with electrodes for testing.

3.3 Process Characterization

In this section, the geometry characterization of isotropically etched hemispherical mold and the μ HSR is presented. Critical geometric parameters that will affect the performance of the μ HSR are inspected, demonstrating the success of fabricating stem-supported freestanding hemispherical shells.

3.3.1 Surface Roughness of Silicon Mold

Inductively coupled plasma (ICP) etching consists of both chemical etching and ion bombardment (physical), which will cause surface roughness. These roughness created from isotropic etching process will then transfer to the hemispherical shell structure. Our study of surface loss on μ HSR indicates that the roughness of hemispherical shell will create localized temperature distribution due to thermoelasticity, thus induces surface thermoelastic damping effect [76].

Hence, characterization of surface roughness is extremely important in high quality factor resonators. Although it is difficult to measure the shell roughness directly, any surface roughness of the silicon hemispherical mold will replicate itself (at least partially) onto the released hemispherical shell structure. Therefore, the surface roughness of the mold is characterized by a Veeco atomic force microscopy (AFM) tool. Due to the limited vertical range of the AFM tip, special preparation of the hemispherical mold needs to be made to have the tip reach the bottom of the mold. The mold was diced directly through its center by a numerically-controlled dicing saw. The AFM cantilever could then be fed from the side and the tip could reach the bottom. Figure 3.8 shows the SEM image of the surface roughness of a hemispherical mold after isotropic etching. After sample preparation, AFM measurement on hemispherical mold from the same wafer is done. Figure 3.9 shows an example 3D plot of the $3\ \mu\text{m}$ by $3\ \mu\text{m}$ bottom region of the silicon mold, and surface statistics show an average roughness R_a of 7.35 nm, root mean squared roughness R_q of

12.8 nm, and maximum height R_t of 104 nm.

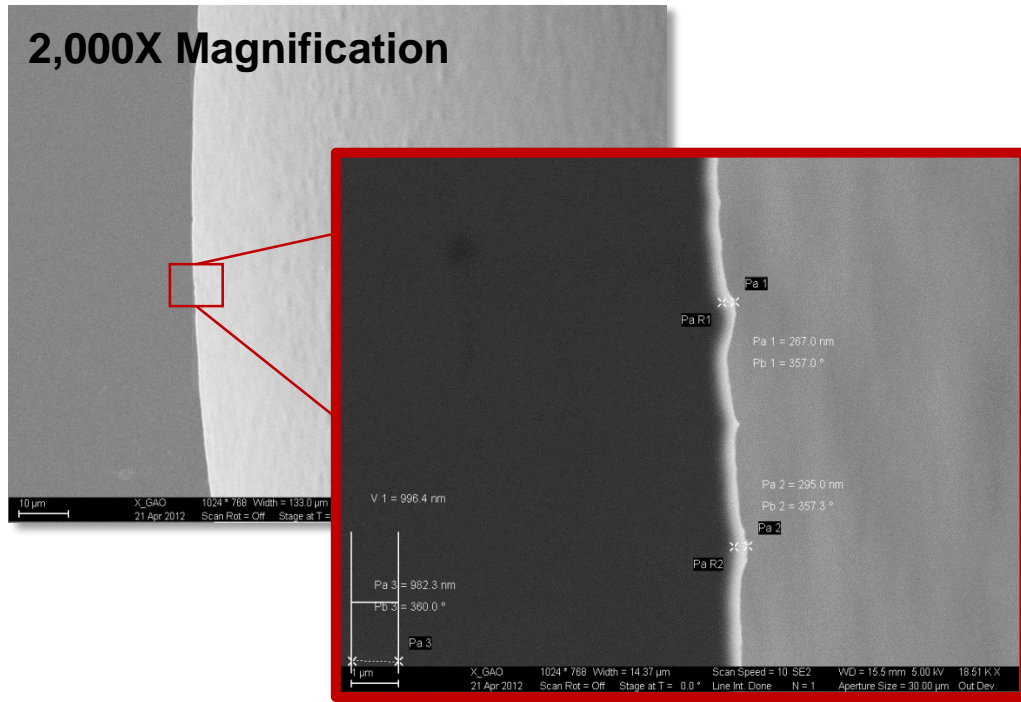


Figure 3.8: SEM image of the surface roughness of an untreated hemispherical mold

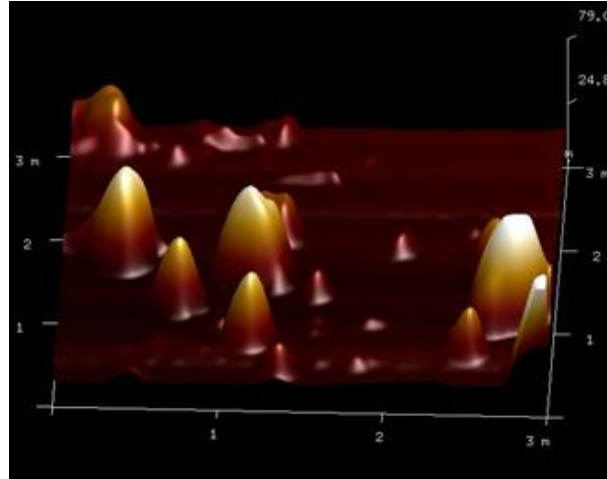


Figure 3.9: AFM measurement of the surface roughness of an untreated hemispherical mold

Thermal treatment of silicon in hydrogen atmosphere at high temperature ($>1000^{\circ}\text{C}$) can improve the surface roughness [77, 78]. The surface mobility of silicon atoms is enhanced by heated hydrogen at temperatures much lower than the melting point (1414°C). Silicon hemispherical mold etched from the same batch was anneal at 1100°C in hydrogen

atmosphere with 10 Torr pressure. This was done at Lawrence SQU. Figure 3.10 shows the silicon surface after hydrogen annealing and figure 3.11 shows the corresponding AFM measurement of the surface. The smoothed surface is difficult to focus under SEM, thus a dust particle is found in order for focusing the surface. The surface statistics show an average roughness R_a of 2.01 nm, root mean squared roughness R_q of 2.47 nm, and maximum height R_t of 15.6 nm.

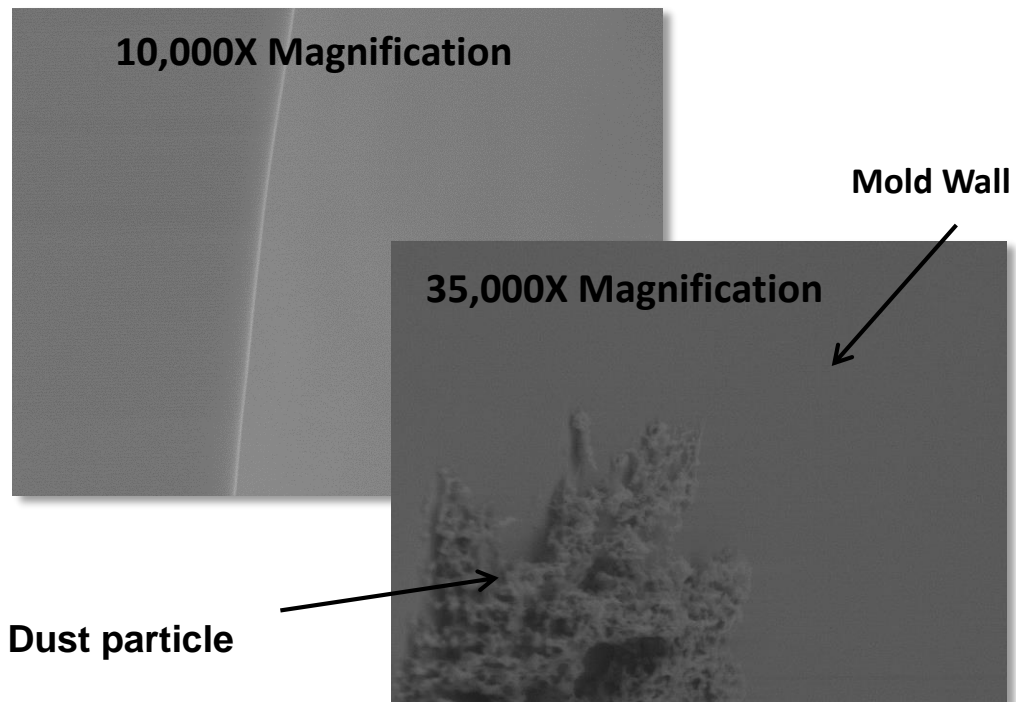


Figure 3.10: SEM image of the surface roughness of a hydrogen annealed hemispherical mold

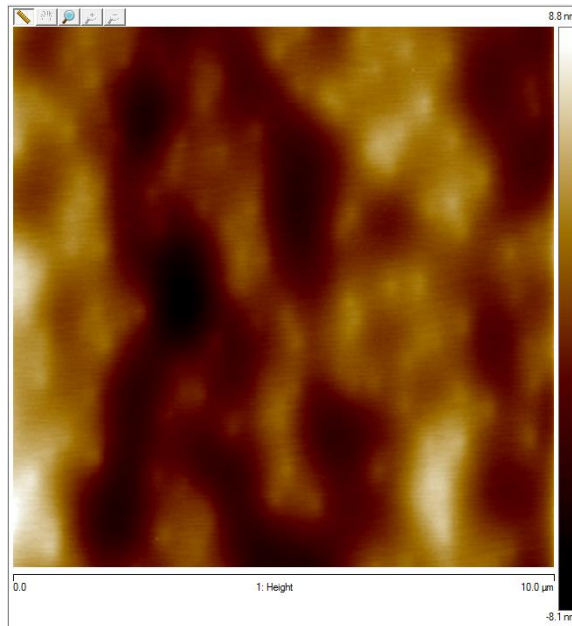


Figure 3.11: AFM measurement of the surface roughness of a hydrogen annealed hemispherical mold

3.3.2 Thickness Variation

The thickness variation due to crystalline structure of silicon is introduced in previous chapter. The thickness variation discussed in this section is introduced by the finite selectivity of silicon and silicon dioxide in XeF_2 gas, and it is not disturbing the axisymmetry of the hemispherical shell. Initially, $3.3 \mu\text{m}$ oxide was thermally grown in the silicon mold, of which the XeF_2 release consumed $1.7 \mu\text{m}$, leaving only $1.6 \mu\text{m}$ at the rim. Although XeF_2 is well-known for its high etching selectivity between silicon and silicon dioxide, the consumption of silicon dioxide is not negligible in this process. Therefore, the shell thickness is found to vary along the depth of shell. During release, the top part of the shell is released first and exposed to XeF_2 from both inner and outer sides. Thus, more oxide is consumed at the rim than at the unexposed base. By cleaving the released shell, the thickness variation along the depth of the shell could be measured under SEM. The thickness smoothly tapers from $1.6 \mu\text{m}$ at the rim to $2.2 \mu\text{m}$ close to the base as figure 3.12 shows. Thickness variation in the depth direction is tolerable since it has no impact on the axial symmetry of the shell.

The shell is found to have a re-entrant extension with a horizontally-projected dimension of 23 μm near its rim (Fig. 8). This is a result of the nature of the isotropic SF_6 mold formation. Inductively-coupled plasma (ICP) is used as the dry etching method for mold formation, during which both chemical etching and physical bombardment take place. Because it is diffusion limited, chemical etching tends to form an isotropic profile, while physical bombardment is more directional due to the momentum of the plasma, which causes the reentrant profile in the mold. Control over platen power, pressure, and etch time are expected to impact the overall shape of the hemispherical mold, reducing the reentrance, but even the macroscale HRG has a short cylindrical rim extension with minimal negative impact

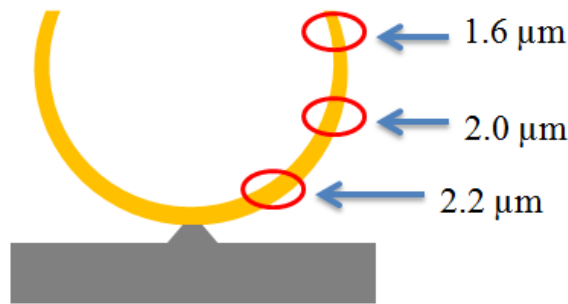


Figure 3.12: Thickness variation of silicon dioxide hemispherical shell caused by XeF_2 releasing

3.3.3 Re-entrant Extension

The shell is found to have a reentrant extension with a horizontally-projected dimension of 23 μm near its rim (Fig. 3.13). This is a result of the nature of the isotropic SF_6 mold formation. Inductively-coupled plasma (ICP) is used as the dry etching method for mold formation, during which both chemical etching and physical bombardment take place. Because it is diffusion limited, chemical etching tends to form an isotropic profile, while physical bombardment is more directional due to the momentum of the plasma, which causes the reentrant profile in the mold. Control over platen power, pressure, and etch time are expected to impact the overall shape of the hemispherical mold, reducing the

reentrance, but even the macroscale HRG has a short cylindrical rim extension with minimal negative impact.

3.3.4 Capacitive Gap

A smaller gap will give more efficient electrical transduction, lowering the motional impedance, while a larger gap can allow large drive amplitude. To reach a large drive amplitude of a few microns (3 to 5 μm), at least 30 μm capacitive gap is needed to operate the resonator in the linear region. Figure 3.13 shows the 29.4 μm capacitive gap between the μ -wineglass structure and electrode pillar.

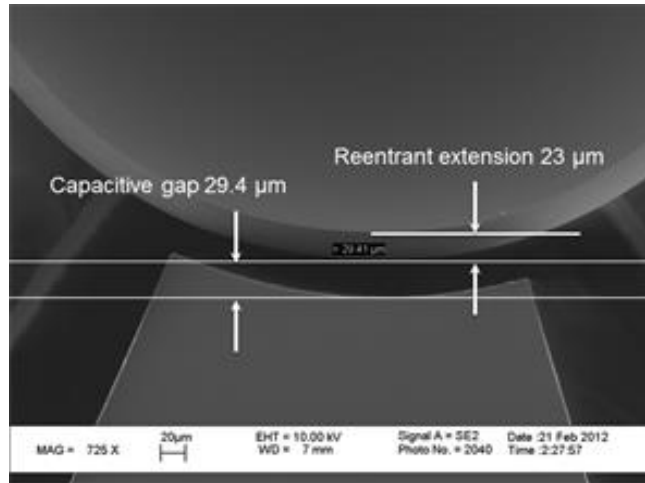


Figure 3.13: Top view SEM: showing reentrant and capacitive gap

3.3.5 Support Structure

As discussed in previous chapter on support loss and support induced anisotropy, the size and shape of support structure has a strong effect on the resonance frequency, quality factor and frequency mismatch. By monitoring the support diameter under microscope during XeF_2 release, its size can be precisely controlled and the shape of support is repeatable from run to run. Figure 3.14 shows an optical microscope image of the support structure. Interestingly, despite XeF_2 being well-known for etching silicon isotropically, the etching on 100 wafer does show crystalline preference evidenced by a

square-shaped support with 77 μm edge length. And on 111 wafer, the support is showing a triangular shape. Due to the transparency of the uncoated oxide shell, the substrate surface roughness that is formed during XeF_2 release is also visible in Figure 3.14.

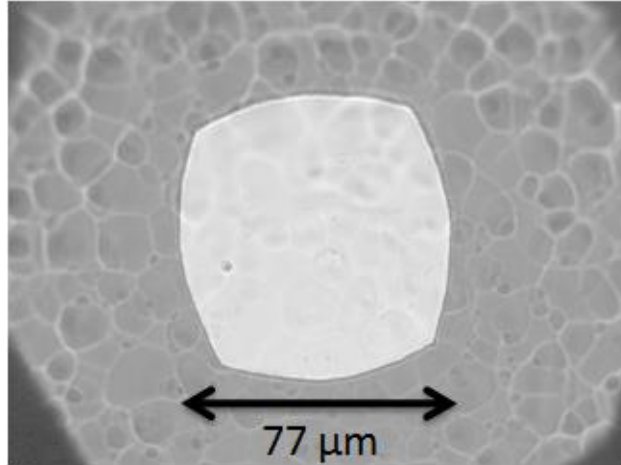


Figure 3.14: Microscopic image of the support structure

CHAPTER 4

TEST AND CHARACTERIZATION OF SILICON DIOXIDE μ HSR

This chapter introduces the characterization of ALD-coated thermally-grown silicon dioxide micro-hemispherical shell resonators (μ HSRs) with capacitive electrodes. High aspect ratio silicon dioxide μ HSRs, uniformly coated with ALD process, demonstrated quality factor as high as 19,100. An optimized isotropic dry etching recipe was developed to create highly symmetric hemispherical molds in (111) silicon substrates. The as-fabricated frequency mismatch between $m=2$ degenerate modes is achieving 21 Hz out of 8 kHz. This creates a path for fabricating high Q and highly symmetric hemispherical shell resonators for micro-hemispherical resonator gyroscopes.

4.1 Resonance Modes

This section details the electrical testing of the resonances of fabricated μ HSR that are assembled with excitation electrodes. Three batches of devices, with titanium nitride (TiN) coating (batch #1 & #3) and platinum (Pt) coating (batch #2), respectively, were tested in vacuum (10 μ Torr range) as one-port resonators. A 3D optical image of fabricated silicon dioxide μ HSR is shown in Figure 3.7. The geometric parameters of these two devices are listed in Table 4.1. An Agilent 4395A network analyzer supplies AC drive voltage that is combined with DC polarization voltage to one electrode pillar, and a sense current is generated by the change in capacitance across the polarized gaps due to vibration of the shell. A trans-impedance amplifier (TIA) is used to amplify the signal from μ HSR.

As introduced in chapter 2.1.4, the resonance frequencies of a hemispherical shell can be estimated by

$$\omega_m = \frac{m(m^2 - 1)}{R^2} \sqrt{\frac{E \cdot I(m, h)}{3(1 + \mu)\rho \cdot J(m, h)}} \quad (4.1)$$

Where,

$$I(m, h) = h^2 \int_{\varphi_0}^{\varphi_F} \frac{\tan^{2m}(\varphi/2)}{\sin^3 \varphi} d\varphi \quad (4.2)$$

$$J(m, h) = h \int_{\varphi_0}^{\varphi_F} (m^2 + 1 + \sin^2 \varphi + 2m \cos \varphi) \tan^{2m}(\varphi/2) d\varphi \quad (4.3)$$

E is Young's modulus, r is the radius of the shell, h is the shell thickness, φ_0 and φ_F are the boundary angles in spherical coordinates relative to the zenith axis, ν is Poisson's ratio, ρ is the material density, and m is the mode number.

Table 4.1: Geometric parameters of measured μ HSR

Batch #	Coating Material	Shell Diameter (μm)	Shell Thickness (μm)	Support Diameter (μm)
1	TiN	740	1.6	77
2	Pt	910	2.6	82
3	TiN	1240	1.6	90

Eigenfrequency analysis by COMSOL Multiphysics FEA software was also run to predict the frequency of each resonance mode of the μ HSRs. The support structure is also included in the FEA simulation to give more accurate prediction of resonance frequency. Table 4.2 illustrates the calculated results by (4.1), simulated results by COMSOL Multiphysics, and measured frequency results along with the measured quality factor, showing good agreement between theory and experiment.

Batch #1 and #3 are coated with 30 nm ALD TiN as the conductive layer, while 30 nm ALD Pt is used for batch #2. Batch #2 with Pt coating shows the highest quality factor of 19,100 at 19.17 kHz for $m=2$ mode and 14,300 at 55.2 kHz for $m=3$ mode, illustrated in figure 4.1 and figure 4.2, respectively. The insets are showing the mode shapes simulated by COMSOL eigenfrequency analysis. Electrostatic tuning curves for each mode are shown in figure 4.3 and figure 4.4, proving a mechanical resonance peak instead of electrical peak from characterization board. Quadratic curve fitting is also performed on

electrostatic tuning data, showing good agreement between theory and experimental results [79].

Compared with the measured results of batch #1 and batch #3, quality factor is showing a dependency on ALD coating material. Platinum coated oxide μ HSR is showing 5 times high quality factor compared to titanium nitride coated devices. The higher Young's modulus mismatch between TiN-SiO₂ interface compared to Pt-SiO₂ interface is potentially causing additional interfacial loss, and a reduced quality factor [80].

Table 4.2: Comparison of resonance frequency by equation (4.1), COMSOL FEA and measured results

Mode #	Equation (4.1) (kHz)	FEA (kHz)	Measured frequency (kHz)	Measured quality factor
Batch #1				
m=2	18.99	19.87	19.97	6,800
m=3	56.22	57.28	56.84	5,600
Batch #2				
m=2	18.84	18.38	19.17	19,100
m=3	55.76	53.22	55.20	14,300
Batch #3				
m=2	6.79	6.67	6.62	5,900
m=3	19.72	20.62	20.51	5,100

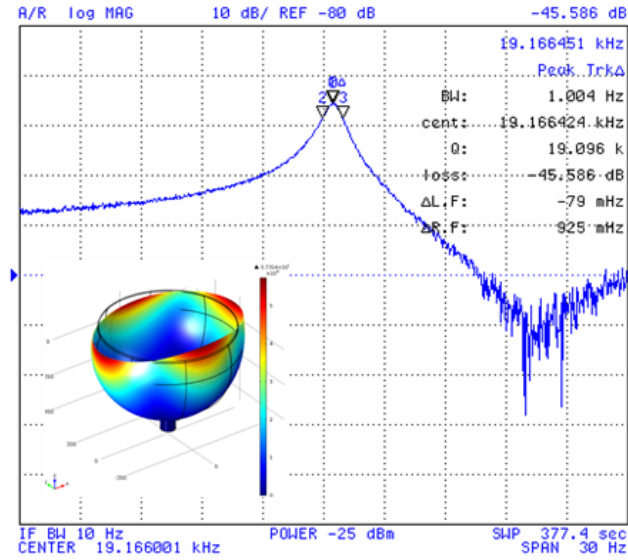


Figure 4.1: $m=2$ mode resonance peak of silicon dioxide μ HSR (inset: mode shape)

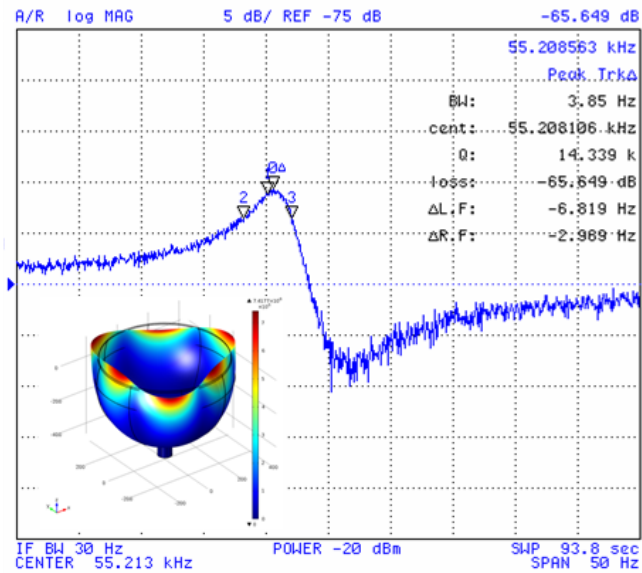


Figure 4.2: $m=3$ mode resonance peak of silicon dioxide μ HSR (inset: mode shape)

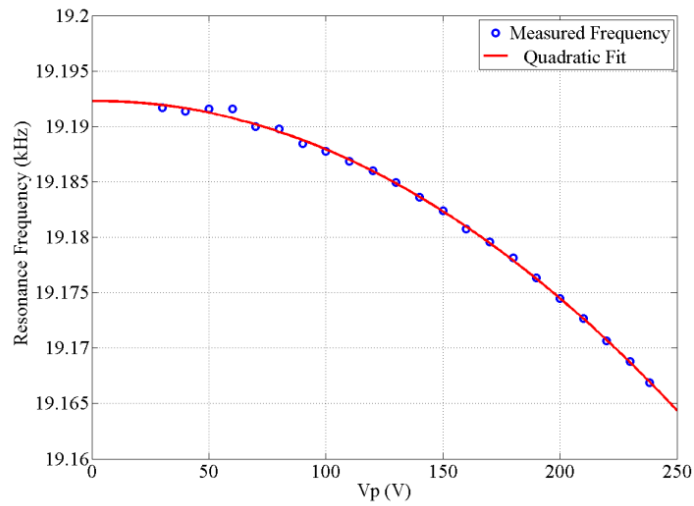


Figure 4.3: Electrostatic tuning curve of $m=2$ mode resonance of silicon dioxide μ HSR, fitted with quadratic equation

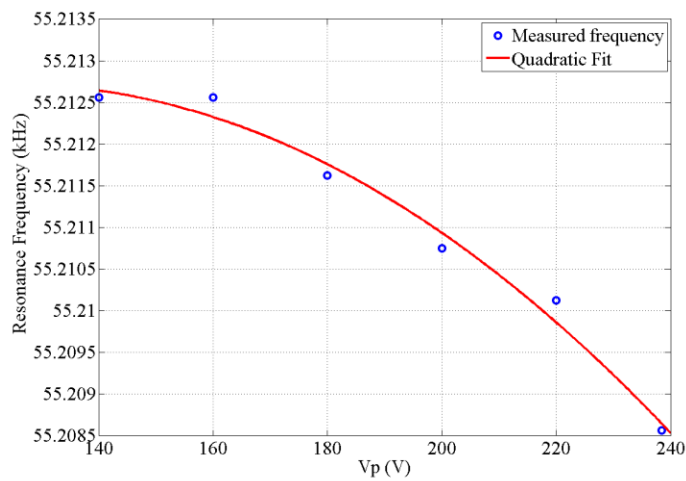


Figure 4.4: Electrostatic tuning curve of $m=3$ mode resonance silicon dioxide μ HSR, fitted with quadratic equation

4.2 Ring Down Test

One of the operating modes of HRG is rate integrating mode (whole angle mode). In this operating mode, the resonator is excited by a delta function and allowed to precess freely without any further excitation as introduced in chapter 1. Due to the way that rate integrating mode works, long ringdown time of the resonator is preferred. Thus, a time domain ringdown test is also performed for μ HSR.

Figure 4.5 illustrates the schematic view of ringdown test setup³. A feed-through cancellation circuit is designed and connected in parallel with the input and output of the resonator. By tuning the potentiometer R_{IN1} , a negative capacitance that equals to the feed through capacitance of the device is created by the feedthrough cancellation block. Trans-impedance amplifier (TIA) and post amplifier circuit enhance the signal for display on oscilloscope. Figure 4.6 shows a picture of the prototype of the test boards. The resonance peak is firstly measured by network analyzer with feed-through cancellation circuit. By setting frequency span to 0 Hz, the excitation is locked at the resonance frequency. Once the connection is switched from network analyzer to digital oscilloscope, the transient waveform can be recorded.

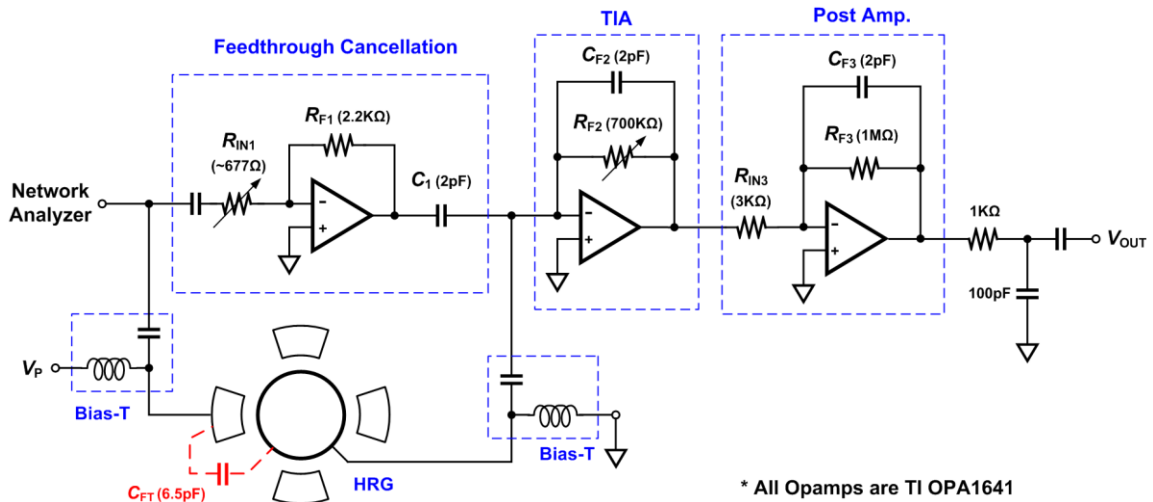


Figure 4.5: Illustration of electronic setup for ringdown measurement

³ Courtesy of Chang-Shun Liu on ringdown measurement

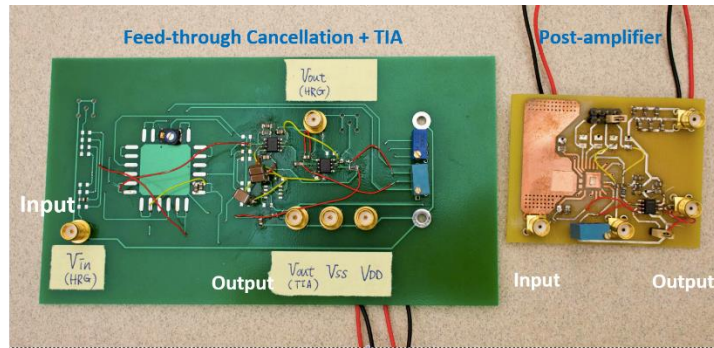


Figure 4.6: Prototype of ringdown measurement circuit

Figure 4.7 and figure 4.8 show the measured resonance peak by network analyzer and corresponding ringdown measurement. For a μ HSR from batch #3, a quality factor of 5,900 at 6.62 kHz is measured at frequency domain. The ring down time of the resonance peak shown in figure 4.7 can be calculated by:

$$\tau = \frac{Q}{\pi f} \quad (4.4)$$

where Q is the quality factor and f is the resonance frequency. Ringdown time of 284.7 ms can be calculated by equation (4.4) while the measured result is 292 ms, showing good agreement between time domain and frequency domain measurements.

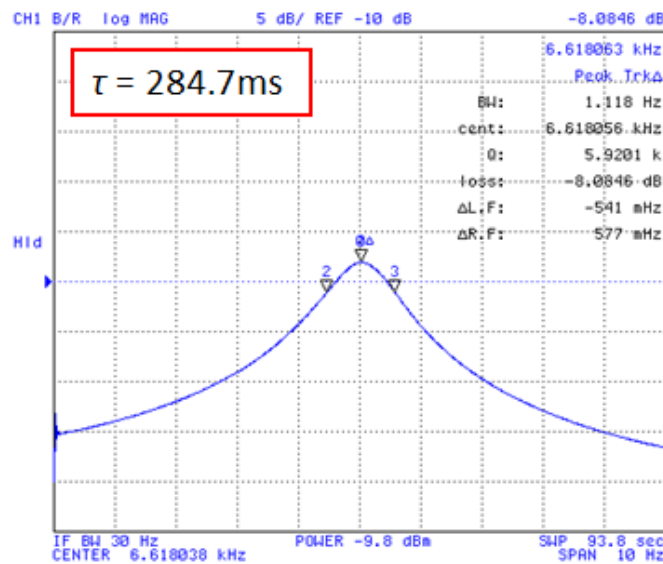


Figure 4.7: m=2 resonance peak of a batch #3 device

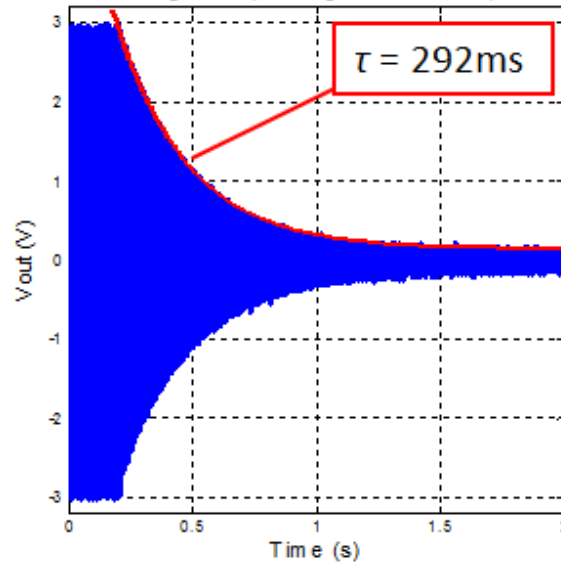


Figure 4.8: Ringdown measurement of a batch #3 device

4.3 Environmental Behavior

In order to study the loss mechanism on this device, quality factor is measured at various environment conditions. Figure 4.9 illustrates the measured quality factor of batch #2 device at different vacuum level. At sub-mTorr range, the quality factor does not show significant dependency on chamber pressure, while air damping will dominate when chamber pressure is above 1 mTorr. Therefore, the quality factor is not limited by air damping at current vacuum level. For resonators that operated at Knudsen region, the air damping Q is inversely proportional to the air pressure. The proportional constant is extracted by the data at 30 mTorr (data point at highest pressure), and the air damping Q is plotted as the dashed line in Figure 4.9. This curve predicts that if other loss mechanism are all eliminated, vacuum level of 100 μ Torr or better is needed to reach Q_s in excess of one million.

The temperature behavior of the SiO_2 μ HSR is measured to understand how resonance frequency and quality factor change over temperature. Vacuum chamber with μ HSR inside is placed in a temperature oven with both heater and compressor.

Measurement is done from 10°C to 90°C for batch #2. Four hours stabilization time was given between two temperature points. As shown in Figure 4.10, a linear and positive temperature coefficient of frequency (TCF) of 61.9 ppm/°C is extracted by linear regression of the resonance frequencies at different temperatures. The relatively smaller TCF value compared to a silicon dioxide resonator is due to the loading of negative TCF of Pt coating. Theoretical calculation shows a TCF of 59.8 ppm/°C, which matches the experimental result. Quality factor also shows an inverse trend at temperatures above 40°C.

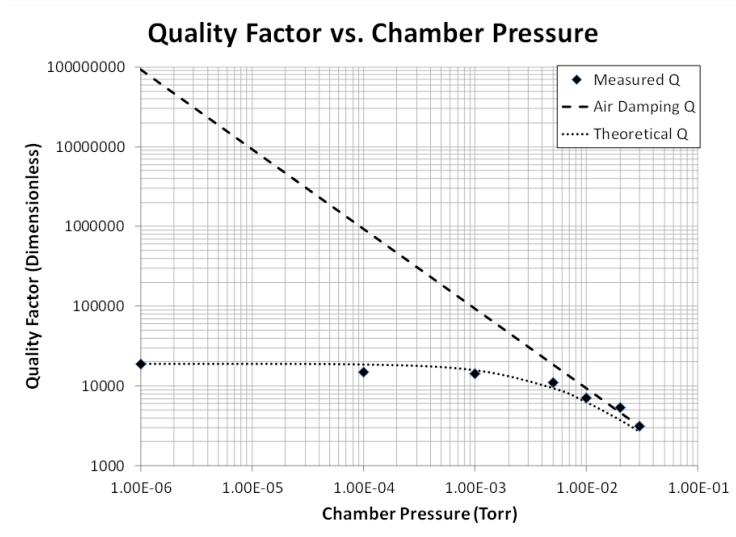


Figure 4.9: Quality factor Vs. vacuum pressure

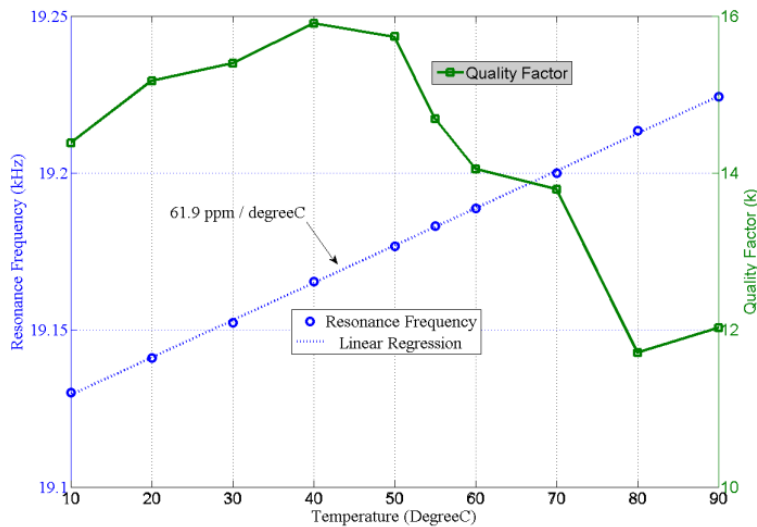


Figure 4.10: TCF and quality factor Vs. temperature

4.4 Frequency Mismatch

For axis-symmetric gyroscopes, frequency mismatch between two degenerate fundamental modes is a critical performance. This mismatch reflects the level of symmetry of the structure as well as the difficulty in order for mode matching. Single crystal silicon wafer (100) and (111) are used as the starting substrates. Known as an anisotropic material with four fold symmetry, (100) silicon wafer shows 4th harmonics in hemispherical molding process, while (111) silicon wafer shows 6th harmonics. As simulated in section 2.3.1, this type of anisotropy significantly affects frequency mismatch between $m=2$ and $m=3$ degenerate modes. Figure 4.11 and figure 4.12 show the measured frequency mismatch of 320 Hz ($\Delta f/f = 4.9\%$) between $m=2$ modes and 99 Hz ($\Delta f/f = 0.48\%$) between $m=3$ modes of μ HSR fabricated out of (100) silicon substrate. Figure 4.13 and figure 4.14 show the measured frequency mismatch of 21 Hz ($\Delta f/f = 0.26\%$) between $m=2$ modes and 474 Hz ($\Delta f/f = 1.95\%$) between $m=3$ modes of μ HSR fabricated out of (111) silicon substrate.

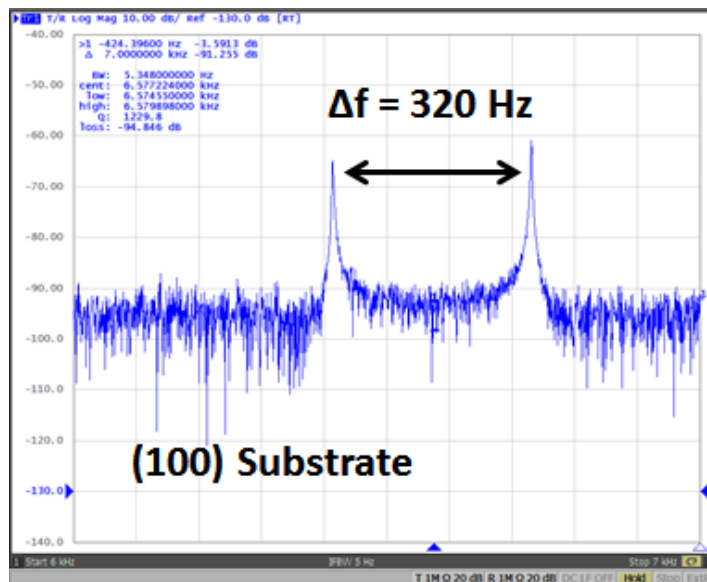


Figure 4.11: Frequency mismatch between $m=2$ degenerate modes for μ HSR fabricated out of (100) wafer

These testing results on frequency mismatch of $m=2$ and $m=3$ modes of silicon dioxide μ HSR fabricated out of (100) and (111) silicon substrate agree well with the simulation results presented in section 2.3.1. The additional mismatch is mostly likely due to the misalignment of the cut of silicon wafer. Therefore, for μ HSR that has high degree of symmetry of $m=2$ modes, (111) silicon substrate will be selected as the starting substrate.

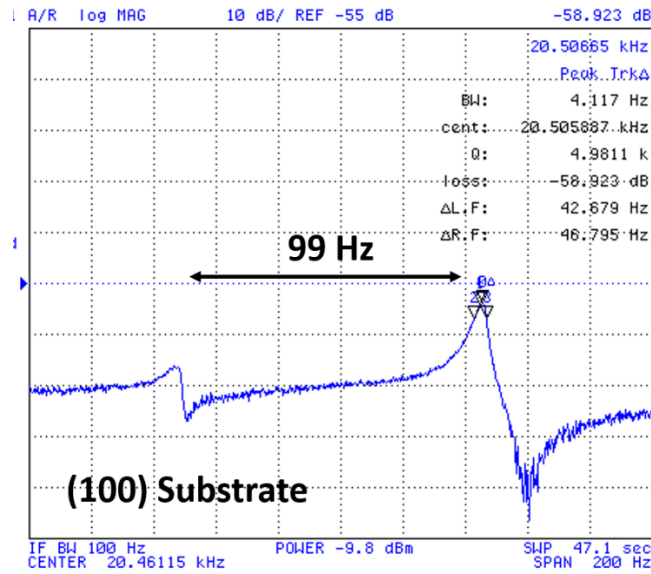


Figure 4.12: Frequency mismatch between $m=3$ degenerate modes for μ HSR fabricated out of (100) wafer

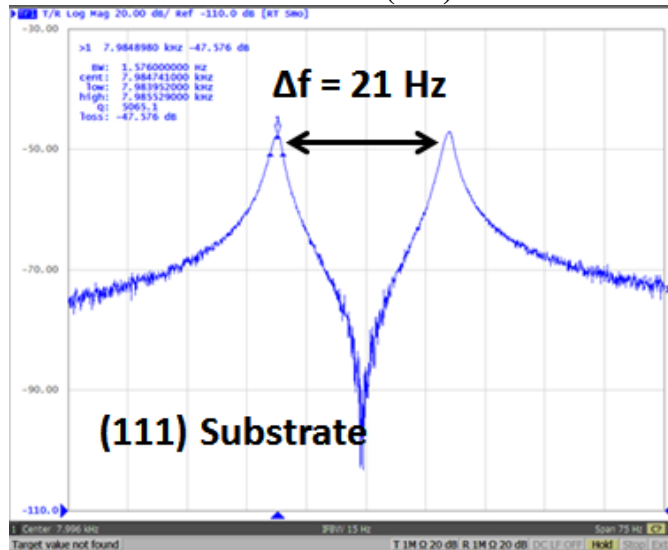


Figure 4.13: Frequency mismatch between $m=2$ degenerate modes for μ HSR fabricated out of (111) wafer

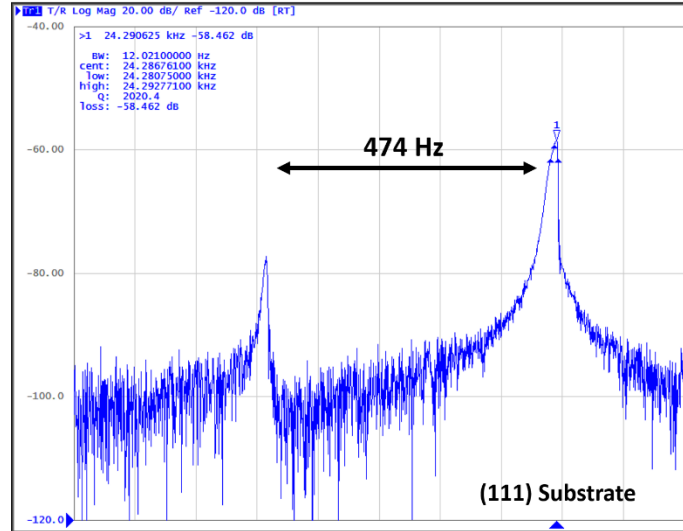


Figure 4.14: Frequency mismatch between $m=3$ degenerate modes for μ HSR fabricated out of (111) wafer

4.5 Optical Measurement

For silicon dioxide μ HSR, one possible loss mechanism is surface loss caused by additional conductive coating. The difference of Young's Modulus between two materials will cause interfacial slip, thus energy loss. In order to eliminate this type of energy dissipation, uncoated silicon dioxide μ HSR is tested by optical displacement probe setup at Northrop Grumman Corporation. Figure 4.15 shows the schematics of the optical test setup⁴. The μ HSR is mounted on a PZT stage inside a vacuum chamber with 0.5 mTorr pressure. To actuate the μ HSR, The PZT stage is connected to a function generator that can perform frequency sweeping. A Philtec D6 optical displacement probe is used to detect the vibration amplitude of the μ HSR. Figure 4.16 shows the actual test setup. Multiple tests run at 0° and 45° locations. Data is recorded at the frequency of 300 kHz for higher resolution. Figure 4.17 shows the ringdown curve of multiple runs at different locations. Figure 4.18 shows the test results of frequency sweep. Table 4.3 shows the statistical analyses of the results. The highest quality factor of 67,000 is measured with frequency mismatch of 5 Hz between two $m=2$ degenerate modes.

⁴ Courtesy of Northrop Grumman on optical measurement

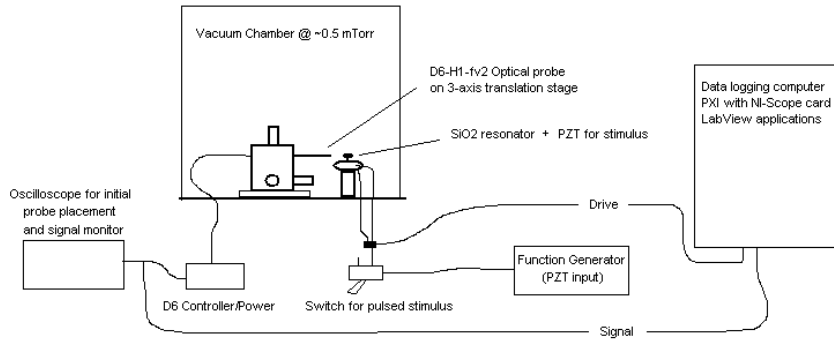


Figure 4.15: Schematics of optical test setup (Courtesy of Northrop Grumman)



Figure 4.16: Optical test setup (Courtesy of Northrop Grumman)

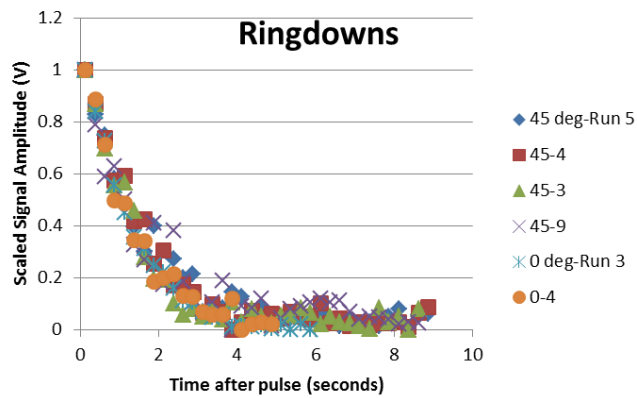


Figure 4.17: Optical ringdown test results (Courtesy of Northrop Grumman)

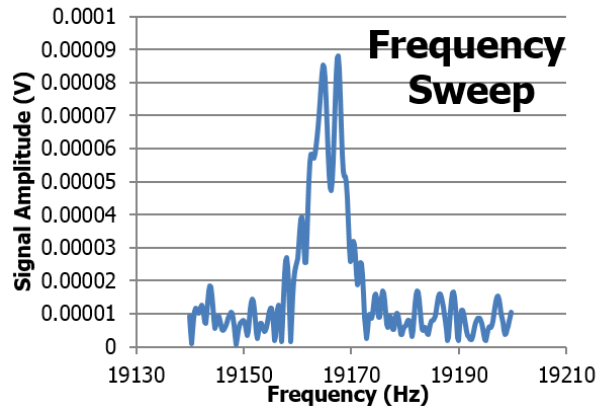


Figure 4.18: Frequency sweep test results (Courtesy of Northrop Grumman)

Table 4.3 Summary of optical test results

	0°	45°	Difference
Decay Time (s)	1.077	1.112	0.035
Frequency (Hz)	65,000	67,000	2,000
Quality Factor	19165	19170	5

4.6 Static Stiffness Measurement

Another interesting feature of μ HSR is its extremely low stiffness. This will result in less power consumption and larger tuning range. The static stiffness of this device is measured by Femtotools FT-S1000-LAT lateral microforce sensing probe⁵. The measurement system is shown in figure 4.19. Force versus deflection curve of the μ HSR is recorded, and the mechanical stiffness is extracted as figure 4.20 shows. Mechanical stiffness of 10 N/m can be calculated by linear regression, compared to stiffness of 800 N/m for conventional tuning fork gyroscope operated at 13 kHz [18].

⁵ Courtesy of Femtotools on static stiffness measurement



Figure 4.19 Static stiffness measurement system (Courtesy of Femtotools)

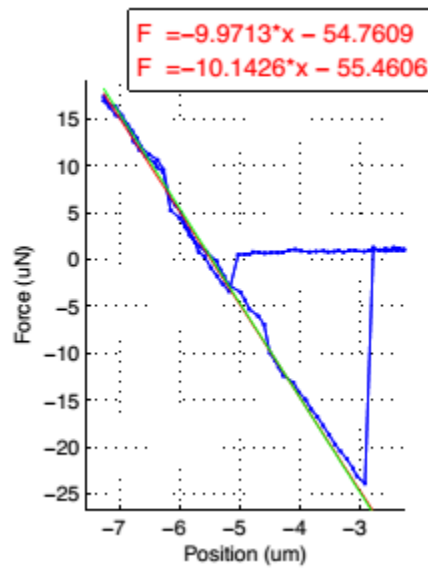


Figure 4.20: Static deformation measurement (Courtesy of Femtotools)

CHAPTER 5

ELECTROMECHANICAL DESIGN AND SIMULATION OF MICROSCALE HEMISPHERICAL SHELL RESONATING GYROSCOPES (μ HRG)

To build a gyroscope out of the hemispherical shell resonator introduced in previous chapters, capacitive transducer is needed to drive the resonator and sense the Coriolis effect. For axial symmetric structure that uses $m=2$ resonance mode, 16 electrodes are designed uniformly distributed around the hemispherical shell as figure 5.1 shows. Electrodes at 0° , 90° , 180° and 270° are at the antinodes of the drive mode. They are used for driving the resonator, or detecting the drive mode. Electrodes at 45° , 135° , 225° and 315° are at the nodes of the drive mode, which is also the antinodes of the sense mode. They are used for detecting the sense mode, or tuning the sense mode. The remaining electrodes at $22.5^\circ + n45^\circ$ are used for balancing the resonance modes, where n is an integer [81]. The detailed control mechanism will be discussed in detail in Chapter 7. In this chapter, the effect of the capacitive transducer is studied. Proper capacitive gap size and electrode structure is designed.

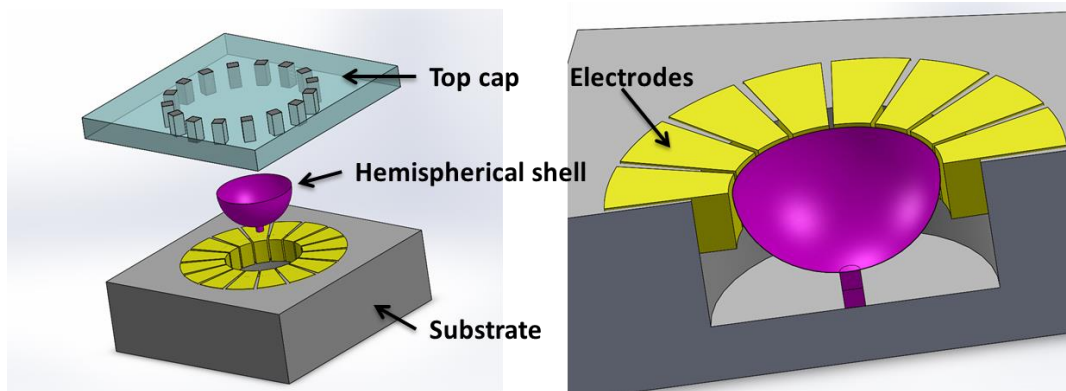


Figure 5.1: Schematic diagram of the μ HRG

5.1 Pull-in Voltage

For a parallel-plate capacitive transducer actuator, the travel range is limited. Thus the applied DC voltage is limited by the pull-in voltage. Figure 5.2 shows the lumped parameter model of a capacitive transducer. The electrostatic potential energy can be written as:

$$u = \frac{1}{2} CV^2 = \frac{1}{2} \frac{\epsilon A}{d} V^2 \quad (5.1)$$

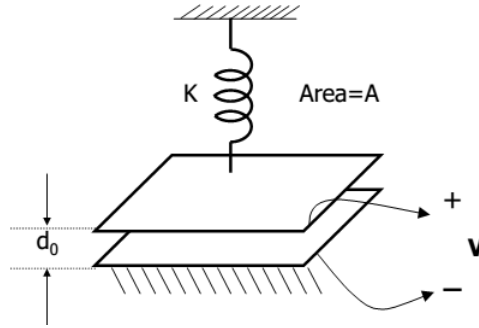


Figure 5.2: Lumped parameter model of a capacitive transducer

Then the electrostatic force can be calculated as:

$$F_{electrostatic} = -\frac{\partial u}{\partial d} = \frac{1}{2} \frac{\epsilon AV^2}{d^2} \quad (5.2)$$

The electrostatic force is then independent of voltage polarity. Assuming steady state condition, for an electrostatically induced deflection x along the gap

$$F_{electrostatic} = \frac{1}{2} \frac{\epsilon AV^2}{(d-x)^2} = Kx \quad (5.3)$$

Thus,

$$V^2 = 2 \frac{Kx}{\epsilon A} (d-x)^2 \quad (5.4)$$

The pull-in voltage can be calculated by setting:

$$\frac{dV}{dx} = 0 \quad (5.5)$$

Therefore, the pull-in voltage and the maximum deflection at pull-in voltage is:

$$\begin{cases} V_{pull-in} = \sqrt{\frac{8Kd^3}{27\varepsilon A}} \\ x_{pull-in} = \frac{d}{3} \end{cases} \quad (5.6)$$

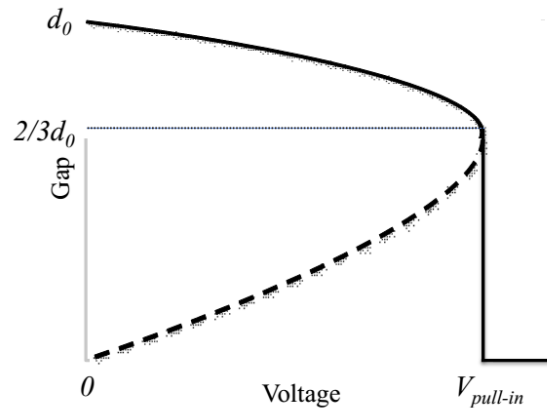


Figure 5.3: Electrostatic deflection Vs. DC voltage

Figure 5.3 shows the trend of deflection as increasing DC voltage. As DC voltage is increasing from 0, the deflection is showing a quadratic curve as a function before pulling in. When the voltage reaches pull-in voltage, the deflection suddenly becomes the same as the gap size.

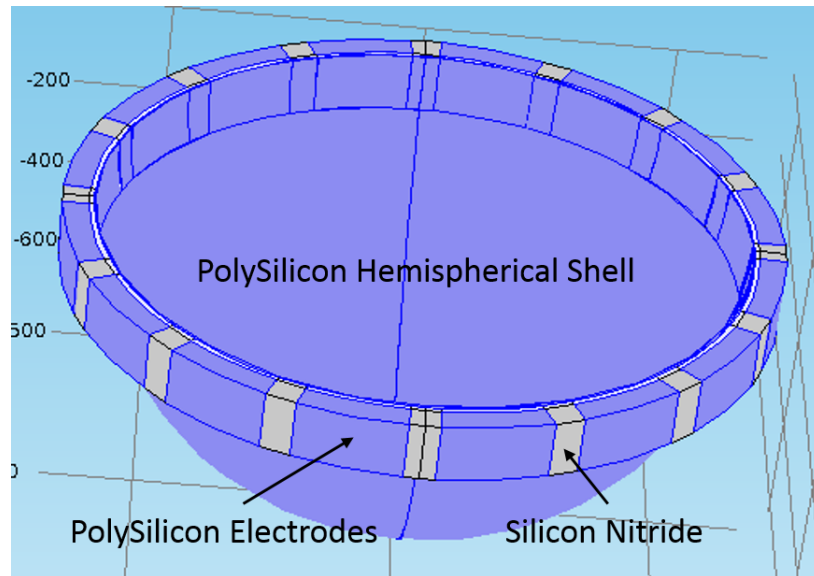


Figure 5.4: Electromechanical model of μ HRG in COMSOL

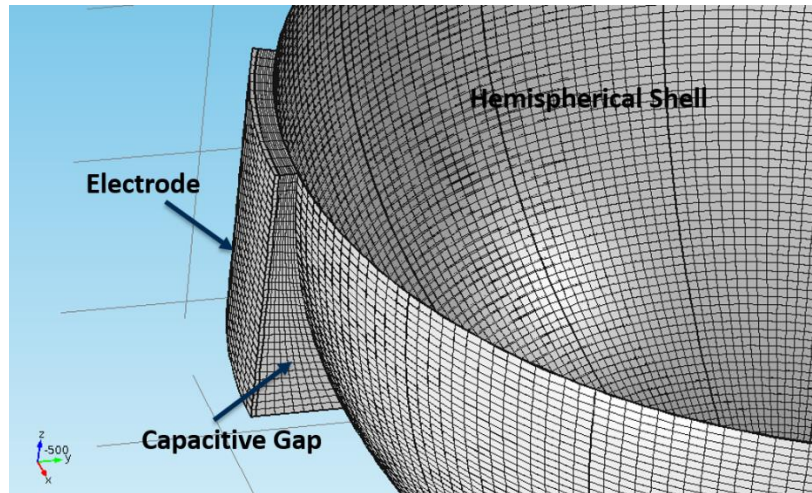


Figure 5.5: Electromechanical model of μ HRG: cross section of single electrode

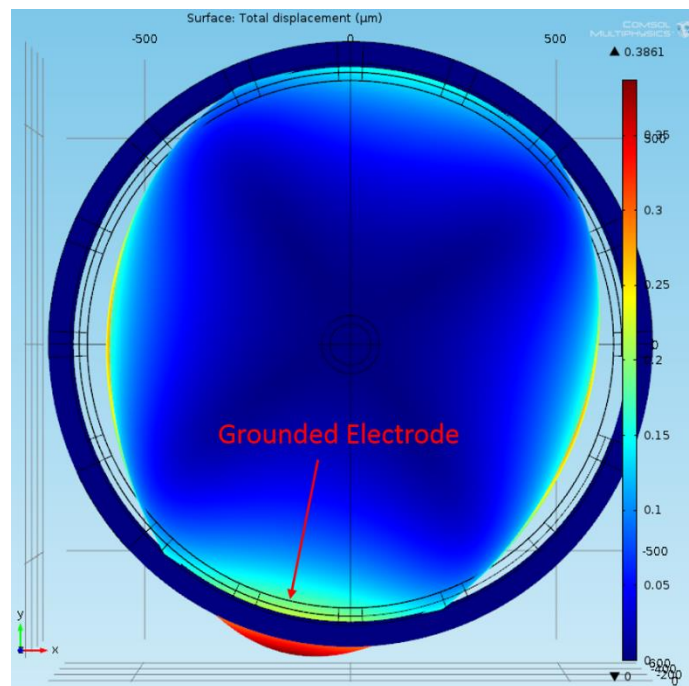


Figure 5.6: Simulated hemispherical shell deformation in response of 40 V DC voltage

The electromechanical model is built in COMSOL Multiphysics with the physics of electro-mechanics as shown in figure 5.5. A polysilicon hemispherical shell with radius of $620 \mu\text{m}$, thickness of $1 \mu\text{m}$ and circular support radius of $50 \mu\text{m}$ is used as the test structure. The electrode is $300 \mu\text{m}$ in depth and 20° circumferential span, with minimum capacitive gap of $10 \mu\text{m}$, $20 \mu\text{m}$ and $30 \mu\text{m}$. The adjacent electrodes are separated by silicon nitride.

The hemispherical shell is given a DC potential, and one of the electrodes is grounded while others are biased at the same DC potential with the hemispherical shell. A stationary analysis is run at different voltages to find out the static displacement at different DC voltages.

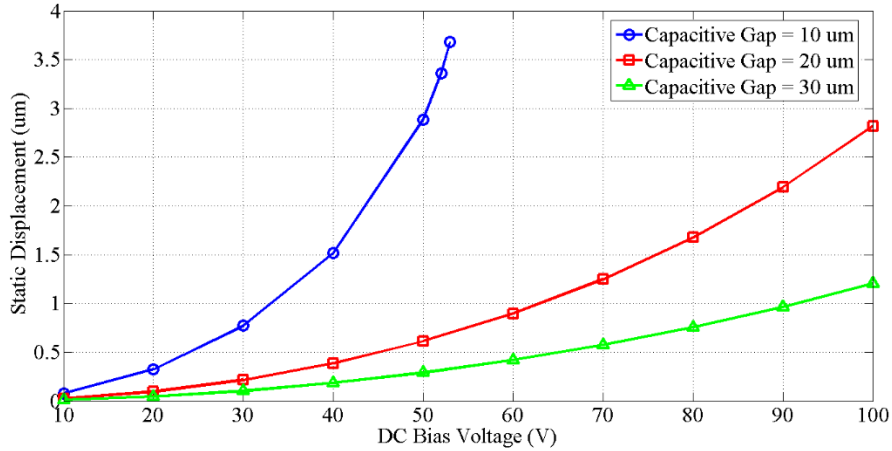


Figure 5.7: Simulated static displacement of hemispherical shell Vs. applied DC bias voltage

Figure 5.6 shows the deformation of hemispherical shell with 20 μm capacitive gap in response to 40 V DC bias voltage. It is interesting to notice that although only single electrode is used, the deformation is showing the elliptical shape similar to the mode shape of $m=2$ mode. Figure 5.7 illustrates the COMSOL simulation results when sweeping the DC voltage from 10 V to 100 V for three different capacitive gap sizes. It clearly shows a quadratic forms trend which agree with the theory. For a gap size of 10 μm , the simulation does not converge when applying a DC voltage larger than 53 V, which means at this voltage the structure has already pulled in. It is also interesting to notice that at the voltage right before pull-in, the displacement is 3.68 μm which is approximately one third of the gap size. For gap size of 20 μm and 30 μm , the structure is not pulling in at DC bias of 100 V. Therefore, it is safe to apply DC voltages below 100 V on this device without pulling in.

5.2 Electrostatic Tuning

For parallel plate transducer, the frequency of a resonator can be fine-tuned by the DC polarization voltage. This phenomenon is also called electrostatic spring softening effect, which enable mode matching of MEMS gyroscopes [18, 28, 33]. The amount of frequency that can be tuned is also very important to a gyroscope design. This tuning range has to be able to compensate for the as-fabricated frequency mismatch in order for mode matching.

Considering the electrostatic force with DC bias and a small AC component:

$$F_{electrostatic} = \frac{1}{2}(V_p + V_{ac})^2 \frac{\partial C}{\partial x} = \frac{1}{2}(V_p^2 + 2V_p V_{ac} + V_{ac}^2) \quad (5.7)$$

Where with Tylor's series, the derivative of capacitance can be written as:

$$\frac{\partial C}{\partial x} = \frac{C_0}{d \left(1 - \frac{x}{d}\right)^2} = \frac{C_0}{d} \left(1 + \frac{2}{d}x + \dots\right) \quad (5.8)$$

Assummng linear operation ($x < 0.1d$) and $V_{ac} \ll V_p$:

$$\begin{aligned} F_{electrostatic} &= \frac{1}{2}(V_p^2 + 2V_p V_{ac} + V_{ac}^2) \frac{C_0}{d} \left(1 + \frac{2}{d}x\right) \\ &= \frac{1}{2}V_p^2 \frac{C_0}{d} + V_p^2 \frac{C_0}{d^2}x + V_p V_{ac} \frac{C_0}{d^2}2x + V_{ac}^2 \frac{C_0}{d^2}x + V_p V_{ac} \frac{C_0}{d} + \frac{1}{2}V_{ac}^2 \frac{C_0}{d} \quad (5.9) \end{aligned}$$

In this expanded form, by the assumption that $V_{ac} \ll V_p$, the term $(V_p V_{ac} \frac{C_0}{d^2}2x + V_{ac}^2 \frac{C_0}{d^2}x)$ can be ignored because these are higher order stiffness terms, and $\frac{1}{2}V_{ac}^2 \frac{C_0}{d}$ can be ignored too because this is higher order small force. Therefore, by equating the above equation with the lumped parameter model of a resonator, we can obtain:

$$M\ddot{x} + D\dot{x} + Kx - V_p^2 \frac{C_0}{d^2}x = \frac{1}{2}V_p^2 \frac{C_0}{d} + V_p V_{ac} \frac{C_0}{d} \quad (5.10)$$

So, there introduces a electrical stiffness term of $-V_p^2 \frac{C_0}{d^2}x$. The electrode acts as if an added negative spring at that location. Therefore, the frequency of the resonator becomes:

$$\omega_{electro-mechanical} = \sqrt{\frac{K_{mech} - V_p^2 \frac{C_0}{d^2} x}{M}} \quad (5.11)$$

To simulate electrostatic tuning effect, pre-stressed eigenfrequency analysis is run on the same electromechanical model in COMSOL Multiphysics. Figure 5.6 shows the tuning curve from 0 V to 80 V for different capacitive gap sizes. The device with capacitive gap of 20 μm is showing a tuning range larger than 200 Hz for 80 V.

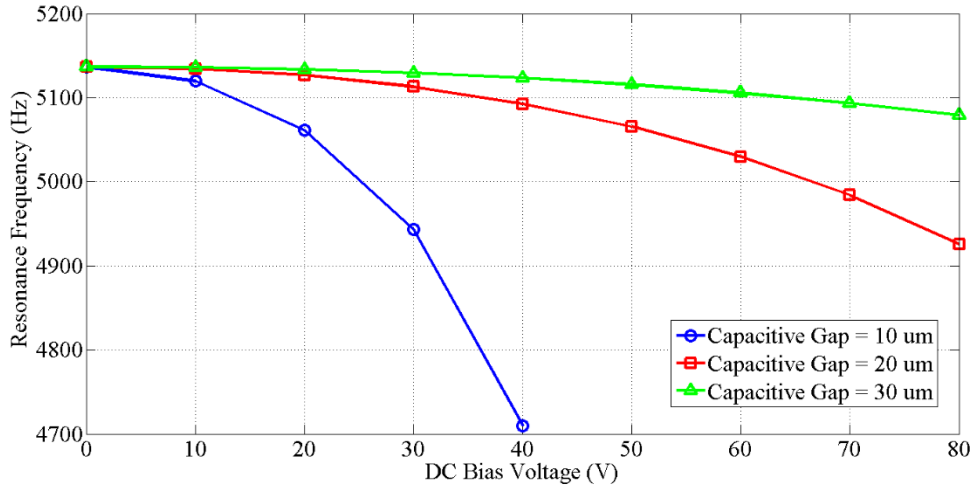


Figure 5.8: Simulated electrostatic tuning curve

In designing a tunable electrostatic resonant device with capacitive transducer, capacitive gap is designed to have a large full-in voltage with enough tuning range. Therefore, the gap size of 20 μm is selected for this hemispherical resonating gyroscope design for these considerations.

5.3 Drive Amplitude

During the operation of the μHRG , the hemispherical shell is firstly driven into resonance by applying a DC bias on the body of the shell and an AC signal on one of the electrodes. The drive amplitude has a large effect on sensitivity and mechanical noise of the gyroscope. The drive amplitude can simply be written as:

$$x = \frac{F_{electrostatic} Q_d}{\omega_0^2 M_{eff}} \quad (5.11)$$

Where, $F_{electrostatic}$ is the electrostatic force, Q_d is the drive mode quality factor, ω_0 is the resonance angular frequency, M_{eff} is the effective mass of that particular resonance mode.

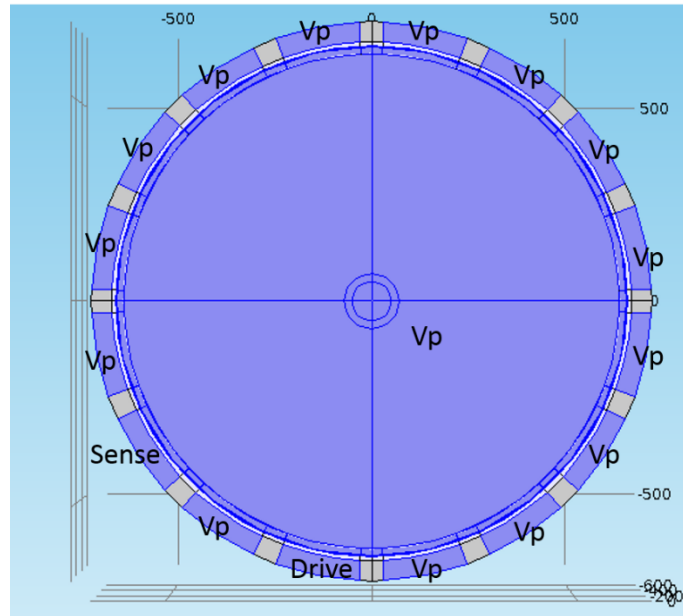


Figure 5.9: Electrode configuration for frequency domain simulation

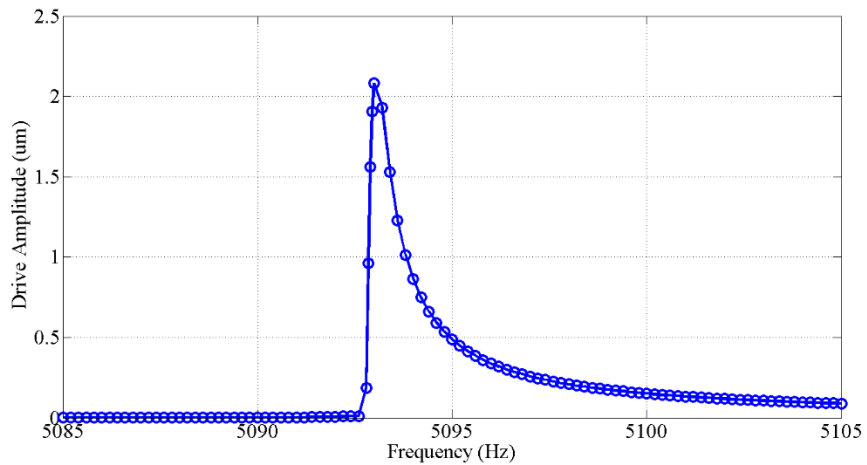


Figure 5.10: Simulated resonance peak by frequency sweeping

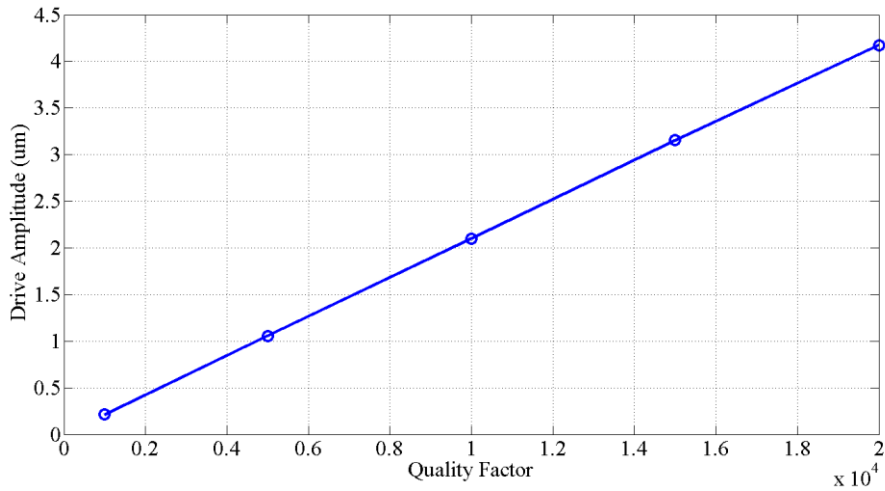


Figure 5.11: Simulated drive amplitude Vs quality factor

As can be seen, the drive amplitude is a linear function of the drive mode quality factor and electrostatic force. The same electrostatic model is run for the simulation of drive amplitude. The electrode configuration is shown in figure 5.9. Hemispherical shell is polarized by a DC potential of V_p , a drive electrode is driving the resonator into resonance by a AC signal with grounded DC potential. A pre-stressed frequency domain analysis with AC perturbation of 30 mV is carried out to find out the drive amplitude. In order to precisely simulate the drive amplitude, a frequency sweeping is performed to locate the peak. Figure 5.9 shows a resonance peak with quality factor of 10,000, DC bias of 40 V. By keeping the DC and AC level the same, drive amplitude is simulated as a function of quality factor. Figure 5.11 shows the linear dependency of drive amplitude on quality factor. It also shows that, with a quality factor of even 10,000, the resonator is easily driven in non-linear region when the drive amplitude is larger than 1/10 of the capacitive gap. With the improvement on Q, gap size needs to be further optimized. Simulation results show that gap size of 50 μm is optimized for Q of 150,000, while gap size of 100 μm is optimized for Q of 1.2 millions. However, with the gap size of 100 μm , electrostatic frequency tuning effect will be greatly reduced. Simulation shows only 2.2 Hz can be tuned

by applying a DC bias of 100 V. This will require an ultra-axisymmetric structure with frequency mismatch of sub-Hz.

5.4 Sensitivity

While the hemispherical shell is driven into its first degenerate mode (drive mode), the vibration energy is stored in this mode and slowly decays if there is no rotation. Then rotation is applied, the Coriolis effect transfers the stored vibration energy between the two degenerate modes until all the energy is transferred to the second mode (sense mode). The Coriolis induced vibration will cause a capacitance change at the antinode of the sense mode, which is also the node of drive mode. By sensing the capacitance change, the angular rotation can be measured. The sense mode amplitude can be calculated by the following equation [30]:

$$y = 4xA_gQ_s \frac{\Omega_z}{\omega_0} \quad (5.12)$$

Where A_g is the angular gain, Q_s is the sense mode quality factor, Ω_z is the rotation rate, and ω_0 is the resonance angular frequency.

Angular gain is another critical parameter of a Coriolis vibratory gyroscope. When rotation is applied to the device, the node lines of the vibration pattern lag behind the rotation of the sensor. The angular gain is defined as the ratio of the change in the vibration pattern angle to the applied angle of rotation. It depends on the structure of the resonating structure as well as the resonance mode. Table 5.1 lists the reported value of angular gain for various axis-symmetric structures.

Table 5.1 Reported value to angular gain for various structures

	Ring [28]	Cylinder [32]	Disk [37]	Hemisphere [12]
A_g	0.37	0.013	0.23	0.3

In the same electromechanical model of μ HRG is used by applying a sense electrode that is 45° apart from the drive electrode as figure 5.9 shows. The rate sensitivity of μ HRG is simulated by applying a Coriolis body force on the hemispherical shell structure in the pre-stressed frequency domain simulation with AC perturbation. With the existence on z axis rotation only, the body force is written as:

$$\vec{F}_{Cor} = \begin{Bmatrix} -\rho\Omega_z v_y \\ \rho\Omega_z v_x \\ 0 \end{Bmatrix} \quad (5.13)$$

The μ HRG is biased at 40 VDC, and driven by an AC signal of 30 mV from one electrode. The Coriolis signal is detected from one electrode which is 45° apart from the drive electrode. With a quality factor of 10,000, a rate sensitivity of 400 pA/(deg/s) is predicted, showing a very sensitive gyroscope response.

CHAPTER 6

MONOLITHIC FABRICATION OF POLYSILICON μ HRG

In this chapter, the fabrication process of polysilicon micro-hemispherical resonating gyroscope is introduced, and detailed process module is presented. SEM images of fabricated devices are then demonstrated to show a successful fabrication process. A few optimization of the process is made in order to improve the yield and the performance of the device.

6.1 Fabrication Features

6.6.1 Structural Material

High quality factor can help increase sensitivity, decrease noise level and also reduce power consumption of a gyroscope. Materials that are potentially having high Q properties should be selected as the structural material of the hemispherical shell. According the thermal elastic damping simulation in section 2.2.1, silicon dioxide and polysilicon are showing the highest two Q_{TED} , which are more than a couple of millions.

The requirement of high axisymmetry expects the Young's Modulus of the structural material to be isotropic. Although single crystal material such as single crystal silicon could possibly give higher quality factor, they are actually not preferred due to their anisotropic properties. Silicon dioxide and polysilicon are both isotropic materials that are suitable for the structural material of μ HRG. The only advantage of silicon dioxide is that it is potentially giving higher Q_{TED} if the quality factor is TED-limited. However, the resonator characterization results of silicon dioxide μ HSR and polysilicon μ HSR does not show much difference, and both have not yet reached Q_{TED} . Since the quality factor is material-independent, polysilicon is selected as the structural material to eliminate the conductive coating that is needed for silicon dioxide.

6.6.2 3D HARPSS

HARPSS process is a single wafer, all-silicon, high aspect-ratio multi-layer polysilicon micromaching technology that combines deep dry etching of silicon with conventional surface micromaching to realize tens to hundreds of microns thick, high aspect-ratio, electrically isolated polysilicon structure with sub-micron air-gaps [29]. It is developed by Ayazi to fabricate polysilicon ring gyroscope (PRG) [28]. Later on, it is widely used in MEMS area for various devices, such as star gyroscopes [82], bulk acoustic wave disk gyroscopes [33], bulk acoustic wave resonators [83, 84]. The fabrication process of each device was developed based on the original HARPSS process, but with minor modifications considering the case of each device.

For μ HRG, a 3D HARPSS process is developed to create high aspect-ratio, electrically isolated polysilicon electrode structure, as well as hemispherical shell structure. The polysilicon electrodes structure is created by high aspect-ratio DRIE etching and trench refilling process. The three-dimensional hemispherical shell structure is created by the same process introduced on chapter 3. Compared to the original HARPSS, this 3D HARPSS creates a three-dimensional resonating structure, which forms extremely complicated surface topography and is difficult for any photolithography step afterwards.

6.6.3 Self-aligned Structures

Since the electrodes and hemispherical shell are defined in different steps in the process flow, there will be finite misalignment between different lithography steps which will cause misalignment between the electrodes and hemispherical shell. In other words, the hemispherical shell will not be at the center of the electrodes, and will create imbalanced pre-stress of the hemispherical shell structure. This problem is solved by designing a process that can make self-aligned electrodes and hemispherical shell structure.

The first mask defines the trenches for electrodes and the circular opening for the hemispherical shell at the center of the electrodes. The precision of alignment between these two features is solely dependent on the precision of mask manufacturing, which can go down below 0.5 μm . During the etching of high aspect-ratio silicon trenches, the circular opening for hemispherical shell is protected by photoresist that defined in the second mask. After refilling the trenches with dielectric insulation layer and polysilicon, the electrodes are protected by photoresist that defined in the other mask during isotropic etching process. In this way, electrode structure and hemispherical shell structure can be self-aligned by the additional mask.

6.6.4 Scalable Capacitive Gap

The mechanical noise of a Coriolis Vibratory Gyroscope (CVG) is inversely proportional to the drive amplitude of the drive mode [37]. For navigation grade high performance gyroscopes, a few microns' drive amplitude is usually required [85]. In order to have the capacitive transducer working in its linear range, gap size needs to be larger than 10 times of the drive amplitude. In the electro-mechanical model introduced in chapter 5, it is proved that for this type of low frequency, low stiffness, high Q devices, even capacitive gap of 20 μm or above is able to actuate as well as tune the device without increasing DC bias more than 50 V.

The original HARPSS process defines the capacitive air gap by the thickness of a sacrificial layer which is always sub-micron in thickness. The sacrificial layer limits the maximum gap size the process can produce. This new process also gives a tunable capacitive gap size that is not dependent on the thickness of sacrificial material. The capacitive gap size in this process is defined by precision timing of isotropic etch. The gap size is able to go from 5 μm to 50 μm or even larger, which is desired for low frequency, low stiffness, high Q devices.

6.6.5 DC Bias

For capacitive devices, a DC bias (polarization voltage) needs to be provided to the resonating structure. Because the hemispherical shell is very fragile and cannot survive the wire-bonding process, two methods of providing DC bias to the hemispherical shell is developed. One of them is to etch a through hole from the backside of the wafer, then structural polysilicon is deposited by LPCVD through the hole to the backside. The DC bias is provided by the backside of the wafer. The second approach is to etch the sacrificial oxide layer at the center bottom of the hemispherical mold before depositing structural polysilicon layer, which will be connected directly with silicon substrate for DC bias. Batches for both process are fabricated and characterized.

6.2 Microfabrication Process Flow

The process starts with a heavily doped (111) silicon substrate (Non-SOI) with Boron as the dopant and doping level of 10-20 mΩ•cm. Silicon dioxide is firstly thermally grown on both side of the wafer to reach the thickness of 6 μm. This oxide will be used later on for both silicon DRIE trench etching and silicon isotropic etching for hemispherical mold. The first lithography is then performed including the feature of electrode trench and circular opening for isotropic etching. Shipley positive tone photoresist SPR220-7.0 with thickness of 7 μm is used as the photoresist of this step. Then the first oxide is etched in Plasma-therm ICP by C₄F₈ plasma to create the electrode trenches and circular opening (figure 6.1a). The second lithography is performed to protect the circular opening in silicon DRIE etching. Futurrex negative tone photoresist NR9-3000P with thickness of 16 μm is used in this step. DRIE etching in STS-Pegasus is performed to create high aspect-ratio deep trenches for electrode structure. The trenches are designed to be 8 μm in width and etched to be 300 μm in depth with the aspect-ratio close to 1:40. Figure 6.2 demonstrates the cross-section view of these high aspect-ratio trenches in silicon.

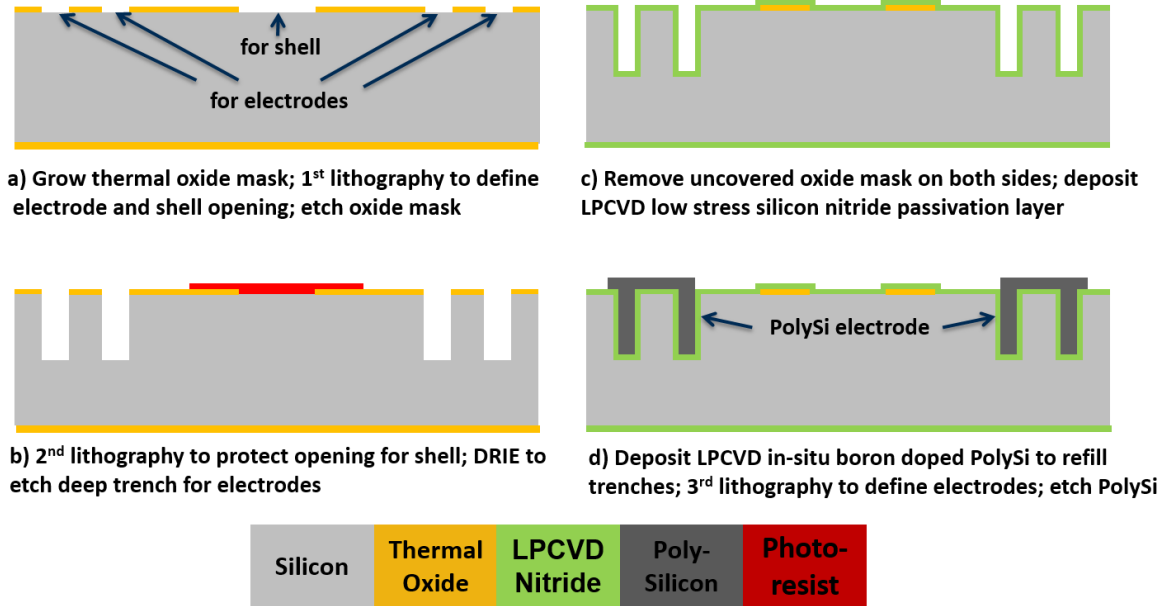


Figure 6.1: Microfabrication process flow of polysilicon μ HRG: Step a) to d)

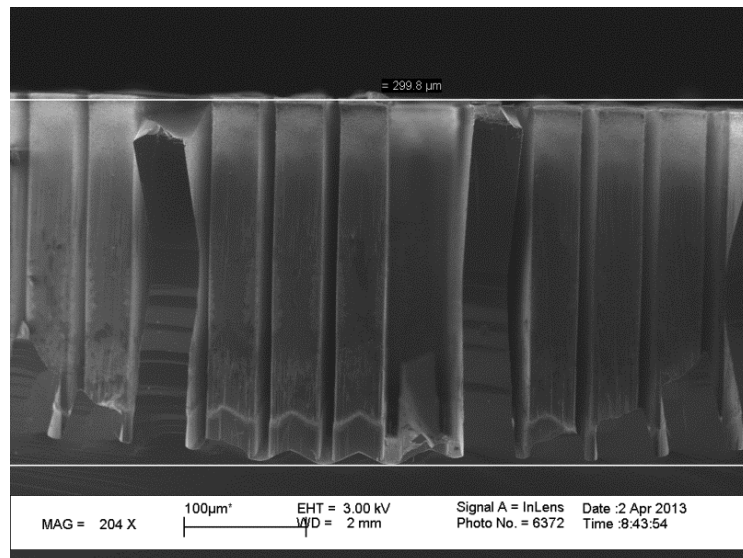


Figure 6.2: High aspect-ratio trenches in silicon

Without removing the remaining photoresist, the exposed first oxide mask on both sides is removed by Plasma-therm ICP, leaving the oxide for circular opening in the center. LPCVD silicon nitride is then deposited as the passivation layer to insulate electrodes and silicon substrate as figure 6.1c shows. LPCVD in-situ boron doped polysilicon is deposited at 588°C to refill the trenches and form the electrode structure. After that, the third

lithography is performed the separate each electrode and define the bonding pad. Shipley positive tone photoresist SC1827 with thickness of 3 μm is used in this step. A short DRIE silicon etch in STS-ICP is then to etch away the exposed polysilicon as figure 6.1d shows. Figure 6.3 shows the SEM image of the cross section view of a refilled trench. The layers of polysilicon and silicon nitride is clearly seen.

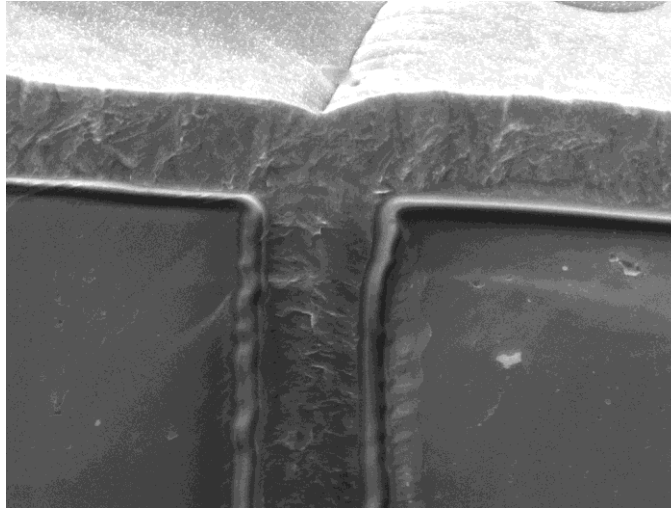


Figure 6.3: Silicon nitride and polysilicon refilled trench

The fourth lithography step is to remove silicon nitride from center region as figure 6.4e shows. Due to the topography on the surface created by polysilicon etching, a thick photoresist of AZ4620 is used for thickness of 10 μm . Silicon nitride is etched in Vision RIE by CHF_3 plasma. The fifth lithography is to protect the polysilicon electrodes and the silicon substrate, leaving only the circular opening for isotropic etching exposed. The radius of the circular opening in this mask is designed to be 20 μm larger than the one on the first mask, leaving enough clearance compensating for misalignment. Therefore, the actual circular opening for isotropic etching is defined by the first mask for the self-alignment of polysilicon electrodes and hemispherical shell.

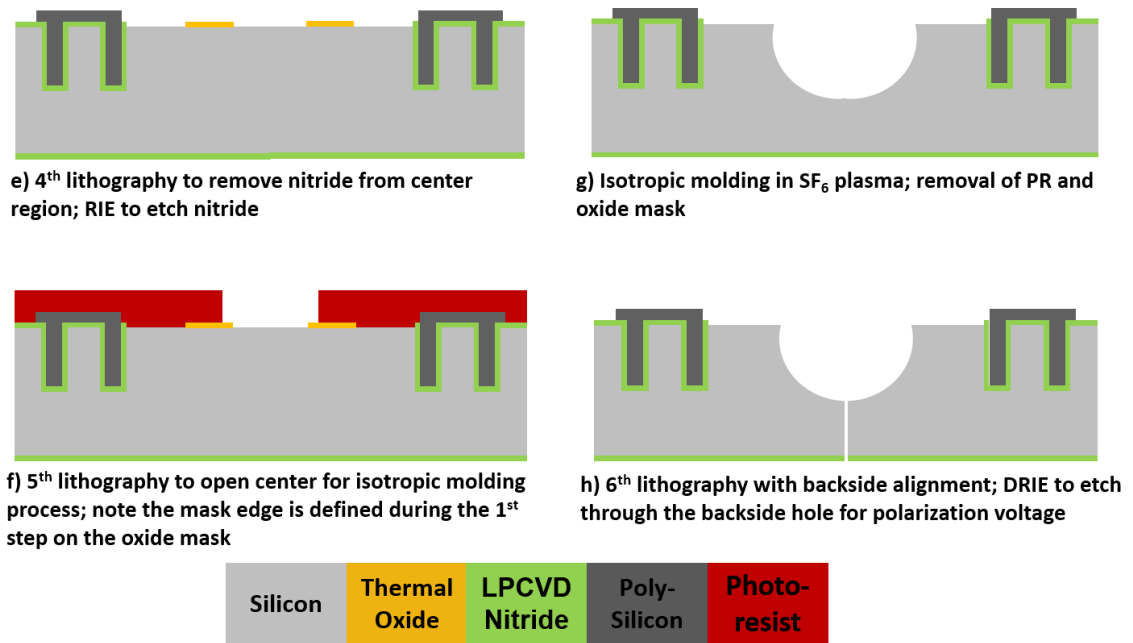


Figure 6.4: Microfabrication process flow of polysilicon μ HRG: Step e) to h)

Isotropic etching is then performed in SF₆ plasma the same way as introduced in Chapter 3. In order to have the capacitive gap as designed, a very good timing is needed. Due to the effect of reentrant caused by ICP etching, IR microscope is used to check the closest gap size which is not on the surface of silicon substrate. Etching is considered to be completed when the closest gap reaches 20 μ m. Figure 6.4g illustrates the structure after removing photoresist mask in hot piranha and oxide mask in HF solution. The sixth lithography creates a circle with diameter of 40 μ m right at the center of the hemispherical mold on the backside of the wafer. This step requires a backside to front side alignment, after which silicon DRIE is then performed to etch through the wafer. Figure 6.5 shows the SEM image of a hemispherical mold with self-aligned polysilicon electrodes around it and a through hole in its center. Figure 6.6 shows the zoomed-in view of the center through hole from the front side of the wafer. It shows 40 μ m in diameter which is exactly the designed size, proving very good process control of DRIE with minimum footing effect.

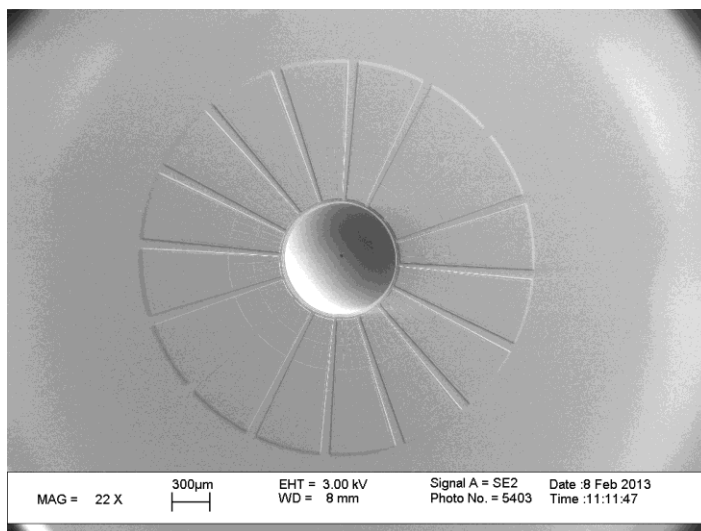


Figure 6.5: Hemispherical mold with polysilicon electrodes and backside hole

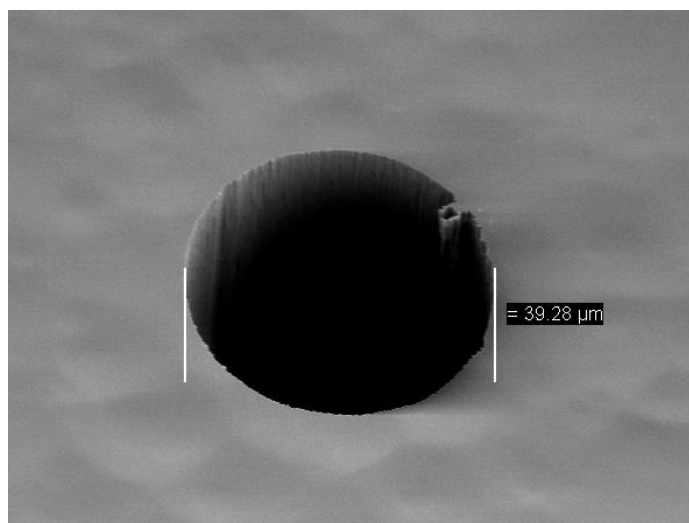


Figure 6.6: Through hole viewed from front side for DC bias

After that, 2 μm sacrificial silicon dioxide is thermally grown, followed by LPCVD polysilicon deposition for hemispherical shell structure. For better surface roughness and smaller crystalline size, undoped polysilicon is deposited at 588°C and then doped and annealed at 1050°C . Figure 6.8 shows the surface topography of in-situ boron doped polysilicon and undoped polysilicon measured by atomic force microscopy (AFM). The in-situ boron doped polysilicon has the surface roughness R_a of 10 nm with maximum crystal size 200 nm, while the undoped polysilicon has the surface roughness R_a of 1 nm

with maximum crystal size 10 nm. Therefore, undoped polysilicon is selected for the structural material for hemispherical shell. To remove polysilicon deposited on the top surface, photoresist Shipley SC1813 is spun at 400 rpm to fill the hemispherical mold. A blank etch in O₂ plasma will etch away photoresist on the top surface while keeping the photoresist in the hemispherical mold. With polysilicon in the hemispherical mold being protected, SF₆ plasma is used to remove the polysilicon on the top surface.

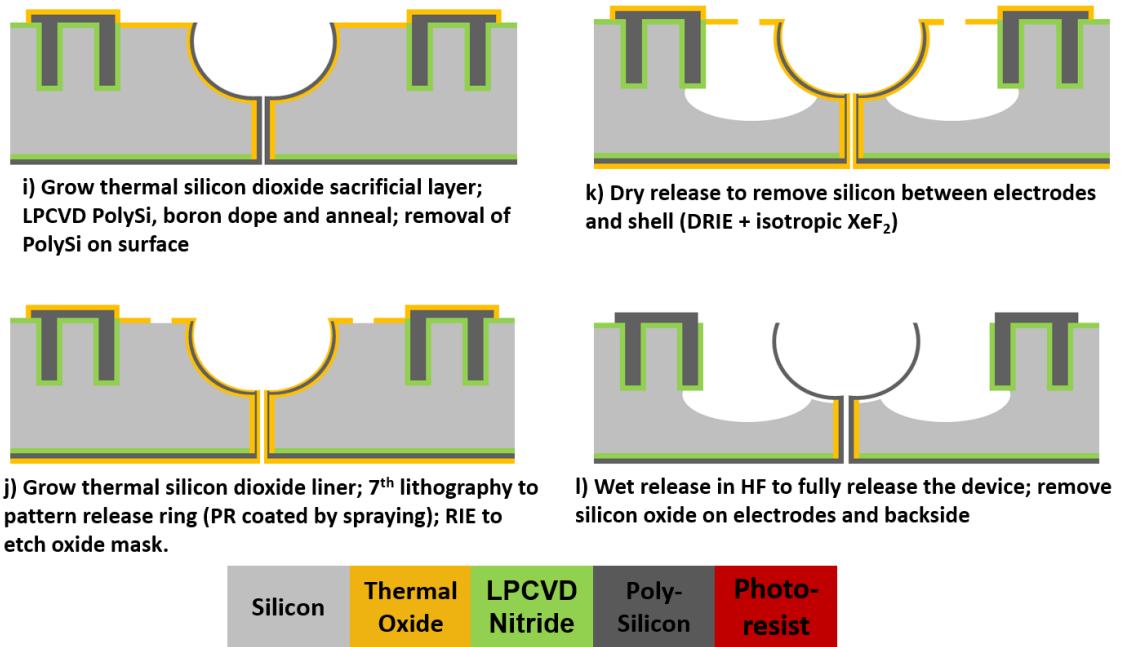


Figure 6.7: Microfabrication process flow of polysilicon μ HRG: Step i) to l)

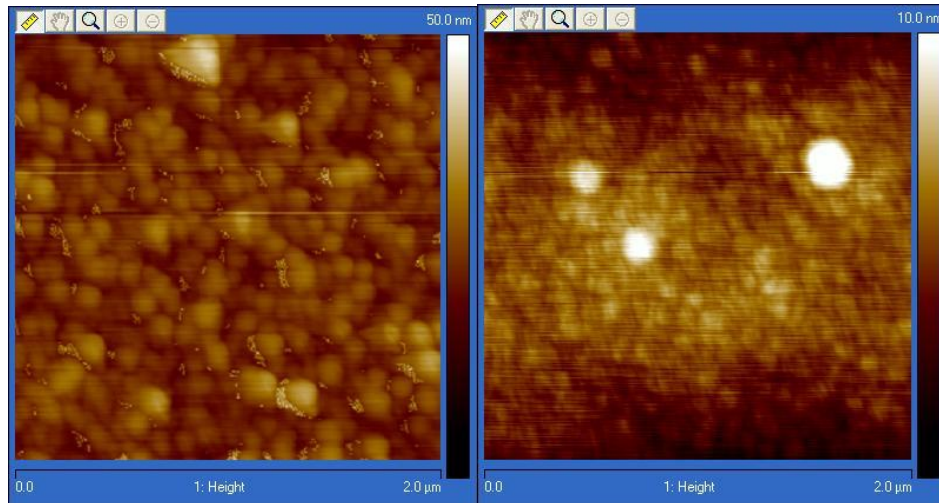


Figure 6.8: AFM surface topography measurement of (left) in-situ boron doped polysilicon and (right) undoped polysilicon

Another silicon dioxide layer is thermally grown on order to protect polysilicon from the other side and fine tune the thickness of structural layer. The last lithography step is then performed by patterning spraycoated 10 μm AZ4620 photoresist due to the complex surface topography in the front side. The oxide is then etched to expose the release ring structure as shown in figure 6.7j. In the device releasing procedure, DRIE dry release is firstly performed, followed by isotropic silicon etching in SF_6 plasma and XeF_2 gas as shown in figure 6.7k. This step is to clear out the silicon between the hemispherical shell and electrodes. The DRIE dry release is to reduce the amount of isotropic etching, thus reduce the undercut to the electrode structure. The last step is to remove the silicon dioxide on the surface of polysilicon and fully release the device (figure 6.7l). Since this is a low frequency, low stiffness device, super critical drying is needed to dry these released devices.

6.3 Fabrication Results

In this section, the images of fabricated μHRG at various views are demonstrated, showing the 3D structure as designed in the process flow. Figure 6.9 shows a picture of a wafer with processed polysilicon μHRG that is ready for dicing and release. Figure 6.10

shows a fabricated polysilicon μ HRG with 16 self-aligned polysilicon electrodes and through hole for DC bias. Figure 6.10 shows a cross section view of polysilicon μ HRG with the hemispherical shell remains. In order to further looking at the electrode structure, the hemispherical shell is removed manually. Figure 6.11 shows a cross section view of polysilicon μ HRG with the hemispherical shell off. The tall electrodes and undercut can be easily seen. Figure 6.12 shows the zoomed-in view of hemispherical shell. The gap between hemispherical shell and silicon substrate is the released sacrificial silicon dioxide.

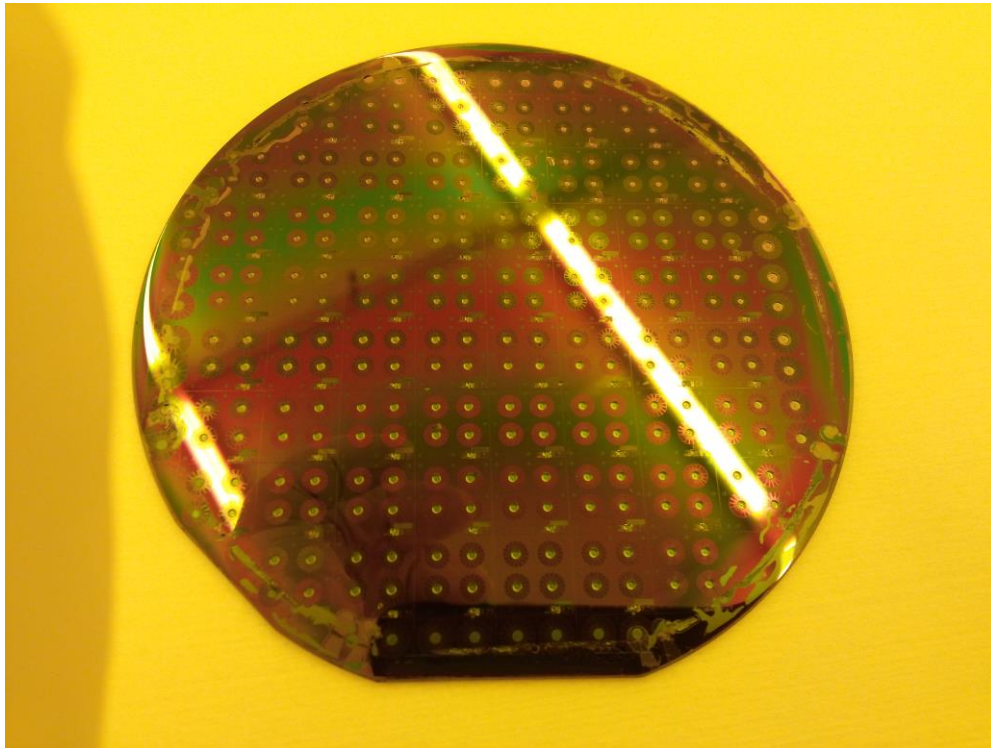


Figure 6.9: Wafer level fabrication of polysilicon μ HRG

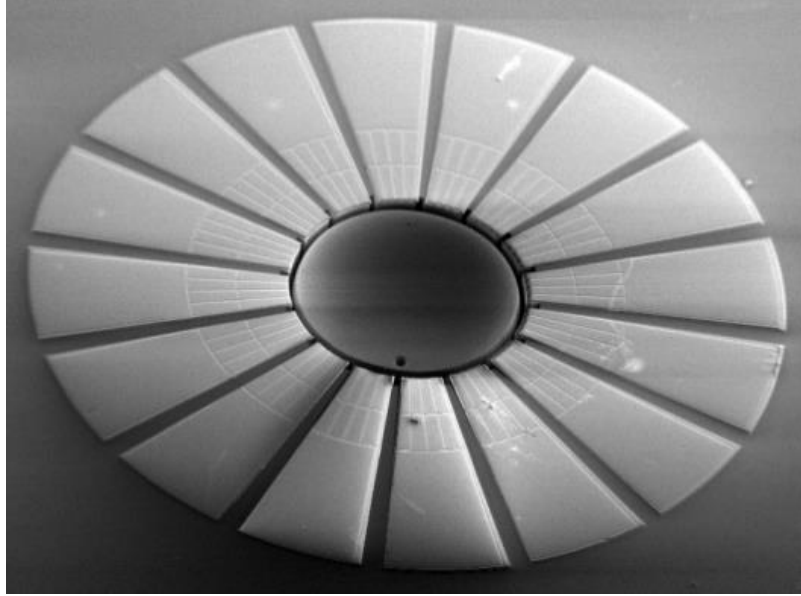


Figure 6.10: Bird eye view of a fabricated polysilicon μ HRG

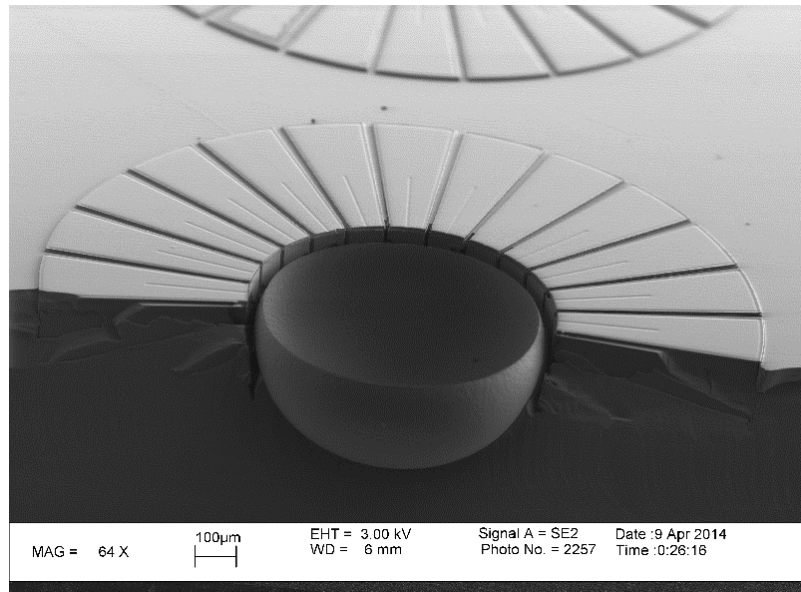


Figure 6.11: Cross section view of a fabricated polysilicon μ HRG (with shell on)

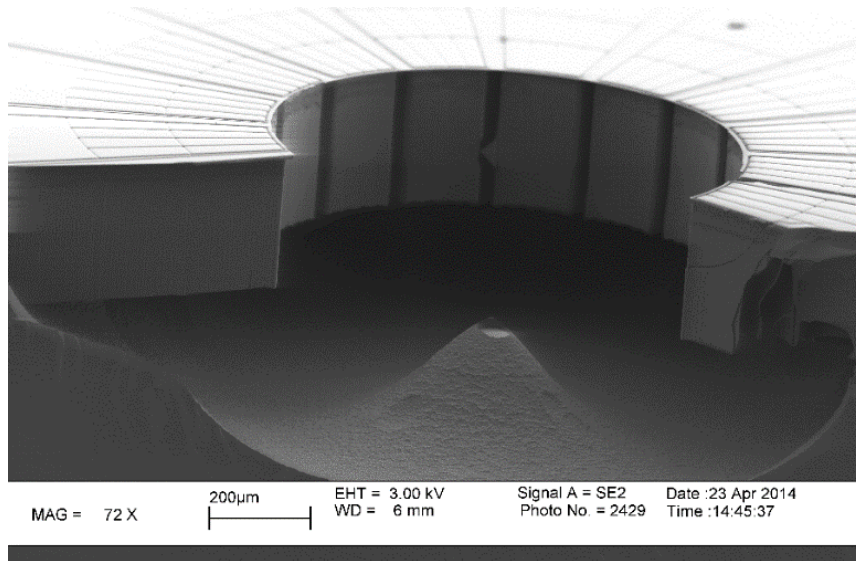


Figure 6.12: Cross section view of a fabricated polysilicon μ HRG (with shell off)

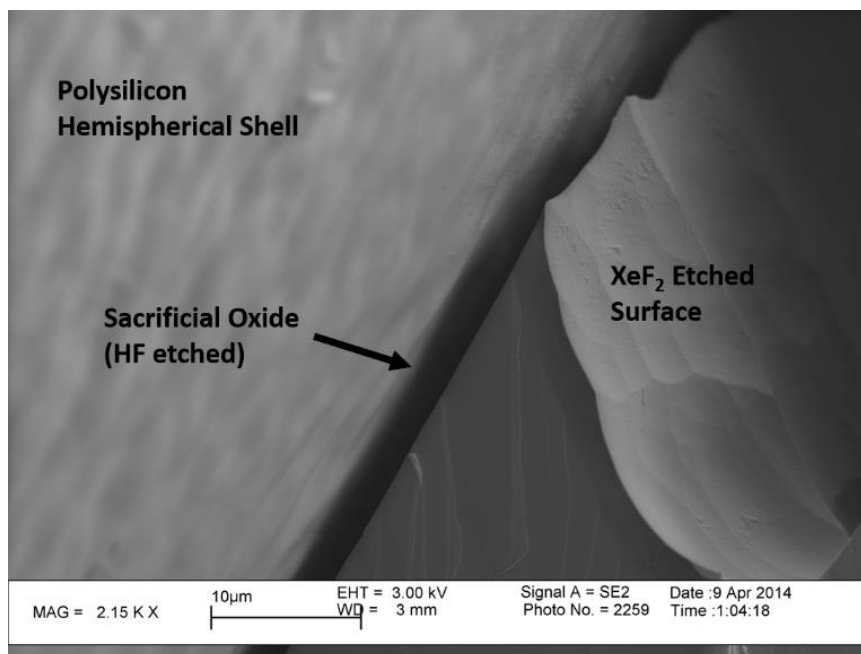


Figure 6.13: Zoomed-in view of a fabricated polysilicon μ HRG

6.4. Front Side DC Bias Contact

The process flow introduced in the previous section has already demonstrated successful fabrication of μ HRG structure. However, the existence of through hole is sometimes causing various problems during fabrication. The through hole will result in

incomplete coverage of hemispherical mold during mold filling by photoresist, causing part of the structural polysilicon get etched. The backside through etch is also needed to be strictly controlled to avoid footing of DRIE, which will cause the through hole to be larger from the front side. Another process flow which includes a front side DC bias contact is developed based on the previous process with minor modifications. This process eliminates the backside alignment and through hole by a front side pattern of spraycoated photoresist.

The first 2/3 of the process is exactly the same as introduced before. The modification begins after isotropic etching of hemispherical mold (figure 6.13g). After growing sacrificial oxide layer, photoresist AZ 4620 is spraycoated on the substrate and a circle is patterned right at the center of the hemispherical shell. Due to the non-contact type of lithography, the pattern will be larger than the size on the mask and this can be compensated by designing a smaller circle. Moreover, over-exposure is needed for the larger actual exposed area. After photoresist development, the exposed sacrificial oxide is etched and the silicon underneath is also etched by DRIE as figure 6.13h shows. Polysilicon structural layer is then deposited, doped and annealed. The rest of the process flow remains the same as the previous process. The final structure is shown in figure 6.13j. Figure 6.14 demonstrates the SEM of a fabricated polysilicon μ HRG with front side DC bias contact. The zoomed-in view of the contact is shown in figure 6.15.

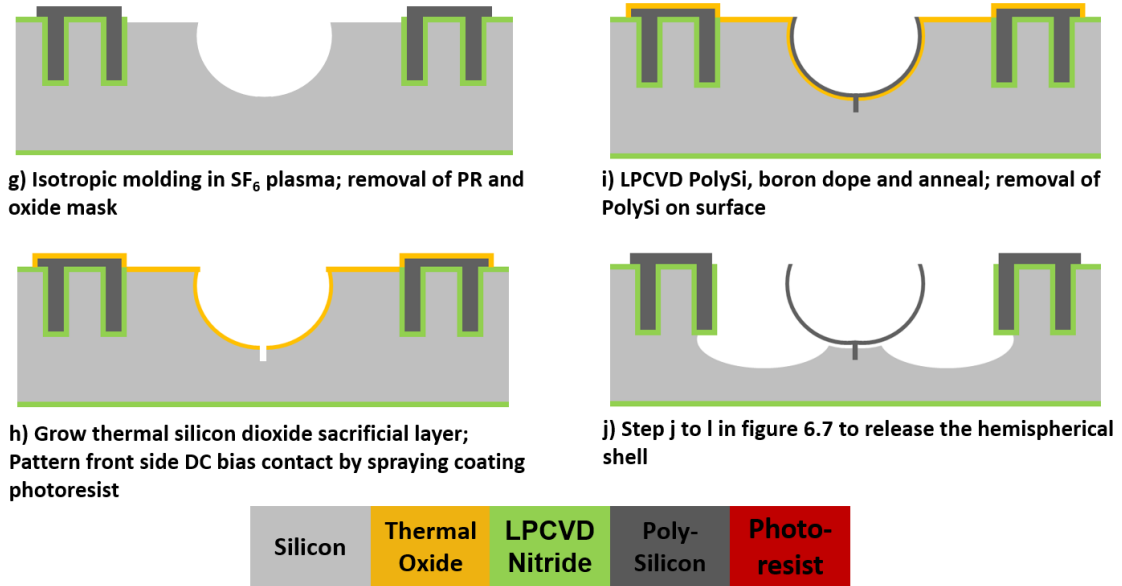


Figure 6.14: Modified process flow for front side DC bias contact

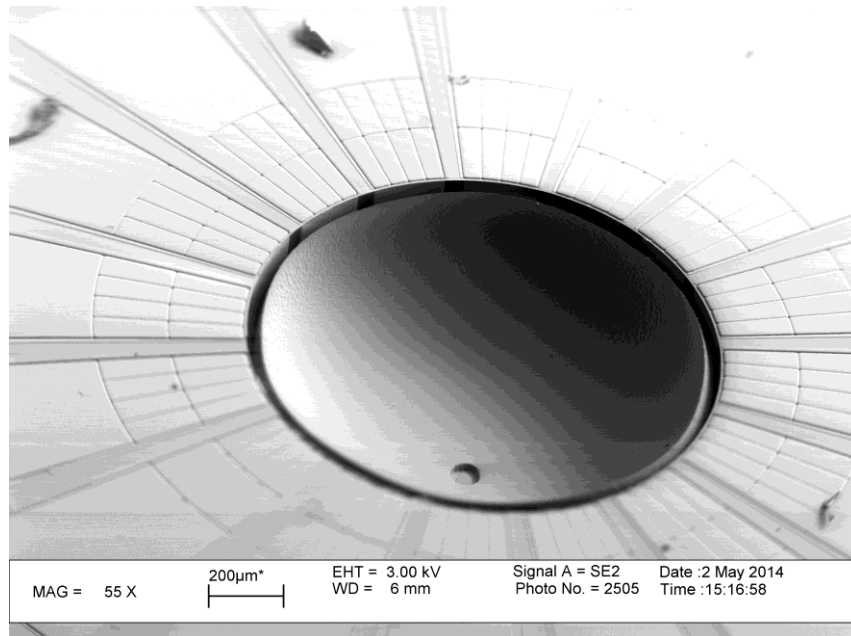


Figure 6.15: Fabricated polysilicon μ HRG with front side DC bias contact

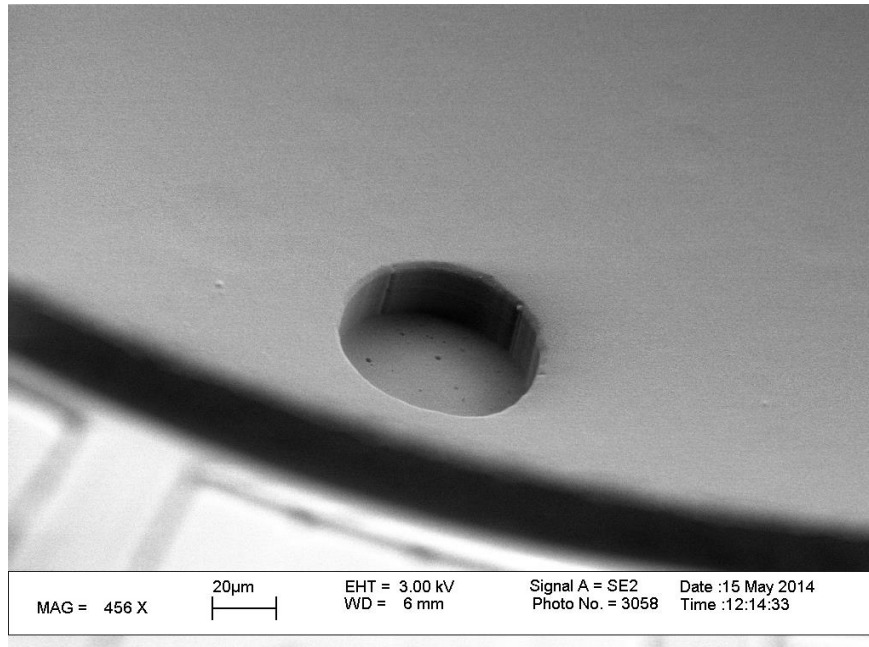


Figure 6.16: Zoomed-in view on the front side DC bias contact

6.5 Detailed Process Modules

All the steps of the process flows introduced in previous sections are done at Georgia Tech IEN cleanroom facilities. Detailed process modules are discussed in this section and processing parameters are given.

6.5.1 Silicon Dioxide Etching

Silicon dioxide is a good etching mask for silicon etching in SF_6 plasma (DRIE, isotropic etching) and XeF_2 gas. Oxide etching is carried out in Plasma-therm ICP tool in IEN cleanroom. The detailed parameters are listed in Table 6.1. Due to the high power of this tool, it gives a very fast etch and the photoresist mask needs to be hard-baked at 120°C for 10 minutes. However, this hard-baking could cause photoresist to reflow, and distort the feature. For oxide etching with minimum feature size smaller than $20\ \mu\text{m}$, Vision RIE is used for oxide etching at lower power without the need for photoresist hard-baking. Table 6.2 lists the parameters of oxide etching recipe in Vision RIE.

Table 6.1: Parameters of oxide etch recipe in Plasma-therm ICP

Parameters	Value
Gas Flow Rate	C ₄ F ₈ : 15 sccm
	Ar: 5 sccm
	CO ₂ : 28 sccm
Pressure	5 mTorr
Platen Power	40 W
Coil Power	800 W
Platen Temperature	25°C
Etch Rate	180 nm / min

Table 6.2: Parameters of oxide etch recipe in Vision RIE

Parameters	Value
Gas Flow Rate	CHF ₃ : 45 sccm
	O ₂ : 5 sccm
Pressure	40 mTorr
Platen Power	250 W
Etch Rate	25 nm / min

6.5.2 Silicon DRIE

Silicon DRIE trench etching is a very important process for this 3D HARPSS process. As introduced, the trenches for polysilicon electrodes are designed to be 8 μm in width and etched 300 μm in depth, with the aspect-ratio close to 1:40. In IEN cleanroom, STS-Pegasus is the silicon DRIE tool that can reach the highest aspect ratio. It can perform parameter ramping, which enable the high aspect-ratio etching. Table 6.3 lists the

parameters of high aspect-ratio DRIE recipe. Several parameters such as etch time and etch power are ramping either up or down during the etching process.

Table 6.3: Parameters of silicon DRIE in STS-Pegasus

Parameters	Start	Finish
Etching Time	2.4 s	3 s
Passivation Time	2 s	2 s
Etching Gas Flow	SF ₆ : 250 sccm	SF ₆ : 250 sccm
Passivation Gas Flow	C ₄ F ₈ : 150 sccm	C ₄ F ₈ : 150 sccm
Etching Power	Coil: 2200 W; Platen: 90 W	Coil: 2000 W; Platen: 90 W
Passivation Power	1900 W	1900 W
Etching Cycles	1200	
Platen Temperature	0°C	

6.5.3 Silicon Isotropic Etching

Hemispherical mold is etched by silicon isotropic etching in SF₆ plasma. It is carried out in either STS-ICP tool or STS-HRM tool at Georgia Tech IEN cleanroom. STS-HRM is generating more power than STS-ICP, thus provides a faster etching but rougher surface quality. Table 6.4 and 6.5 list the etching parameter in STS-ICP and STS-HRM, respectively.

Table 6.4: Parameters of silicon isotropic etching in STS-ICP

Parameters	Value
Gas Flow	SF ₆ : 130 sccm
	O ₂ : 13 sccm
Coil Power	600 W
Platen Power	10 W
Platen Temperature	20°C

Table 6.5: Parameters of silicon isotropic etching in STS-HRM

Parameters	Value
Gas Flow	SF ₆ : 260 sccm
Coil Power	2000 W
Platen Power	30 W
Platen Temperature	10°C

6.5.4 Polysilicon Deposition

In this process, LPCVD polysilicon by Tystar polysilicon furnace is used for the electrodes structure and the hemispherical shell structure. In both structures, doping is needed for electrical conductivity. In-situ boron doped polysilicon has a faster deposition rate and eliminates the doping and annealing step afterwards. Undoped polysilicon has a slower deposition rate but smaller crystalline size, thus better smoothness. Table 6.6 and table 6.7 lists the processing parameter for undoped and in-situ boron doped polysilicon, respectively.

Table 6.6: Parameters of LPCVD undoped polysilicon in Tystar Furnace

Parameters	Value
Deposition Temperature	588°C
Gas Flow	SiH ₄ : 100 sccm
Deposition Pressure	250 mTorr
Deposition Rate	319.7 nm/hr

Table 6.7: Parameters of LPCVD in-situ boron doped polysilicon in Tystar Furnace

Parameters	Value
Deposition Temperature	588°C
Gas Flow	SiH ₄ : 100 sccm BCl ₃ : 30 sccm
Deposition Pressure	250 mTorr
Deposition Rate	453.5 nm/hr

CHAPTER 7

TEST AND CHARACTERIZATION OF POLYSILICON μ HRG

This chapter presents the characterization results of μ HRG fabricated using the process described in chapter 6. Firstly, interface electronics for gyroscope operation is introduced. Then, frequency response of the resonator is measured, and mode matching is performed. The mode-matched gyroscope sensitivity is then measured in an open loop configuration, showing good sensitivity and the potential of high performance gyroscope.

7.1 Front-end Electronics

The front-end electronics for interfacing μ HRG is designed collaborately by Northrop Grumman and Georgia Tech. As figure 7.1 shows, it includes circuitry for antinode/node forcer, antinode/node pickoff, feed-through cancellation and quadrature control. Each channel is buffered with a different operational amplifier. Moreover, an on-board mini vacuum chamber is incorporated onto the PCB. Copper is deposited onto the area where device will be mounted at, in order for vacuum sealing. Another adaptor board is also designed for easier access of all functionalities (figure7.2). The interface PCB and the adaptor board are connected by pin header



Figure 7.1: Layout of interface PCB

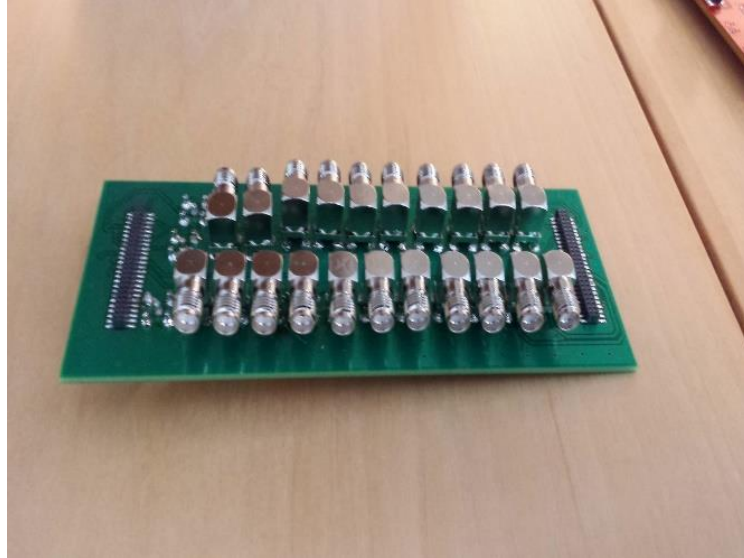


Figure 7.2: Image of the adaptor board

Fabricated μ HRG is wire-bonded onto the interface PCB as figure 7.3 shows. For stability consideration, none of the electrodes are left floating. This also shows the mechanical robustness of the polysilicon electrodes. Finally, the interface PCB with device on is assembled with the adaptor board as figure 7.4 shows.



Figure 7.3: A polysilicon μ HRG with all 16 electrodes bonded to the interface PCB

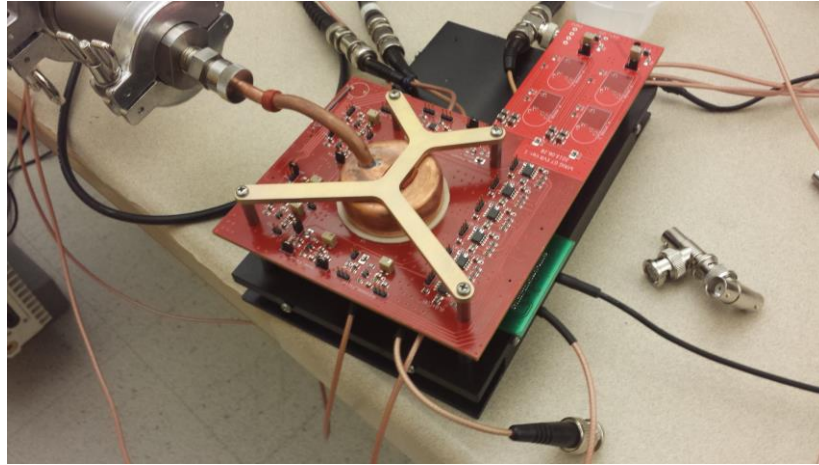


Figure 7.4: Assembled interface PCB (with device in on-board vacuum chamber) and adaptor board

7.2 Frequency Response

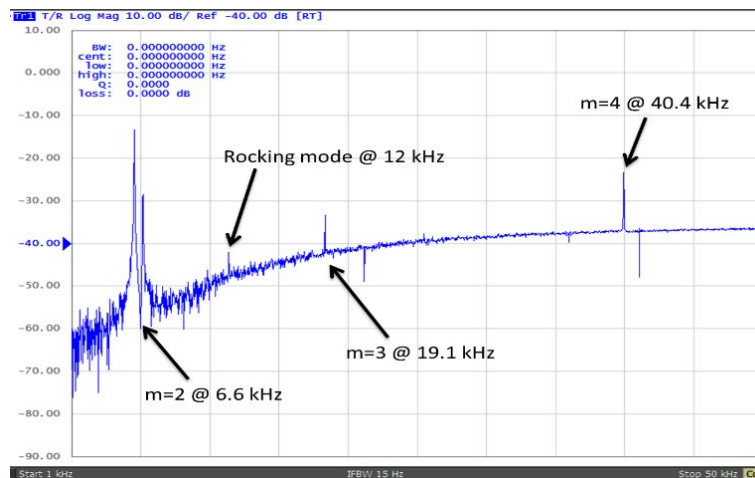


Figure 7.5: Frequency response of μ HRG showing various resonance modes

Resonator performance is characterized using a network analyzer (E5061B) while the board is placed inside a vacuum chamber with ~ 5 μ Torr vacuum pressure. Figure 7.5 shows the resonance peaks of the $m=2$, $m=3$, $m=4$ elliptical modes, and the rocking mode for a polysilicon μ HRG with a shell thickness of 700 nm and a shell diameter of 1240 μ m. The $m=2$, $m=3$ and $m=4$ resonances are measured to be at 6.7 kHz, 19.1 kHz and 40.2 kHz with quality factor 8,500, 7,000, and 10,400, respectively. Figure 7.6 shows the peak of one of the $m=2$ resonance peak, with quality factor of 8,500.

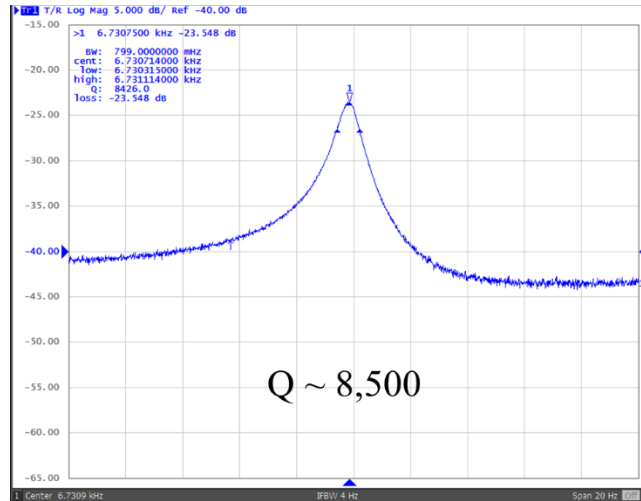


Figure 7.6: m=2 Resonance mode of μ HRG

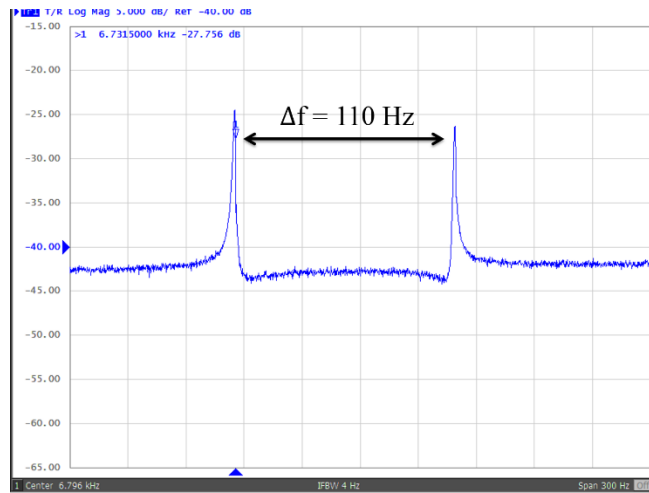


Figure 7.7: Frequency mismatch between two degenerate modes at 10 V DC

Figure 7.7 captures both m=2 degenerate modes at the same screen with the minimum possible DC bias voltage. It shows at 10 V DC bias, the two modes has a frequency mismatch of 110 Hz. Figure 7.8 shows the electrostatic tuning curve of two degenerate m=2 modes. Polarization voltage is applied on the hemispherical shell from 10V to 50V, and resonance frequency is recorded for both modes. The quadratic trend of the curve demonstrates very good agreement with the theory and simulation. By quadratic curve fitting, the as-fabricated frequency mismatch without any tuning effect is estimated to be 105 Hz with $\Delta f/f = 1.56\%$.

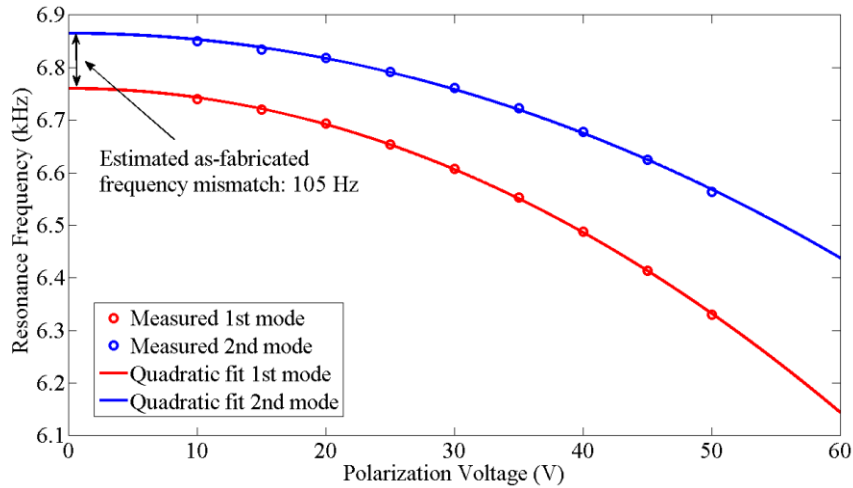


Figure 7.8: Electrostatic tuning curve of $m=2$ resonance modes

Due to the extremely small stiffness of this structure ($\sim 1\text{N/m}$), the drive amplitude can be as high as a few micrometers even with large capacitive gaps of $20\ \mu\text{m}$ as predicted by the simulation. During frequency sweeping by network analyzer, nonlinearity of resonance peaks can be easily observed if input RF power exceeds $-20\ \text{dBm}$. This phenomenon is confirmed by COMSOL multi-physics simulation that it is due to the nonlinearity of the transducer for its large drive amplitude.

7.3 Mode Matching Procedure

Mode matching and balancing of two degenerate $m=2$ modes is performed on the same polysilicon μHRG measured in the previous section, using the approach described in [81]. As figure 7.9 shows, two sets of tuning electrodes (V_{T1} , V_{T2}) and two sets of balancing electrodes (V_{Q1} , V_{Q2}) are used. Tuning electrodes for the drive mode and sense mode are at the anti-nodes of both the drive mode and sense mode, respectively. V_{T1} is to tune the drive mode, while V_{T2} is to tune the sense mode. However, the two modes will not perfectly matched by the tuning voltages only. When the two modes get very close ($\Delta f < 10\ \text{Hz}$), they will flip with each other suddenly due to the off-diagonal term of stiffness matrix caused by the quadrature signal [81]. This quadrature signal is eliminated by balancing and

aligning the resonance modes with their principal axes by electrodes that are at 22.5° to the drive anti-nodes and its equivalent position. Figure 7.10 shows the two peaks as their being matched with 27 Hz and 5 Hz frequency split, and figure 7.11 shows the mode matched resonance peak at 6.5 kHz with an effective quality factor of 11,100. The phase plot demonstrates 360° shift, proving the existence of two overlapped resonance peaks.

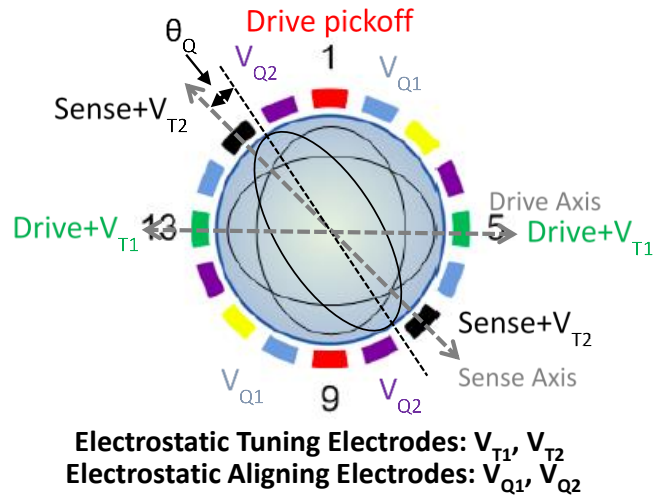


Figure 7.9: Schematic illustration of the tuning electrodes

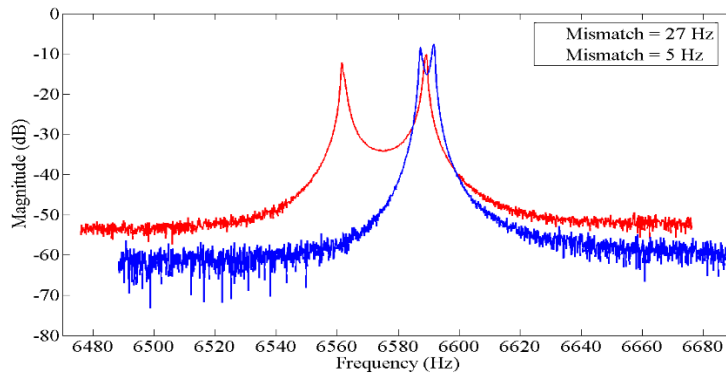


Figure 7.10: The two peaks as their being matched with a 27 Hz and 5 Hz frequency mismatch

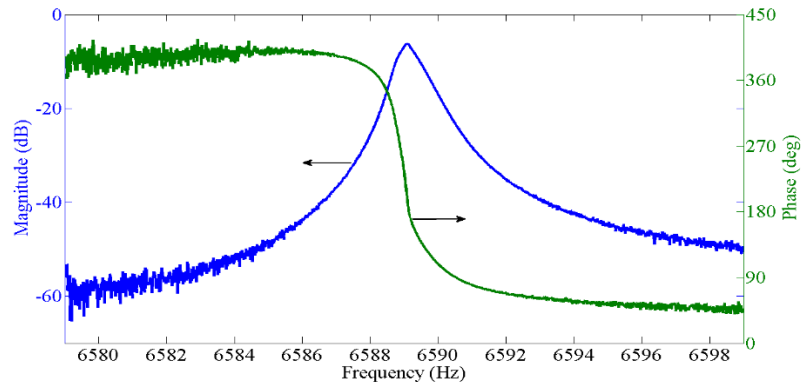


Figure 7.11: Schematic illustration of mode matching of μ HRG at 6.6 kHz

7.3 Rate Sensitivity

The rate sensitivity testing of mode-matched polysilicon μ HRG is carried out by the testing setup shown in figure 7.12. The μ HRG is mounted inside a vacuum chamber connect with a pump by long tube, allowing rotation of the vacuum chamber. The vacuum chamber sits on the rate table that provide a sinusoidal rotation motion that can be programmed. By specifying the rotation angle and frequency of the sinusoidal function, the rotation rate can be applied.



Figure 7.12: Testing setup for rate sensitivity

The mode-matched polysilicon μ HRG is operated in an open loop configuration as shown in figure 7.13 by exciting the drive mode using an external sinusoidal signal at the exact resonance frequency and an RF power of -35 dBm. The device is polarized at 40V. The Coriolis-induced signal is then processed by a transimpedance amplifier (TIA) with a gain of 500 k Ω and post amplification of 60 dB. After demodulation with the drive signal and low-pass filtering, the rotation rate information can be detected. The rate table is programmed to run at 200 mHz with an incremental rotation amplitude for different rotation rates. Figure 7.14 demonstrates the transient response to a 14 $^\circ$ /s rotation rate measured using an oscilloscope. It shows a very clean and linear sinusoidal output. Sensitivity is also measured by applying a rotation rate of up to 16 $^\circ$ /s. By linear regression, the scale factor of the polysilicon μ HRG is extracted to be 4.4 mV/($^\circ$ /s).

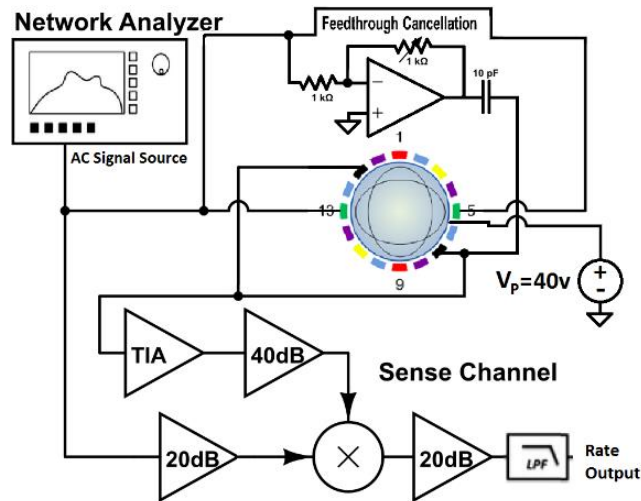


Figure 7.13: Rate sensitivity measurement circuit architecture

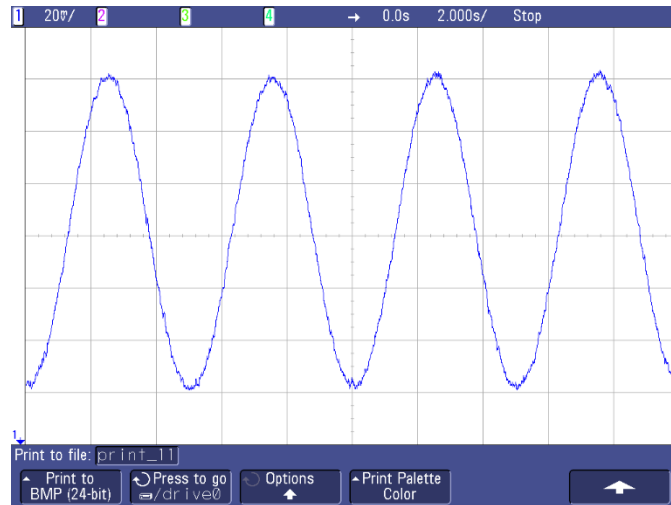


Figure 7.14: Transient response to a sinusoidal rotation input

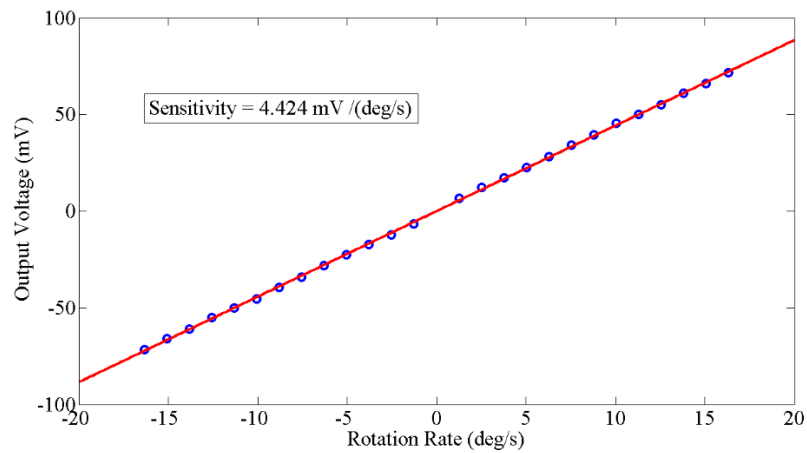


Figure 7.15: Scale factor of a mode matched polysilicon μ HRG

7.4 Discussion

A few batches of polysilicon μ HRG is fabricated, for both backside DC contact design and front side DC contact design. The quality factor of $m=2$ lies between 6,000 and 20,000. However, higher order modes ($m=3$, $m=4$) usually shows higher quality factor. Figure 7.16 shows the quality factor of $m=2$, $m=3$ and $m=4$ of one of the design with front side DC contact. It shows $m=2$ mode at 5.58 kHz with Q of 17,600, $m=3$ mode at 18.4 kHz with Q of 79,000 and $m=4$ mode at 32.7 kHz with Q of 61,000. This provides an indication

that the Q is support loss limited. The reason is that for higher order modes, the motion and support are better decoupled than $m=2$ mode. In other word, the motion of higher order mode is concentrating more at the rim of the hemispherical shell.

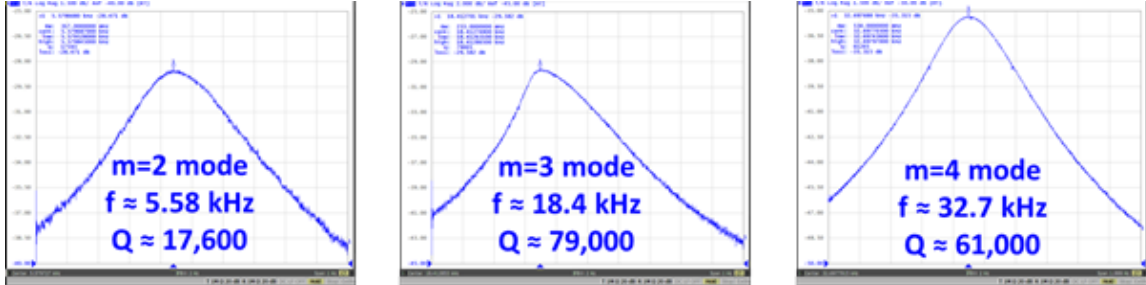


Figure 7.16: Quality factor of different modes of polysilicon μ HRG

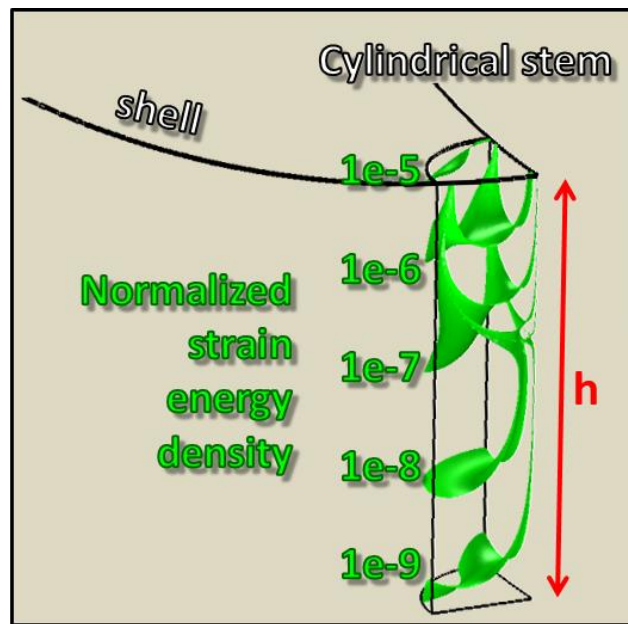


Figure 7.17: Strain energy distribution in a long stem that supporting the hemispherical shell

This means, further energy doupling is needed in order to increase its quality factor. This can be done by either pushing the energy away from the support or trapping the energy in a stem. By increasing the mode number, the energy is pushed away further from the support. However, for better sensitivity and longer ringdown time, the lowest fundamental resonance mode ($m=2$) is selected to release the requirement on quality factor. Thus,

supporting the hemispherical shell with a long stem can improve the support loss by trapping the energy.

In order to verify this argument, a cylindrical stem is added to a hemispherical shell. Strain energy density is calculated for $m=2$ mode in the stem structure. Figure 7.17 shows the decay of strain energy density along the length of the stem. With the length of $200\ \mu\text{m}$, the strain energy density reduces to 0.01% of that at the bottom of the shell. To prove this by simulation, perfectly matched layers (PML) should be used as introduced in Section 2.2.3. However, it is almost impossible for such low frequency devices due to its long wavelength. Another way of predicting support loss is needed. Considering the definition of quality factor:

$$Q = 2\pi \frac{\text{Energy Stored}}{\text{Energy Dissipated per Cycle}} \quad (7.1)$$

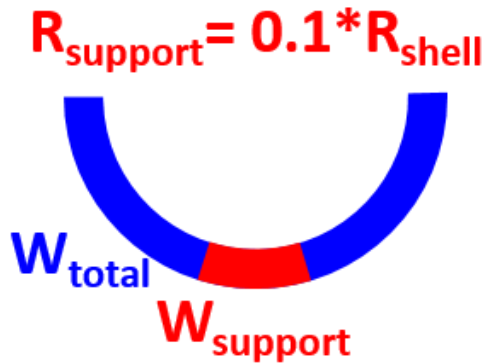


Figure 7.18: Illustration on support loss estimation

Ignoring all other energy dissipation mechanisms, the energy is only converting between strain energy and kinetic energy. At some point, the energy stored can be the total strain energy integrated all over the volume of the hemispherical shell, and the energy dissipated can be the strain energy dissipated through the support. If assuming the strain energy at the support area is totally dissipated, the lower bound of the Q_{support} can be estimated. In case there is any energy reflected by the support structure, the Q_{support} can be higher than the estimated value. Figure 7.18 shows the schematic of the support loss model.

The size of the support is assumed to be 1/10 of the diameter of the shell. Any strain energy in this region will be considered to be lost. Then, the lower bound of Q_{support} can be calculated by equation (7.1). Table 7.1 shows the calculated results for various designs. The result matches well with the current hemisphere design, showing a lower bound of Q of 5,372. By increasing the lateral diameter of the hemispherical shell without increasing the depth, the hemisphere turns into a shallow hemisphere (birdbath). This will increase the Q to about 54,161. By adding a long stem to support the hemispherical shell, Q will be increased to 4,800,000. This provides the evidence to add a long stem at the support for higher quality factors.

Table 7.1: Support loss estimation results for various designs⁶

structure	Hemisphere 	Shallow Hemisphere 	Hemisphere and Cylinder 
R_w ($m=2$)	5,372	54,161	4,800,000

The backside DC contact design has the capability of tailoring the length of the stem, while the front side DC contact design does not. Longer XeF₂ release and HF release is performed on a polysilicon μ HRG with diameter of 900 μm and thickness of 1 μm . The polysilicon that deposited on the side wall of the through hole creates a cylindrical tube that acts as a long stem as figure 7.19 shows. Testing result shows a Q of 40,404 for $m=2$ modes at 11.1 kHz. However, this will decrease the fabrication yield due to the extremely compliance structure, especially during transferring sample between different solutions

⁶ Courtesy of Dr. Vahid Tavassoli on support loss estimation

between supercritical drying. The hemispherical shell has a much larger chance to pop off from its support.

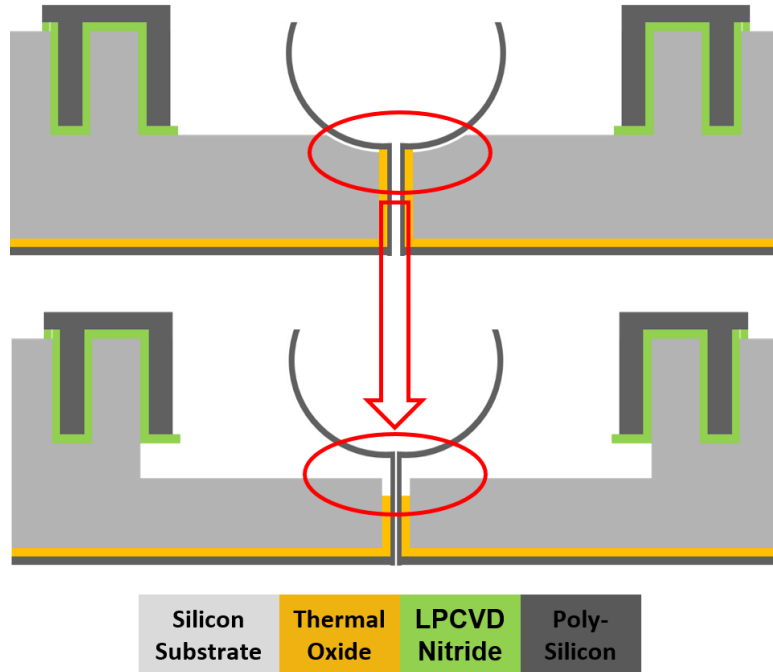


Figure 7.19: Support structure optimization: long stem

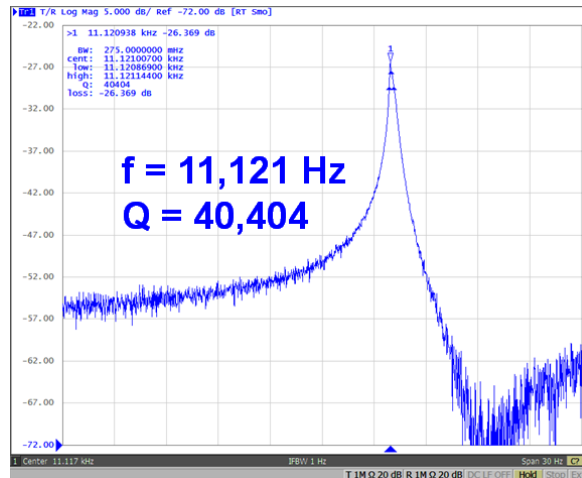


Figure 7.20: m=2 mode for a polysilicon μHRG with long stem

The measurement on the frequency mismatch between two degenerate modes shows a 105 Hz as fabricated mismatch. This is proved to be tunable and matchable in precious section. Also in section 2.3.1, it has been simulated that the frequency mismatch

between $m=2$ degenerate modes should be negligible for 111 substrate. The difference between the simulation and measurement could come from the error during cutting the silicon wafer. There is always a slight deviation from the perfect 111 plane that will cause some finite frequency mismatch.

CHAPTER 8

SUMMARY AND FUTURE WORK

8.1 Contributions

This dissertation introduces the design, fabrication and performance characterization of microscale hemispherical shell resonators and resonating gyroscopes. The research is funded by DARPA MRIG project [86] (Contract #HR0011-00-C-0032) led by Northrop Grumman Corporation. There is a collaborative effort between IMEMS lab at Georgia Tech and Advanced Sensors Navigation Systems Division at Northrop Grumman Corporation. Georgia Tech is in charge of design, fabrication and initial characterization of μ HRG, while Northrop Grumman is responsible for front-end and back-end electronics design. The contributions delivered by this dissertation are listed as follows:

1. Developed a microfabrication process that can build a freestanding, stem-supported hemispherical shell that can be assembled with insulated electrodes for capacitive drive and sense. The frequency mismatch is measured at different processing parameters, which are optimized to give highly symmetric hemispherical shell with low frequency mismatch between two $m=2$ degenerate modes at low resonance frequency. The measured results of the resonator promises a high performance rate mode gyroscope.
2. Theoretical and experimental study of various energy dissipation of microscale hemispherical shell resonators (μ HSR). Thermoelastic damping, squeezed film damping, and support loss are studied by COMSOL multiphysics modeling, providing the baseline on designing of μ HSR and μ HRG in terms of material selection, capacitive gap design, support structure design. Quality factors at various environment for various designs are measured to support the simulation by experimental results.
3. Electro-mechanical design and modeling of μ HRG. Considering a quality factor similar to what is measured for μ HSR, the capacitive gap size is designed accordingly. Electro-

- mechanical model simulates the device performance with the existence of capacitive transducer. It verifies the static pull-in voltages are large enough, so the DC voltage can be applied upto 100 V without device failure. The electrostatic tuning range is large enough so that two degenerate modes can be matched to compensate the as-fabricated frequency split. The drive amplitude is small enough to keep the resonance within the linear region of the transducer, and large enough for better sensitivity and less noise. The Coriolis sensitivity is large enough for a high sensitivity gyroscope.
4. Developed a 3D HARPSS process for polysilicon μ HRG with self-align hemispherical shell and electrodes. This integrated monolithic process consists of seven lithography steps, two of which are performed with the existence of complicated surface topography by the hemispherical mold. Capacitive gaps are scalable from 5 μm to 50 μm or above, polysilicon electrodes are scalable from 50 μm or below to 300 μm . The DC bias contact can be at the front side or backside of the wafer. It is also very important to mention that all the individual process modules are standard and the whole process can be transferred to foundry for future commercialization.
 5. Performance characterization of fabricated polysilicon μ HRG. Frequency response is measured by network analyzer to find out the quality factor and frequency mismatch of $m=2$ modes. The success of fabrication demonstrated a high quality factor axial symmetric structure for μ HRG. Mode matching is performed by applying tuning voltages at antinodes of both drive and sense mode, while mode alignment is performed by applying quadrature nulling voltages at 22.5° or equivalent. The sensitivity of mode matched μ HRG is measured by an open loop configuration with a scale factor of 4.4 $\text{mV}/^\circ/\text{s}$, showing a very sensitive device.

8.2 Future Work

8.2.1 Quality Factor Improvement

As introduced in section 5.4, the sensitivity of the gyroscope is proportional to the quality factor of the resonance. In addition, the ringdown time, which is required for a rate integrating gyroscope, is also proportional to the quality factor. Thus, improving the quality factor can help improve the performance of the rate mode gyroscope and also enable rate integrating mode operation.

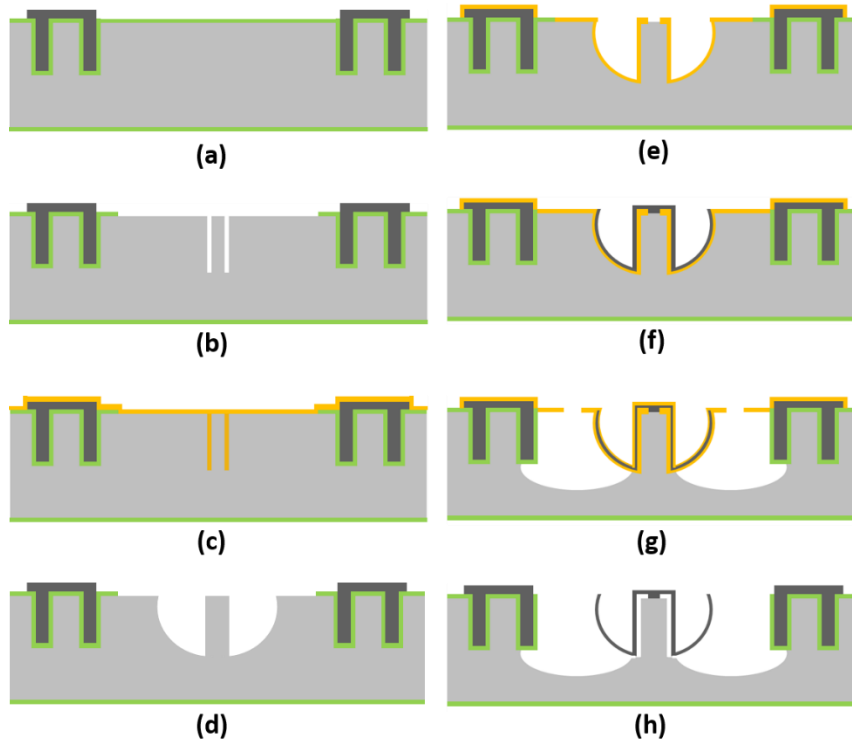


Figure 8.1: Process flow for μ HRG supported by long stem

As discussed in section 7.4, the quality factor of current device is mostly likely limited by support loss, which means further decoupling between the motion and support structure is demanded. By incorporating a long stem at the support structure, the simulation has shown a dramatic increase in quality factor. The fabrication process can be modified by adding another lithography step to define the long stem. Figure 8.1(a) shows the same

procedure as shown in figure 6.1(d). After that, a circular ring is etched to define the long solid stem. The trenches are then refilled by LPCVD TEOS silicon dioxide as figure 8.1(c) shows. After isotropic etching of hemispherical mold in silicon (figure 8.1(d)), there are hemispherical mold and long stem on the structure. Then sacrificial oxide layer is deposited and patterned for DC bias (figure 8.1(e)). Figure 8.1(f) to (h) show the steps of structural polysilicon deposition and release, which is very similar to the figure 6.7. Figure 8.2 shows the fabricated μ HRG supported by the long stem. Figure 8.3 shows the structure of polysilicon electrodes and long stem with the hemispherical shell removed. This process still needs optimization and characterization to make a fully functional device.

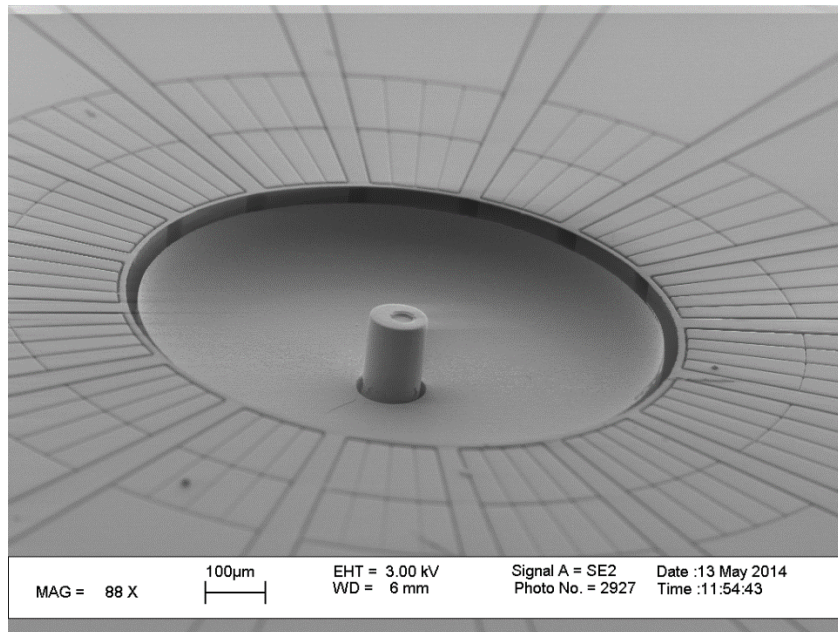


Figure 8.2: Fabricated μ HRG supported by long stem

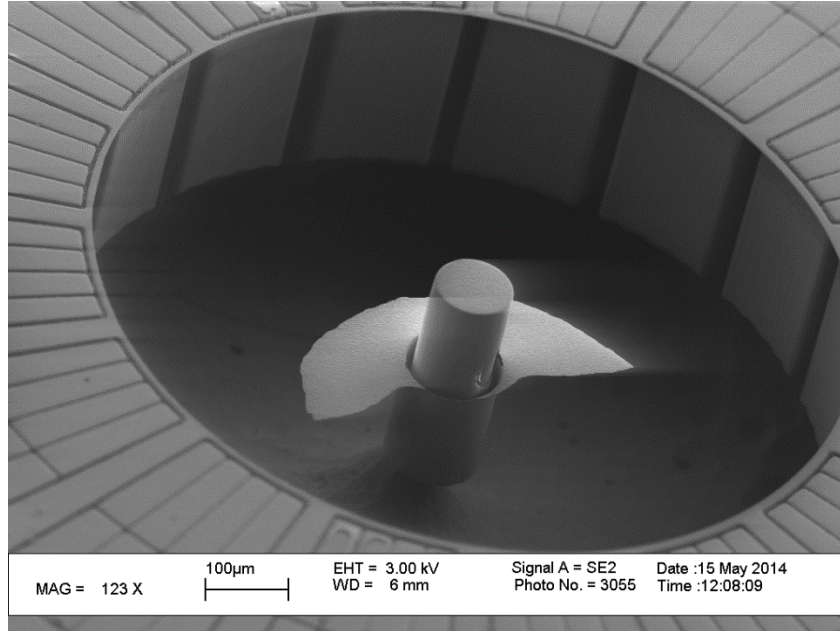


Figure 8.3: Fabricated μ HRG supported by long stem (shell broken)

8.2.2 Rate Integrating Mode Operation

The purpose of this axial symmetric high Q structure is to operate the gyroscope in rate integrating mode. Rate integrating gyroscopes have a number of unique advantages as introduced in section 1.2.2. Of greatest importance to the current research are their high dynamic range, accuracy due to direct measurement of the angle of rotation, and ability to operate interchangeably in the rate integrating and angular rate modes. Despite these noteworthy advantages, rate integrating gyroscope technology has never been demonstrated on the microscale smaller than 10 mm^3 .

The control system of a microscale rate integrating gyroscope (MRIG) should perform four basic functions, including initiating oscillations until the appropriate energy level is reached, maintaining the reached energy level with feedback loop, active tuning of the structure to compensate for frequency mismatch along the principal axes of elasticity, compensating for quadrature-induced perturbations. The MRIG sense function should be able to derive the angle of rotation from sensing displacements and velocities in a pair of

orthogonal directions. At the same time, necessary signals to the feedback control system needs to be provided by the sense function. While the MRIG is operating in rate integrating mode, all the tasks have to be performed seamlessly without interfering with the free precession of the gyroscope.

REFERENCES

- [1] C. Machover, *Basics of Gyroscopes* vol. 1. New York: John F. Rider Publishing, 1963.
- [2] R. H. Dixon and J. Bouchaud, "Markets and applications for MEMS inertial sensors," in *Proceedings of the SPIE - The International Society for Optical Engineering*, 2006, pp. 611306-611306-10.
- [3] P. H. Savet, *Gyroscopes: theory and design*: McGraw-Hill, 1961.
- [4] D. H. Titterton and J. L. Weston, *Strapdown inertial navigation technology*, 2nd ed. vol. 207: American Institute of Aeronautics and Astronautics, Inc, 2004.
- [5] P. Hariharan, "Sagnac or Michelson-Sagnac interferometer?," *Applied Optics*, vol. 14, pp. 2319_1-2321, 1975/10/01 1975.
- [6] "An Update on KVH Fiber Optic Gyros and Their Benefits Relative to Other Gyro Technologies," KVH Industries Inc. 2014.
- [7] B. R. Paul, "Fiber Optic Gyroscope Sensors," in *Fiber Optic Sensors, Second Edition*, ed: CRC Press, 2008, pp. 333-366.
- [8] A. Lawrence, *Modern inertial technology : navigation, guidance, and control*, 2nd ed.: New York : Springer, 1998.
- [9] J. W. S. Pringle, "The Gyroscopic Mechanism of the Halteres of Diptera," *Philosophical Transactions of the Royal Society of London. Series B, Biological Sciences*, vol. 233, pp. 347-384, 1948.
- [10] "QRS116 Single-Axis Tactical Grade Analog Gyroscope," Systron Donner Data Sheet 2012.
- [11] G. Bryan, "On the beats in the vibrations of a revolving cylinder or bell," in *Proceedings of the Cambridge Philosophical Society*, 1890, pp. 101-111.
- [12] D. M. Rozelle, "The Hemispherical Resonator Gyro: From Wineglass to the Planets," in *19th AAS/AIAA Space Flight Mechanics Meeting*, 2009, pp. 1157-1178.

- [13] D. Meyer and D. Rozelle, "Milli-HRG inertial navigation system," *Gyroscopy and Navigation*, vol. 3, pp. 227-234, 2012/10/01 2012.
- [14] G. G. Coriolis, *Mémoire sur les équations du mouvement relatif des systèmes de corps*: Bachelier, 1835.
- [15] M. F. Zaman, "Degree-per-hour mode-matched micromachined silicon vibratory gyroscopes," Ph.D, Georgia Institute of Technology, 2008.
- [16] A. M. Shkel, C. Acar, and C. Painter, "Two types of micromachined vibratory gyroscopes," in *Sensors, 2005 IEEE*, 2005, p. 6 pp.
- [17] C. C. Painter and A. M. Shkel, "Identification of anisoelasticity for electrostatic trimming of rate-integrating gyroscopes," in *SPIE Annual International Symposium on Smart Structures and Materials*, 2002, pp. 157-168.
- [18] M. F. Zaman, A. Sharma, H. Zhili, and F. Ayazi, "A Mode-Matched Silicon-Yaw Tuning-Fork Gyroscope With Subdegree-Per-Hour Allan Deviation Bias Instability," *Microelectromechanical Systems, Journal of*, vol. 17, pp. 1526-1536, 2008.
- [19] J. Bernstein, S. Cho, A. T. King, A. Kourepenis, P. Maciel, and M. Weinberg, "A micromachined comb-drive tuning fork rate gyroscope," in *Micro Electro Mechanical Systems, 1993, MEMS '93, Proceedings An Investigation of Micro Structures, Sensors, Actuators, Machines and Systems. IEEE.*, 1993, pp. 143-148.
- [20] A. Sharma, M. F. Zaman, and F. Ayazi, "A Sub-0.2deg/hr Bias Drift Micromechanical Silicon Gyroscope With Automatic CMOS Mode-Matching," *Solid-State Circuits, IEEE Journal of*, vol. 44, pp. 1593-1608, 2009.
- [21] P. Greiff, B. Boxenhorn, T. King, and L. Niles, "Silicon monolithic micromechanical gyroscope," in *Solid-State Sensors and Actuators, 1991. Digest of Technical Papers, TRANSDUCERS'91., 1991 International Conference on*, 1991, pp. 966-968.

- [22] Y. B. Gianchandani and K. Najafi, "A bulk silicon dissolved wafer process for microelectromechanical devices," *Microelectromechanical Systems, Journal of*, vol. 1, pp. 77-85, 1992.
- [23] C. Acar and A. M. Shkel, "Structurally decoupled micromachined gyroscopes with post-release capacitance enhancement," *Journal of Micromechanics and Microengineering*, vol. 15, p. 1092, 2005.
- [24] S. E. Alper and T. Akin, "A symmetric surface micromachined gyroscope with decoupled oscillation modes," *Sensors and Actuators A: Physical*, vol. 97-98, pp. 347-358, 4/1/ 2002.
- [25] S. E. Alper and T. Akin, "A Single-Crystal Silicon Symmetrical and Decoupled MEMS Gyroscope on an Insulating Substrate," *Microelectromechanical Systems, Journal of*, vol. 14, pp. 707-717, 2005.
- [26] S. E. Alper, Y. Temiz, and T. Akin, "A Compact Angular Rate Sensor System Using a Fully Decoupled Silicon-on-Glass MEMS Gyroscope," *Microelectromechanical Systems, Journal of*, vol. 17, pp. 1418-1429, 2008.
- [27] S. E. Alper, K. Azgin, and T. Akin, "A high-performance silicon-on-insulator MEMS gyroscope operating at atmospheric pressure," *Sensors and Actuators A: Physical*, vol. 135, pp. 34-42, 3/30/ 2007.
- [28] F. Ayazi and K. Najafi, "A HARPSS polysilicon vibrating ring gyroscope," *Microelectromechanical Systems, Journal of*, vol. 10, pp. 169-179, 2001.
- [29] F. Ayazi and K. Najafi, "High aspect-ratio combined poly and single-crystal silicon (HARPSS) MEMS technology," *Microelectromechanical Systems, Journal of*, vol. 9, pp. 288-294, 2000.
- [30] M. W. Putty, "Micromachined vibrating ring gyroscope," Ph.D Thesis, University of Michigan, 1995.

- [31] G. He and K. Najafi, "A single-crystal silicon vibrating ring gyroscope," in *Micro Electro Mechanical Systems, 2002. The Fifteenth IEEE International Conference on*, 2002, pp. 718-721.
- [32] J. Cho, J. A. Gregory, and K. Najafi, "High-Q, 3kHz Single-Crystal-Silicon Cylindrical Rate-Integrating Gyro (CING)," in *Micro Electro Mechanical Systems (MEMS), 2012 IEEE 25th International Conference on*, 2012, pp. 172-175.
- [33] H. Johari and F. Ayazi, "Capacitive Bulk Acoustic Wave Silicon Disk Gyroscopes," in *Electron Devices Meeting, 2006. IEDM '06. International*, 2006, pp. 1-4.
- [34] H. Johari and F. Ayazi, "High-frequency capacitive disk gyroscopes in (100) and (111) silicon," in *Micro Electro Mechanical Systems, 2007. MEMS. IEEE 20th International Conference on*, 2007, pp. 47-50.
- [35] S. Wang-kyung, M. Dalal, and F. Ayazi, "A 3MHz spoke gyroscope with wide bandwidth and large dynamic range," in *Micro Electro Mechanical Systems (MEMS), 2010 IEEE 23rd International Conference on*, 2010, pp. 104-107.
- [36] R. Tabrizian, M. Hodjat-Shamami, and F. Ayazi, "High-Frequency AlN-on-Silicon Resonant Square Gyroscopes," *Microelectromechanical Systems, Journal of*, vol. 22, pp. 1007-1009, 2013.
- [37] H. Johari, "Micromachined capacitive silicon bulk acoustic wave gyroscopes," Ph.D Thesis, Georgia Institute of Technology, 2008.
- [38] A. A. Trusov, I. P. Prikhodko, S. A. Zotov, and A. M. Shkel, "Low-Dissipation Silicon Tuning Fork Gyroscopes for Rate and Whole Angle Measurements," *Sensors Journal, IEEE*, vol. 11, pp. 2763-2770, 2011.
- [39] S.-c. Fan, G.-y. Liu, and Z.-j. Wang, "On flexural vibration of hemispherical shell," *Applied Mathematics and Mechanics*, vol. 12, pp. 1023-1030, 1991.
- [40] W. Flugge, *Stresses in Shells*. Berlin, Germany: Springer-Verlag, 1962.
- [41] L. Meirovitch, *Elements of vibration analysis, 2nd ed.*: New York : McGraw-Hill, 1986.

- [42] A. Duwel, R. N. Candler, T. W. Kenny, and M. Varghese, "Engineering MEMS Resonators With Low Thermoelastic Damping," *Microelectromechanical Systems, Journal of*, vol. 15, pp. 1437-1445, 2006.
- [43] H. W. Lord and Y. Shulman, "A generalized dynamical theory of thermoelasticity," *Journal of the Mechanics and Physics of Solids*, vol. 15, pp. 299-309, 9// 1967.
- [44] R. Abdolvand, H. Johari, G. K. Ho, A. Erbil, and F. Ayazi, "Quality factor in trench-refilled polysilicon beam resonators," *Microelectromechanical Systems, Journal of*, vol. 15, pp. 471-478, 2006.
- [45] R. Lifshitz and M. L. Roukes, "Thermoelastic damping in micro- and nanomechanical systems," *Physical Review B*, vol. 61, pp. 5600-5609, 02/15/ 2000.
- [46] C. Zener, "Internal Friction in Solids. I. Theory of Internal Friction in Reeds," *Physical Review*, vol. 52, pp. 230-235, 1937.
- [47] W. E. Newell, "Miniaturization of Tuning Forks," *Science*, vol. 161, pp. 1320-1326, 1968.
- [48] M. Bao and H. Yang, "Squeeze film air damping in MEMS," *Sensors and Actuators A: Physical*, vol. 136, pp. 3-27, 5/1/ 2007.
- [49] M. Bao, *Analysis and design principles of MEMS devices*: Elsevier, 2005.
- [50] M.-H. Bao, *Micro mechanical transducers: pressure sensors, accelerometers and gyroscopes* vol. 8: Elsevier, 2000.
- [51] M. Esashi, "Wafer level packaging of MEMS," *Journal of Micromechanics and Microengineering*, vol. 18, p. 073001, 2008.
- [52] Z. Hao, A. Erbil, and F. Ayazi, "An analytical model for support loss in micromachined beam resonators with in-plane flexural vibrations," *Sensors and Actuators A: Physical*, vol. 109, pp. 156-164, 12/1/ 2003.
- [53] Z. Hao and F. Ayazi, "Support loss in the radial bulk-mode vibrations of center-supported micromechanical disk resonators," *Sensors and Actuators A: Physical*, vol. 134, pp. 582-593, 3/15/ 2007.

- [54] D. S. Bindel and S. Govindjee, "Elastic PMLs for resonator anchor loss simulation," *International Journal for Numerical Methods in Engineering*, vol. 64, pp. 789-818, 2005.
- [55] J. Yang, T. Ono, and M. Esashi, "Energy dissipation in submicrometer thick single-crystal silicon cantilevers," *Microelectromechanical Systems, Journal of*, vol. 11, pp. 775-783, 2002.
- [56] K. Y. Yasumura, T. D. Stowe, E. M. Chow, T. Pfafman, T. W. Kenny, B. C. Stipe, *et al.*, "Quality factors in micron- and submicron-thick cantilevers," *Microelectromechanical Systems, Journal of*, vol. 9, pp. 117-125, 2000.
- [57] J. Yang, T. Ono, and M. Esashi, "Surface effects and high quality factors in ultrathin single-crystal silicon cantilevers," *Applied Physics Letters*, vol. 77, pp. 3860-3862, 2000.
- [58] D. F. Wang, T. Ono, and M. Esashi, "Thermal treatments and gas adsorption influences on nanomechanics of ultra-thin silicon resonators for ultimate sensing," *Nanotechnology*, vol. 15, p. 1851, 2004.
- [59] C. C. Painter and A. M. Shkel, "Active structural error suppression in MEMS vibratory rate integrating gyroscopes," *Sensors Journal, IEEE*, vol. 3, pp. 595-606, 2003.
- [60] P. Shao, L. D. Sorenson, X. Gao, and F. Ayazi, "Wineglass-on-a-chip," in *Tech. Digest Solid-State Sensors, Actuators, and Microsystems Workshop*, Hilton Head, SC, 2012, pp. 275-278.
- [61] H. Hashimoto, S. Tanaka, K. Sato, I. Ishikawa, S. Kato, and N. Chubachi, "Chemical isotropic etching of single-crystal silicon for acoustic lens of scanning acoustic microscope," *Japanese journal of applied physics*, vol. 32, pp. 2543-2546, 1993.
- [62] L. C. Fegely, D. N. Hutchison, and S. A. Bhawe, "Isotropic etching of 111 SCS for wafer-scale manufacturing of perfectly hemispherical silicon molds," in *Solid-State*

- Sensors, Actuators and Microsystems Conference (TRANSDUCERS), 2011 16th International*, 2011, pp. 2295-2298.
- [63] B. E. Deal and A. S. Grove, "General Relationship for the Thermal Oxidation of Silicon," *Journal of Applied Physics*, vol. 36, pp. 3770-3778, 1965.
- [64] N. Yamamoto, Y. Oshita, A. Ogura, and A. Yoshinouchi, "Orientation Dependence of Silicon Oxidation Ratio in High-Pressure Water Vapor," *Japanese Journal of Applied Physics*, vol. 46, p. 7619, 2007.
- [65] Z. Ji-Tao, L. Yan, L. Zhi-Yong, and W. Xue-Jian, "Determination of mean thickness of an oxide layer on a silicon sphere by spectroscopic ellipsometry," *Chinese Physics Letters*, vol. 27, p. 050601, 2010.
- [66] L. D. Sorenson, X. Gao, and F. Ayazi, "3-D micromachined hemispherical shell resonators with integrated capacitive transducers," in *Micro Electro Mechanical Systems (MEMS), 2012 IEEE 25th International Conference on*, 2012, pp. 168-171.
- [67] P. Shao, V. Tavassoli, C.-S. Liu, L. Sorenson, and F. Ayazi, "Electrical characterization of ALD-coated silicon dioxide micro-hemispherical shell resonators," in *Micro Electro Mechanical Systems (MEMS), 2014 IEEE 27th International Conference on*, 2014, pp. 612-615.
- [68] K. D. Wise, T. N. Jackson, N. A. Masnari, M. G. Robinson, D. E. Solomon, G. H. Wuttke, *et al.*, "Fabrication of hemispherical structures using semiconductor technology for use in thermonuclear fusion research," *Journal of Vacuum Science and Technology*, vol. 16, pp. 936-939, 1979.
- [69] K. Wise, M. Robinson, and W. Hillegas, "Solid-state processes to produce hemispherical components for inertial fusion targets," Michigan Univ., Ann Arbor (USA). Electron Physics Lab.1980.
- [70] B. Sarac, G. Kumar, T. Hodges, S. Ding, A. Desai, and J. Schroers, "Three-Dimensional Shell Fabrication Using Blow Molding of Bulk Metallic Glass," *Microelectromechanical Systems, Journal of*, vol. 20, pp. 28-36, 2011.

- [71] D. Senkal, I. P. Prikhodko, A. A. Trusov, and A. M. Shkel, "Micromachined 3-D Glass-Blown Wineglass Structures for Vibratory MEMS Applications," presented at the Technologies or Future Micro-Nano Manufacturing, Napa, California, USA, 2011.
- [72] D. Senkal, C. R. Raum, A. A. Trusov, and A. M. Shkel, "Titania Silicate / Fused Quartz Glassblowing For 3-D Fabrication of Low Internal Loss Wineglass Microstructures," in *Tech. Digest Solid-State Sensors, Actuators, and Microsystems Workshop*, Hilton Head, SC, 2012, pp. 267-270.
- [73] M. L. Chan, J. Xie, P. Fonda, H. Najjar, K. Yamazaki, L. Lin, *et al.*, "Micromachined Polycrystalline Diamond Hemispherical Shell Resonators," in *Tech. Digest Solid-State Sensors, Actuators, and Microsystems Workshop*, Hilton Head, SC, 2012, pp. 355-358.
- [74] V. Svetovoy, J. Berenschot, and M. Elwenspoek, "Experimental investigation of anisotropy in isotropic silicon etching," *Journal of micromechanics and microengineering*, vol. 17, p. 2344, 2007.
- [75] K. P. Larsen, J. T. Ravnkilde, and O. Hansen, "Investigations of the isotropic etch of an ICP source for silicon microlens mold fabrication," *Journal of Micromechanics and Microengineering*, vol. 15, p. 873, 2005.
- [76] L. Sorenson, P. Shao, and F. Ayazi, "Bulk and Surface Thermoelastic Dissipation in Micro-Hemispherical Shell Resonators," *Microelectromechanical Systems, Journal of*, vol. PP, pp. 1-1, 2014.
- [77] N. Sato and T. Yonehara, "Hydrogen annealed silicon - on - insulator," *Applied Physics Letters*, vol. 65, pp. 1924-1926, 1994.
- [78] M.-C. M. Lee and M. C. Wu, "Thermal annealing in hydrogen for 3-D profile transformation on silicon-on-insulator and sidewall roughness reduction," *Microelectromechanical Systems, Journal of*, vol. 15, pp. 338-343, 2006.

- [79] J. G. Korvink and O. Paul, *MEMS : a practical guide to design, analysis, and applications*: Norwich, NY : W. Andrew Pub. ; Heidelberg, Germany : Springer, c2006., 2006.
- [80] A. Frangi, M. Cremonesi, A. Jaakkola, and T. Pensala, "Analysis of anchor and interface losses in piezoelectric MEMS resonators," *Sensors and Actuators A: Physical*, 2012.
- [81] B. J. Gallacher, J. Hedley, J. S. Burdess, A. J. Harris, A. Rickard, and D. O. King, "Electrostatic correction of structural imperfections present in a microring gyroscope," *Microelectromechanical Systems, Journal of*, vol. 14, pp. 221-234, 2005.
- [82] M. F. Zaman, A. Sharma, and F. Ayazi, "The Resonating Star Gyroscope: A Novel Multiple-Shell Silicon Gyroscope With Sub-5 deg/hr Allan Deviation Bias Instability," *Sensors Journal, IEEE*, vol. 9, pp. 616-624, 2009.
- [83] G. K. Ho, K. Sundaresan, S. Pourkamali, and F. Ayazi, "Micromechanical IBARs: Tunable High-Q Resonators for Temperature-Compensated Reference Oscillators," *Microelectromechanical Systems, Journal of*, vol. 19, pp. 503-515, 2010.
- [84] S. Pourkamali, G. K. Ho, and F. Ayazi, "Low-Impedance VHF and UHF Capacitive Silicon Bulk Acoustic Wave Resonators—Part I: Concept and Fabrication," *Electron Devices, IEEE Transactions on*, vol. 54, pp. 2017-2023, 2007.
- [85] M. F. Zaman, "Degree-Per-Hour Mode-Matched Micromachined Silioecn Vibratory Gyroscopes," Ph.D Thesis, Georgia Institute of Technology, 2008.
- [86] *DARPA MRIG Program.* Available: [http://www.darpa.mil/Our_Work/MTO/Programs/Micro-Technology_Positioning,_Navigation_and_Timing_\(Micro-PNT\)/Inertial_Sensors.aspx](http://www.darpa.mil/Our_Work/MTO/Programs/Micro-Technology_Positioning,_Navigation_and_Timing_(Micro-PNT)/Inertial_Sensors.aspx) (Last Accessed: July 2014)